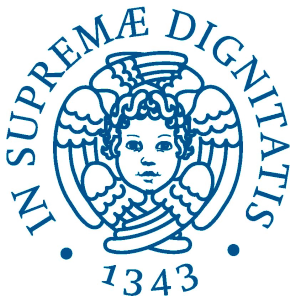

Università di Pisa
Dipartimento di Fisica

Tesi di Laurea Magistrale in Fisica

Quasi-periodic and random THz photonic resonators

Candidato:
Simone Biasco

Relatore:
Dr.ssa Miriam Serena Vitiello

Anno Accademico 2014/2015

CONTENTS

LIST OF FIGURES

LIST OF TABLES

INTRODUCTION

The word "laser" arises from the definition "Light Amplification by Stimulated Emission of Radiation". Conventionally, a laser uses a gain medium to produce stimulated emission of photons and an optical cavity to enhance the intensity of light. This results in good spatial and temporal coherence of radiation and a narrow peak of the spectral energy density around a main frequency.
In the last decades the increasing interest in the field of photonics and nanotechnology has led to some impressive scientific and technological achievements due to the miniaturization of devices and the exploration of yet unexploited regions of the electromagnetic spectrum.
On the one hand, this was possible after the novel theoretical concept of light amplification in multiple quantum wells and superlattices was proposed in 1971, introducing the "Quantum Cascade" mechanism. On the other hand, the development of new nanofabrication technologies and crystal growth techniques, such as the molecular beam epitaxy (MBE), allowed an unprecedented control over the structure of the materials, down to the deposition of nanometer-thick semiconductor layers. This paved the way to the practical realization of active regions for Quantum Cascade Lasers (QCLs) and the successful demonstrations of their use to produce radiation covering the mid-infrared (mid-IR) and the Terahertz (THz) frequency range.

In traditional semiconductor lasers, light emission is based on the recombination of electrons and holes (interband transition) and depends on the energy gap between the initial and final levels. These are usually the conduction and valence bands or the impurity levels of dopants, so their spectral range are determined by the physical and chemical properties of the used materials.
The QCL is an innovative technology which provides an approach to overcome these constraints. The heart of a QCL is its gain medium, a $10\mu m$-thick heterostructure made up by alternating semiconductor layers grown by MBE. The choice of the materials and of the layers' thickness is optimised with the accurate study of the resulting energy levels and electron wavefunctions. This fine regulation of the electronic band structure and states is called "quantum engineering".
In such quantum systems, the transport and optical properties can be tuned by carefully engineering the sequence of well and barrier materials, which induce an electron confinement along the growth direction of the heterostructure. The band splits into discrete energy levels called "subbands", arising in the conduction band, whose energy depends only on the layer thickness, which is controlled via the growth process. Intersubband transitions can then be engineered to produce photons at very low frequencies, in the range $\nu = 300GHz \div 10THz$.
When an electric field is applied, the energy levels are tilted so that electrons are injected in an excited subband and take part to a radiative transition to a lower subband. Then, they tunnel to the next well and emit another photon, and so on (see figure 1). Such "quantum cascade" architecture determines a very favourable rate of photon emission per electron, without recombinating with the holes, so these devices are said "unipolar".
Despite these unique features, QCLs also present many problematic issues to solve. For example, it is difficult to guide light out of the device, since they amplify only TM-polarized radiation, with the electric field $\mathbf{E}$ parallel to the growth direction [1]. At

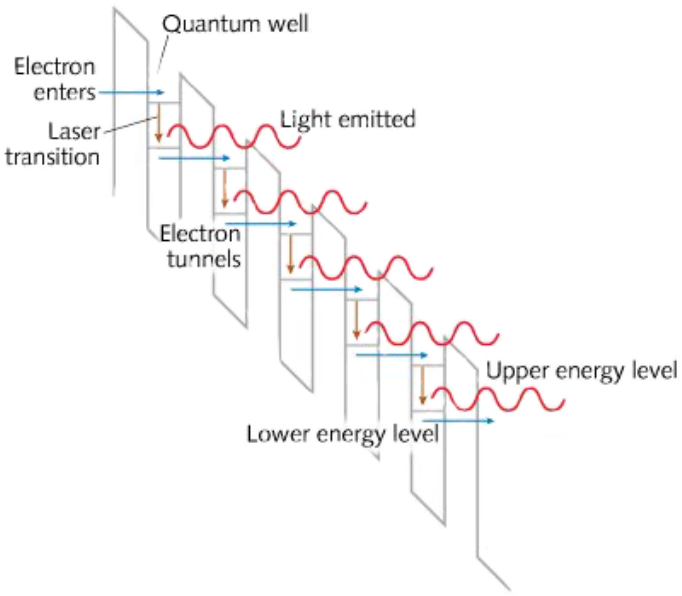

Figure 1: A simplified example of Quantum Cascade

THz frequencies, stimulated emission of photons is complicated by the small energy level separation. Furthermore, the waveguide losses significantly increase, making it necessary to re-design the cavity geometry. In general, at long wavelength ($\lambda > 60\mu m$) they are also affected by huge diffraction and poor beam shape, since the wavelenght of THz radiation is $\lambda = 60\mu m \div 300\mu m$ in vacuum, larger than the typical size of THz QCLs.

The latter issue has been recently addressed by the development of surface-emitting source. These devices are patterned with periodic or aperiodic one- or two-dimensional photonic structures, which exploit light interference to produce vertical emission and enhance the device performance [2]. This is made possible by the feedback effect of the regular or disordered arrangement of scatterers, i.e. regions with a refractive index which differ from that of the surrounding material. Some examples are photonic crystals, quasicrystals and random patterns.
In the case of fully periodic photonic crystals (PC), the propagation of light can be treated with the Bloch theorem thanks to the translational symmetry, producing photonic bands. The dispersion relation $\omega(\mathbf{k})$ presents bandgaps for which no photon can propagate across the structure, strictly selecting the allowed electromagnetic modes.
A different behaviour is produced by photonic quasicrystals (PQC) and other aperiodic, yet deterministic structures: though translational symmetry is lost, long-range order is still present along with orientational order. A larger variety of permitted modes populates the structures since the bandgaps are no longer present, which can be interesting for multi-mode emission.
In a random photonic structure, the highly disordered distribution of scatterers makes photons bounce and interfere with each other, creating modes which can be more or less localised and amplified. Unlike photonic crystals and quasicrystals, random photonic structures are not defined by a deterministic rule. Random lasing is based on a peculiar feedback mechanism, which can be tuned to produce two different regimes, featuring broad or peaked spectral lines, respectively.
The aim of this thesis is to test the use of a 7-fold 2D photonic quasi-crystal to demonstrate multi-mode THz QCL with vertical emission and large efficiency. We also study the possibility of proving random lasing in the THz regime, which has not been demonstrated

yet. This study has involved the theoretical, numerical and experimental works which are presented in the chapters detailed as follows:

- Chapter 1 introduces the fundamental Solid State theory of the envelope function is introduced, the intersubband optical transition and the gain in THz QCLs, population inversion and relaxation dynamics in QCLs, with a particular emphasis on THz QCL active region and waveguide architectures.Finally the main figures of metis are introduced and discussed. The main features of the gain medium are explained, with special attention to the design of the active region and of the waveguides.

- Chapter 2 describes the principles at the basis of the generation and operation of photonic crystal structures and then introduces quasi-crystals and random resonators; the operating principle of such quasi-periodic and random patterns is introduced, with a focus on one-dimensional and two-dimensional photonic structures.

- Chapter 3 describes the implemented algorithm for the generation of quasi-crystal geometries based on the "Generalised Dual Method", computation methods, fabrication protocols, transport and optical testing procedures and beam profile mapping techniques.

- Chapter 4 details the results of the performed two-dimensional simulations for the different types of quasi-crystal and random geometries, obtained with a finite element solver.

- Chapter 5 illustrates the experimental results of the transport and optical characterization of the fabricated devices. Emission spectra, beam intensity profile and thermal behaviour are discussed to understand how the physical and geometrical parameters of the disordered photonic structures affect laser action.

- Chapter 6 introduces the theory of saturable absorption in graphene and the transmission measurement performed to characterize this effect in the THz spectral range, which could be interesting in the perspective of creating a novel mode-locked photonic resonator at THz frequencies.

- Chapter 7 highlights the main conclusions and perspectives associated to the phenomena investigated in this thesis.

1 TERAHERTZ QUANTUM CASCADE LASER: THEORY & OPERATION

Though Quantum Cascade Lasers were first experimentally demonstrated only 20 years ago, today they are a well-established technology, playing an important role in different fields of physics and applications. They are based on many fundamental concepts of quantum mechanics and solid state physics, which will be introduced in the following sections.

1.1 ENVELOPE FUNCTION APPROXIMATION

1.1.1 Derivation in the Single Band Approximation (SBA)

Let us study a crystal in presence of an external potential $U(\mathbf{r})$ which modifies the Schroedinger equation for the wavefunction $\psi(\mathbf{r})$ into:

$$\left(\hat{H}_e + \hat{U}(\mathbf{r})\right)\psi(\mathbf{r}) = E\psi(\mathbf{r}) \tag{1}$$

where $\hat{H}_e = \left(\frac{\hat{\mathbf{p}}^2}{2m_0} + \hat{V}(\mathbf{r})\right)$ is the one-electron hamiltonian with a periodic crystal potential $V(\mathbf{r})$. E is the energy eigenvalue and $\psi(\mathbf{r}) = \sum_{n\mathbf{k}} f_n(\mathbf{k})\psi_{n\mathbf{k}}(\mathbf{r})$ can be expanded over all the bands n and all wavevectors $\mathbf{k}$ in the Brillouin zone of the reciprocal lattice, using the complete othonormal set of Bloch states $\psi_{n\mathbf{k}} = e^{i\mathbf{k}\cdot\mathbf{r}}u_{n\mathbf{k}}(\mathbf{r})$. We assume we deal with a semiconductor (for example GaAs) at temperature $T = 0\ K$ so that the valence band is fully occupied while the conduction one is empty. If we work in the frame of the single band approximation [3], we study a completely isolated band n such that:

- the band is non-degenerate
- it does not cross other bands
- the perturbation $U(\mathbf{r})$ does not induce interband transitions $n \to n'$

Then the Schroendiger equation can be solved in the reciprocal space:

$$\sum_{n\mathbf{k}} f_n(\mathbf{k})E_n(\mathbf{k})\psi_{n\mathbf{k}} + \sum_{n\mathbf{k}} f_n(\mathbf{k})\hat{U}(\mathbf{r})\psi_{n\mathbf{k}} = E\sum_{n\mathbf{k}} f_n(\mathbf{k})\psi_{n\mathbf{k}} \tag{2}$$

As reported in detail in reference [3], a standard projection onto a wavefunction $\psi_{n'\mathbf{k}'}$ makes a sum of the Fourier transforms of the pertubation $\tilde{U}_{\mathbf{k}-\mathbf{k}'-\mathbf{G}}$ appear. The central hypotesis is that the scale of variation of $U(\mathbf{r})$ is much larger than the lattice parameter a, so the only relevant contribution comes from the Fourier components with small wavevector ($\mathbf{G} = 0$). In order to anti-transform to real space, it is convenient to introduce the "envelope function"

$$F_n(\mathbf{r}) = \sum_{\mathbf{k}\in BZ} e^{i\mathbf{k}\cdot\mathbf{r}} f_n(\mathbf{k}) \tag{3}$$

and the non-local operator $\hat{E}_n(-i\nabla) \equiv \sum_{\mathbf{R}} E_{\mathbf{R}} e^{i\mathbf{k}\cdot\nabla}$ which acts on Bloch states this way:

$$\hat{E}(-i\nabla)\left|\psi_{n\mathbf{k}}\right\rangle = \sum_{\mathbf{R}} E_{\mathbf{R}} e^{i\mathbf{k}\cdot\nabla}\left|\psi_{n\mathbf{k}}\right\rangle = E_n(\mathbf{k})\left|\psi_{n\mathbf{k}}\right\rangle \tag{4}$$

These definitions allow obtaining the SBA equation for the envelope function in real space

$$\left[\hat{E}_n(-i\nabla) + \hat{U}(\mathbf{r})\right] F_n(\mathbf{r}) = EF_n(\mathbf{r}) \tag{5}$$

The crystal state associated to the n-th band is

$$\psi_n(\mathbf{r}) = \sum_{\mathbf{k}\in BZ} f_n(\mathbf{k})\psi_{n\mathbf{k}}(\mathbf{r}) = \sum_{\mathbf{k}\in BZ} f_n(\mathbf{k})e^{i\mathbf{k}\cdot\mathbf{r}}u_{n\mathbf{k}}(\mathbf{r}) \tag{6}$$

If we are in a minimum of the band (for example, the Γ point) and $U(\mathbf{r})$ is sufficiently small to keep the state confined, it means U mixes only few states in the reciprocal space and provokes only a slight energy varition. We can restrict to the use of $u_{n0}(\mathbf{r})$ only:

$$\psi_n(\mathbf{r}) \approx \left[\sum_{\mathbf{k}\in BZ} f_n(\mathbf{k})e^{i\mathbf{k}\cdot\mathbf{r}}\right] u_{n0}(\mathbf{r}) = F_n(\mathbf{r})u_{n0}(\mathbf{r}) \tag{7}$$

which is the "envelope function approximation". This choice is convenient for bands with a stationary point at $\mathbf{k} = 0$, while in other cases it is better to use the appropriate $\mathbf{k}_0$ where the energy dispersion has a maximum or a minimum.

1.1.2 Envelope Function in the multiband model

If the assumptions of the single band approximation (SBA) are removed, it is still possible to develop a theory for the envelope function.
In the case the bands cross or are degenerate in some points, we may introduce the ansatz

$$\psi(\mathbf{r}) = \sum_{n\mathbf{k}} f_n(\mathbf{k})e^{i\mathbf{k}\cdot\mathbf{r}}u_{n0}(\mathbf{r}) \equiv \sum_{n\mathbf{k}} f_n(\mathbf{k})\phi_{n\mathbf{k}}(\mathbf{r}) \tag{8}$$

Using the $\mathbf{k}\cdot\mathbf{p}$ hamiltonian (see reference [4], for example) and adding the external perturbation $U(\mathbf{r})$ we find

$$\left[\hat{H}_e + \hat{U}(\mathbf{r})\right]|\phi_{n\mathbf{k}}\rangle = e^{i\mathbf{k}\cdot\mathbf{r}}\left(\frac{\hat{\mathbf{p}}^2}{2m_0} + \hat{V}(\mathbf{r}) + \frac{\hbar}{m_0}\mathbf{k}\cdot\hat{\mathbf{p}} + \frac{\hbar^2k^2}{2m_0} + \hat{U}(\mathbf{r})\right)|u_{n0}(\mathbf{r})\rangle \tag{9}$$

A complete analysis can be found in [3], but for the current discussion we will only sketch the derivation here. In order to find the matrix elements we can treat the bare H_e term and the potential U separately:

- we project $\hat{H}_e|\phi_{n\mathbf{k}}(\mathbf{r})\rangle$ onto $|\phi_{n'\mathbf{k}'}(\mathbf{r})\rangle$ and integrate all over the infinite crystal. With some calculations, it can be seen that the the one-electron hamiltonian $\hat{H}_e$connects only states with the same $\mathbf{k}$:

$$H_{nn'}(\mathbf{k}) = \langle\phi_{n'\mathbf{k}'}(\mathbf{r})|\hat{H}_e|\phi_{n\mathbf{k}}(\mathbf{r})\rangle = \delta_{\mathbf{k}\mathbf{k}'}\left[\left(E_n(0) + \frac{\hbar^2k^2}{2m_0}\right)\delta_{nn'} + \frac{\hbar}{m_0}\mathbf{k}\cdot\mathbf{p}_{nn'}\right] \tag{10}$$

  where $\mathbf{p}_{nn'} \equiv \langle u_{n'0}|\hat{\mathbf{p}}|u_{n0}\rangle$.
  Finally in 9 we can write the first term as $\hat{H}_e\sum_{n\mathbf{k}} f_n(\mathbf{k})\phi_{n\mathbf{k}} = \sum_n H_{nn'}(\mathbf{k})f_n(\mathbf{k})$. This sum contains the contributions of all bands.

- the second addend in 9 projected onto $|\phi_{n'\mathbf{k}'}\rangle$ contains the Fourier transform of U appears. Again we assume the external potential is slowly varying, so that only the components with small wavevectors survive.

$$\langle\phi_{n'\mathbf{k}'}|U(\mathbf{r})|\phi_{n\mathbf{k}}\rangle \approx \delta_{nn'}\tilde{U}_{\mathbf{k}-\mathbf{k}'} \tag{11}$$

  So we find the second addend: $\sum_{\mathbf{k}}\tilde{U}_{\mathbf{k}-\mathbf{k}'}f_{n'}(\mathbf{k})$.

Changing from the reciprocal space representation to the real space, the final equation for the multiband envelope function is

$$\sum_n H_{nn'}(-i\nabla)F_n(\mathbf{r}) + U(\mathbf{r})F_{n'}(\mathbf{r}) = EF_{n'}(\mathbf{r}) \tag{12}$$

If we compare this result with the single band model 5, it is clear that the presence of many bands simply turns $E_{n'}(-i\nabla)F_{n'}(\mathbf{r})$ into $\sum_n H_{nn'}(-i\nabla)F_n(\mathbf{r})$.

Further considerations arise if we add the spin-orbit coupling, which leads to the extra term:

$$\hat{H}_{SO} = \frac{\hbar}{4m_0^2c^2}(\vec{\sigma} \times \nabla V(\mathbf{r})) \cdot \hat{\mathbf{p}} \tag{13}$$

in which $\vec{\sigma}$ is the Pauli spin matrix vector and V is the periodic potential energy due to the crystal. In the case of non-degenerate bands this relativistic effect just creates an additive term in the energy, due to the presence of the same differential operator $\hat{\mathbf{p}}$ as in the $\mathbf{k} \cdot \mathbf{p}$ hamiltonian. Instead spin-orbit coupling has a stronger impact in the case of degenerate bands, partially lifting the degeneracy. For example, if we neglect the energy shift Δ_0 induced by $\hat{H}_{SO}$ in gallium arsenide, silicon and germanium, 6 bands have the same energy at $\mathbf{k} = 0$. When we include this, the bands split into a four-fold and a two-fold degeneracies.
In general the splitting Δ_0 ranges from few tens to few hundreds of meV (for example, $340meV$ in GaAs) and is small with respect to the typical energy gap $E_g > 1\ eV$, but can be comparable to the scale of U. This is a probem for the application of the theory developed here, since one fundamental hypotesis we use is that U is small enough not to induce interband transitions. For an extended analysis, the pioneering paper [3] can give a deeper insight, bringing about the famous "6x6 Luttinger Hamiltonian".

1.2 ENVELOPE FUNCTION FOR HETEROSTRUCTURES

1.2.1 A general introduction

In a heterostructure two different materials A and B are sandwiched togheter in a sequence of alternating layers grown by MBE. In a QCL, semiconductors of type III-V, like GaAs, InGaAs, AlInAs, are conveniently employed. In THz QCLs, GaAS and AlGaAs are the reference choice since they have very similar lattice parameters ($a \approx 5.65\ angstrom$) and ensure a very low conduction band offset ($150 \div 160meV$), minimising the deformation of crystal structures at the interface.
It is postulated the wavefunction can be decomposed as (see [1])

$$\psi(\mathbf{r}) = \sum_n F_n^{A,B}(\mathbf{r})u_{n\mathbf{k}_0}^{A,B}(\mathbf{r}) \tag{14}$$

where we consider a relevant point $\mathbf{k}_0$ in the BZ, which we take in the following at the Γ point ($\mathbf{k}_0 = 0$). This means the electron experiences very little disturbance passing from one layer to the next, apart from the change in the effective mass and the potential. Thus we assume

- the envelope function is slowly varying in real space: its Fourier decomposition is mainly made up of reciprocal vectors near $\mathbf{k}_0 = 0$
- the Bloch functions are the same in both materials: $u_{n0}^A(\mathbf{r}) = u_{n0}^B(\mathbf{r}) \equiv u_{n0}(\mathbf{r})$

In the basic case of a quantum well made by a layer of A clad on both sides by a barrier material B, we define $\mathbf{z}$ as the growth direction. In the perpendicular plane (x, y) the structure is ideally infinite, so its translational invariance allows writing the $x - y$ part of the wave function as a free-particle-like plane wave:

$$F_n(\mathbf{r}_{||}, z) = \frac{e^{i\mathbf{k}_{||}\cdot\mathbf{r}_{||}}}{\sqrt{S}}\chi_n(z) \tag{15}$$

where $\mathbf{r}_{||} = (x, y)$ indicates the in-plane position, $k_{||} = (k_x, k_y)$ the in-plane wavevector and $\sqrt{S}$ is the normalization due to the transverse section S.
The whole hamiltonian is

$$\hat{H}_e = \frac{\hat{\mathbf{p}}^2}{2m_0} + \underbrace{V_A(\mathbf{r})Y_A(z) + V_B(\mathbf{r})Y_B(z)}_{V(z)} \tag{16}$$

where $Y_{A,B}(z) = 1$ when $z \in A, B$ respectively and is zero elsewhere. This turns the right potential on in the different layers. The expression can be written as:

$$\hat{H}_e\psi(\mathbf{r}) = \sum_n \left[\frac{1}{2m_0}(\hbar k_{||} - i\hbar\frac{\partial}{\partial z} + \hat{\mathbf{p}}_B)^2 + V(z)\right]\frac{e^{i\mathbf{k}_{||}\cdot\mathbf{r}_{||}}}{\sqrt{S}}\chi_n(z)u_{n0}(\mathbf{r}) = E\psi(\mathbf{r}) \tag{17}$$

where $\hat{\mathbf{p}}_B$ means the operator $\hat{\mathbf{p}}$ acting only on the Bloch part of the function $u_{n0}(\mathbf{r})$ and $\partial/\partial z \equiv \partial_z$ works only on $\chi(z)$.

Using standard techniques and the assumption of slowly-varying envelope functions over a single cell, which are described in [1], we reach the fundamental result:

$$\hat{D}(z, -i\hbar\partial_z)\chi_n(z) = E\chi_n(z) \tag{18}$$

introducing the operator $\hat{D}$ which contains the contribution of the bare energy bands at the Γ point, plus the action of the differential operators on both the envelope and the Bloch functions. In fact, its matrix element D_{nm} is expressed below

$$\begin{aligned} &D_{nm}(z, -i\hbar\partial_z) \equiv \\ &= \left[E^A_{n0}Y_A(z) + E^B_{n0}Y_B(z) + \frac{\hbar^2}{2m_0}(k^2_{||} - \partial^2_z)\delta_{nm} + \frac{\hbar k_{||}}{m_0}\langle u^*_{m0}|\hat{\mathbf{p}}_B|u_{n0}\rangle - \frac{i\hbar}{m_0}\langle u^*_{m0}|\hat{\mathbf{p}}_B|u_{n0}\rangle\,\partial_z\right] \end{aligned} \tag{19}$$

where $E^{A,B}_{n0}$ is the energy of the bandedge at $\mathbf{k} = 0$.
This expansion is based on the contribution of the bands around the fundamental gap at the Γ point (figure 2): the higher conduction band mainly due to a s-like atomic orbital and the three lower valence bands originating from p-like orbitals. The latter ones are subject to the spin-orbit coupling which partially lifts the degeneracy: the split-off band is separated from the heavy and light hole ones by an energy shift $-\Delta_0$. Since the system is rotationally symmetric around the growth direction, it is useful to use the quantization of the angular momentum along $\mathbf{z}$ to simplify 19. Two examples are now shown to understand the role of the envelope funtion in the description of electronic states in heterostructures.

1.2.2 One-band envelope functions

The simplest situation is a one-band model in which the energy dispersion $E(\mathbf{k})$ is quadratic, using the effective mass approximation. We use the potential energy of the

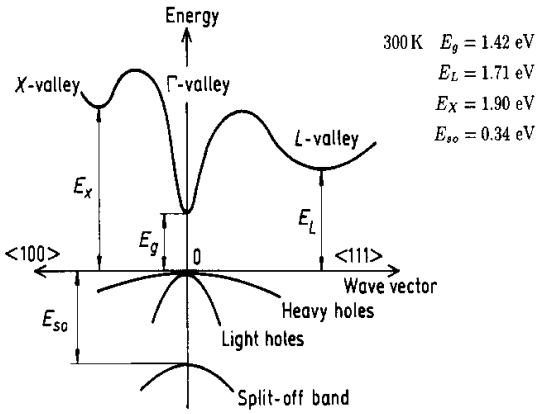

Figure 2: A plot of the GaAs band structure highlighting the heavy hole, light hole and split-off bands around the Γ point [5]

heterostructure $V(z) = V_A(\mathbf{r})Y_A(z) + V_B(\mathbf{r})Y_B(z)$. For simplicity we take the states with $\mathbf{k}_{||} = 0$. Then the envelope function is a solution of the equation

$$\left(-\frac{\hbar^2}{2m^*}\partial_z^2 + V(z)\right)\chi(z) = E\chi(z) \tag{20}$$

The heavy hole band is sufficiently isolated to make this a good approximation, but it must take into account the different effective mass in the well material A and the barrier material B. This means $m^* = m^*(z)$ is a function of the position in the system. The choice of the effective mass is crucial: the most reliable results can be obtained using the value at the center of the BZ $m^*(0)$ corrected for the non-parabolicity effects. The correct boundary conditions at the separation between A and B are

- $\chi(z)$ continuous at the interface
- $\frac{1}{m^*(z)}\partial_z\chi(z)$ continuous at the interface

1.2.3 Two-band envelope functions

In the same hypoteses as in the section above, the more realistic model with both the valence and conduction band is studied.
Let us assume that $k_{||} = 0$, neglect the free particle energy so that $E_{v0} \approx V_v(z)$ and $E_{c0} \approx V_c(z)$ for the valence and conduction band and keep only the first order derivatives in the operator $\hat{D}$ (19) since $|\partial_z u_{n0}| >> |\partial_z\chi|$. The formula 18 gives the system of equations

$$\begin{pmatrix} V_c(z) & -\frac{i\hbar}{m_0}p_{cv}\partial_z \\ -\frac{i\hbar}{m_0}p_{cv}^*\partial_z & V_v(z) \end{pmatrix}\begin{pmatrix} \chi_c \\ \chi_v \end{pmatrix} = E\begin{pmatrix} \chi_c \\ \chi_v \end{pmatrix} \tag{21}$$

Defining the Kane energy is $E_P = 2|p_{cv}|^2/m_0$, this leads to an expression for χ_c

$$\left\{-\frac{\hbar^2}{2}\partial_z \underbrace{\left[\frac{1}{m_0}\frac{E_p}{E - V_v(z)}\right]}_{1/m^*(z,E)}\partial_z + V_c(z)\right\}\chi_c = E\chi_c \tag{22}$$

in which the effective mass $m^*(z, E)$ is introduced to take into account both the non-parabolic features of the bands and the position z along the growth axis, to include the effects of the different alternating materials in this direction.

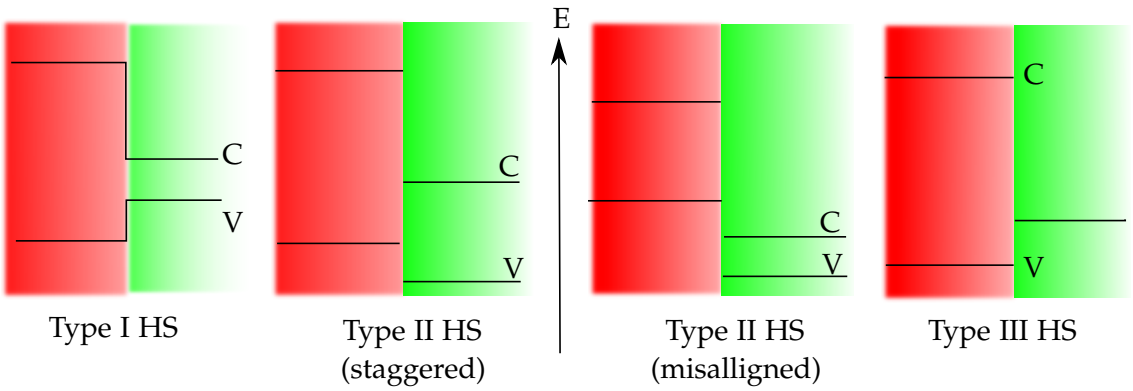

Figure 3: The different types of heterojunctions according to the conduction (C) and valence (V) bands of the two materials in green and red.

This result is self-consistent with the initial approximation of neglecting $\hbar^2 p^2/2m_0$ since its scale is smaller than E_g (typically $1eV$ or more) and even smaller than $E_p \approx 20eV$. The final expression is a Schroedinger-like equation which is widely used:

$$\left[-\frac{\hbar^2}{2}\partial_z \frac{1}{m^*(z,E)}\partial_z + V_c(z)\right]\chi_c = E\chi_c \tag{23}$$

Higher accuracy can be achieved considering more bands, which change the expression for the effective mass, but in these envelope function calculations the importance of the Bloch functions $u_{n0}(\mathbf{r})$ cannot be underestimated. In fact, they serve as a weight for the different envelopes $\chi(z)$ and define the complete physical picture of the electronic wavefunction.

1.2.4 Solving procedure

In order to solve the problem, the following procedure is used:

- For each region in which the potential is assumed constant, the $\chi_n(z)$ and $u_{n0}(\mathbf{r})$ are found within the framework of the effective mass and envelope function approximations.
- Each local solutions is matched at the interface between different materials, in the case of the single-band model the continuity of $\chi_n(z)$ and $\frac{1}{m^*(z)}\partial_z\chi_n$ must be ensured.
- Boundary conditions are imposed on the edge of the samples, with decaying exponentials or periodicity according to the different geometries.

1.3 ENERGY DISPERSION

1.3.1 Transverse electronic confinement

A heterostructure can be classified by the relative energy of the valence and conduction bands in materials A and B (see figure 3). Type I heterostructure have the maximum and the minimum of the energy band in the same layer, so that considering the conduction band shape, one material acts as a quantum well and the next one works as a barrier

material. This creates the electron confinement along the growth direction **z** and splits the single band into many subbands which are the quantazied levels of the well energy. In order to understand the underlying mechanism, it is useful to introduce some simple examples of one-dimensional confinement.

The simplest example of one-dimensional quantum well is built with a potential energy $V(|z| < L/2) = 0$ in the well and $V(|z| > L/2) = \infty$ outside. The solution outside the well is $\psi(z) = 0$, while inside it follows the harmonic behaviour $-\frac{\hbar^2\partial_z^2}{2m_0}\psi = E\psi$ which gives $\psi(z) = A\sin(kz + \delta)$. The continuity of ψ across the interfaces quantizes the allowed wavevectors $k_n = n\pi/L$, so the energy levels are

$$E_n = \frac{\hbar^2 k_n^2}{2m_0} = \frac{\hbar^2}{2m_0}\frac{\pi^2}{L^2}n^2 \quad \text{for} \quad n = \pm 1, \pm 2, \dots \tag{24}$$

This shows that the energy scales with the inverse square of the well size $E_n \sim 1/L^2$. The case of a finite 1D square well is made up by the potential (see [6])

$$V_b(z) = \begin{cases} -V_0 < 0 & |z| < L/2 \\ 0 & |z| \geq L/2 \end{cases} \tag{25}$$

which gives the Schroedinger equation

$$\partial_z^2\psi(z) = \begin{cases} -\frac{2m_0}{\hbar^2}(E + V_0)\psi \equiv \kappa^2\psi & |z| < L/2 \\ -\frac{2m_0}{\hbar^2}E\psi \equiv -q^2\psi & |z| \geq L/2 \end{cases} \tag{26}$$

The quantities

$$q = \frac{\sqrt{2m_0(V_0 - |E|)}}{\hbar} > 0 \qquad \kappa = \frac{\sqrt{2m_0|E|}}{\hbar} > 0 \tag{27}$$

are introduced for energies in $[-V_0, 0]$ since we are looking for bound states. For $|z| < L/2$ the solution is an oscillating function $\psi(z) = A\sin(kz + \delta)$ while outside the well ψ is a decaying exponential to ensure the good behaviour ($\mathcal{L}^2$) of the whole function: $\psi_{(z<-L/2)} = Be^{\kappa z}$ and $\psi_{(z>L/2)} = Ce^{-\kappa z}$. By matching the solutions around $\pm L/2$, and using the relation $\kappa^2 + q^2 = 2m_0V_0/\hbar^2$, a couple of trascendental equations for the energy is found:

$$q(E)\tan\frac{q(E)L}{2} = \pm\kappa(E) \tag{28}$$

where the $+$ sign is taken for even eigenfunctions, the $-$ sign is for odd ones. Equation 28 can be solved numerically or graphically and preserves a dependence on the well size L: increasing its width, the energy eigenvalues diminish.

1.3.2 The 1D coupled wells

In order to introduce the confinement mechanism provided by the iteration of many quantum wells, it is instructive to analyse the case of two identical, one-dimensional quantum wells at a distance $d = z_1 - z_2$. Using 25, a particle is subject to the hamiltonian

$$\hat{H}_e = \frac{\hat{p}_z^2}{2m_0} + \hat{V}_b(z - z_1) + \hat{V}_b(z - z_2) \tag{29}$$

We decompose the ground state wavefunction $\Psi(z) = \alpha\psi_0(z - z_1) + \beta\psi_0(z - z_2)$ on the basis of single-well states ψ_0 centered on z_i, satisfying $\left[\frac{\hat{p}_z^2}{2m_0} + \hat{V}_b(z - z_i)\right]\psi_0(z - z_i) = E_0\psi_0(z - z_i)$ for $i = 1, 2$.

Let us the define the overlap integral r, the energy shift s provoked by one well on the other one's states and the transfer integral t from one well to the other as follows:

$$\begin{aligned} r &\equiv \langle \psi_0(z-z_1)|\psi_0(z-z_2)\rangle \\ s &\equiv \langle \psi_0(z-z_1)|V_b(z-z_2)|\psi_0(z-z_1)\rangle \\ t &\equiv \langle \psi_0(z-z_1)|V_b(z-z_1)|\psi_0(z-z_2)\rangle \end{aligned} \tag{30}$$

This expansion brings about the system of equations

$$\begin{pmatrix} E_0+s-E & (E_0-E)r+t \\ (E_0-E)r+t & E_0+s-E \end{pmatrix} \begin{pmatrix} \alpha \\ \beta \end{pmatrix} = \begin{pmatrix} 0 \\ 0 \end{pmatrix} \tag{31}$$

which can be diagonalised giving two eigenvalues:

$$E_\pm = E_0 + \frac{s \mp t}{1 \mp r} \tag{32}$$

The transfer integral t is responsible for the splitting of the the two-well ground state due to the interaction, since $(E_- - E_+) \sim t$. It is worth noticing that in the limit of distance $d \to \infty$ the coupling disappears and the two wells become independent.

1.3.3 The superlattice concept

In the seminal paper [7], the idea of creating an additional potential by a layered sequence of semiconductor materials was first introduced. This induces an artificial 1D potential with periodicity of the order of 100 *angstrom*, much larger than the classical periodicity of solids (~ 1 *angstrom*). The superlattice potential is

$$V_{sl} = \sum_{n=-\infty}^{\infty} V_b(z-nd) \tag{33}$$

for an infinite number of potential wells with a distance d, with

$$V_b(z-nd) = \begin{cases} -V_0 < 0 & |z-nd| < L/2 \\ 0 & |z-nd| \geq L/2 \end{cases} \tag{34}$$

In the n-th barrier layers, using 27 the electronic states for $E \geq 0$ are described as a combination of plane waves travelling in opposite direction, while for $E < 0$ exponential functions are needed:

$$\begin{aligned} \chi_b^{(n)}(z) &= \alpha e^{i\kappa(z-nd-d/2)} + \beta e^{-i\kappa(z-nd-d/2)} \quad E \geq 0 \\ \chi_b^{(n)}(z) &= \alpha e^{\kappa(z-nd-d/2)} + \beta e^{-\kappa(z-nd-d/2)} \quad E < 0 \end{aligned} \tag{35}$$

In the well material the wavefunctions are (for $E > -V_0$)

$$\chi_w^{(n)}(z) = \gamma e^{iq(z-nd-d/2)} + \delta e^{-iq(z-nd-d/2)} \tag{36}$$

The periodicity of the superlattice potential forces the application of the Bloch theorem, so that a discrete translation $z \to z+nd$ just adds a phase shift to the electronic state: $\chi(z+nd) = e^{iq_{sl}nd}\chi(z)$. Imposing the continuity conditions on χ and $\frac{1}{m^*(z)}\partial_z\chi$ (see [1]) at the interface between the well and the barrier layer and the Bloch theorem, two trascendental equations are found

– for $E \geq 0$:

$$\cos(q_{sl}d) = \cos(qL)\cos[\kappa(d-L)] - \frac{1}{2}\left(\frac{\kappa/m_b^*}{q/m_w^*} - \frac{q/m_w^*}{\kappa/m_b^*}\right)\sin(qL)\sin[\kappa(d-L)] \tag{37}$$

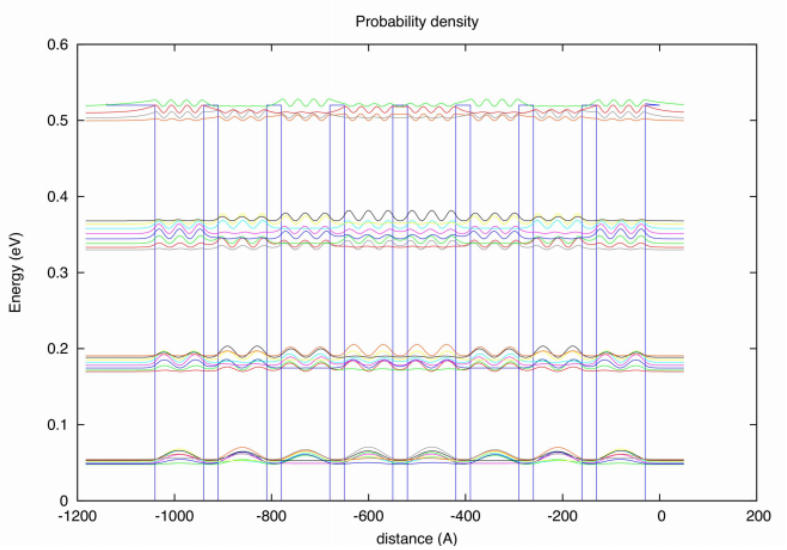

Figure 4: The squared wavefunctions $|\chi(z)|^2$ are plotted in a finite superlattice formed by eight $10nm$-thick InGaAs wells separated by $3nm$-thick AlInAs barriers. [1]

– for $E \in [-V_0, 0]$ (bound states)

$$\cos(q_{sl}d) = \cos(qL)\cosh[\kappa(d-L)] - \frac{i}{2}\left(\frac{\kappa/m_b^*}{q/m_w^*} + \frac{q/m_w^*}{\kappa/m_b^*}\right)\sin(qL)\sinh[\kappa(d-L)] \tag{38}$$

These define a relation between the particle energy E and the momentum associated with the superlattice q_{sl}, depending on some physical parameters like the potential well depth V_0, its size L and the periodicity d. Depending on the actual values of the heterostructure, numerical solutions can be implemented and show the presence of the so-called "minibands" and "minigaps", which are respectively the allowed and forbidden energy zones for the particle in the reciprocal space.

As in classical periodic crystals the bandgap opens at the edge of the Brillouin Zone, in a superlattice heterostructure the artificial potential induces the aperture of the minigap at $q_{sl} = \frac{\pi}{L} = \frac{1}{N}\frac{\pi}{a}$. This allows restricting to the "Brillouin mini-zone" extending over a small region $\left[-\frac{1}{N}\frac{\pi}{2a}, \frac{1}{N}\frac{\pi}{2a}\right]$ of the real BZ. In real-life experiments superlattices have a finite size (see figure 4), but a heterostructure with a sufficient number of quantum wells can mimic their features, provided that some conditions are fulfilled:

- coherence length of the electron wavefuction $\lambda_\phi >> L$ (ideally infinite):
  the electron must be as delocalised as possible to feel the action of the barriers, so that the interplay of reflection and transmission of the states in each layer creates the interference needed to form the miniband.

- homogeneuous broadening condition:
  each miniband has an energy width ΔE which grows at higher energy, since the wavefuctions are more and more overlapping and produce a larger inter-well coupling. Each particle has a lifetime τ, so it is needed that $\Delta E > \hbar/\tau$.

- inhomogeneous broadening condition:
  the energy levels are very sensitive to the wells' size L and small fluctuations ΔL in the growth process of the heterostructure naturally produce a spread in energy Δ_{spread}. In order to have well-defined minibands, we require $\Delta E >> \Delta_{spread}$.

Thus the definition of superlattice depends on the miniband which is considered: in general minibands at very low energy, near the bottom of the wells, host localised electronic states on a very narrow energy level ($\Delta E << E$). Instead higher minibands have larger ΔE and are made up by delocalised wavefunctions across many wells. In the latter case the above hypoteses are respected and the superlattice is properly defined.

1.3.4 In-plane dispersion

Up to now the contribution of the $x-y$ motion of the electron has been neglected, working in the approximation $k_{||} \approx 0$ in the envelope function scheme:

$$\psi(\mathbf{r}) = \sum_n F_n(\mathbf{r}_{||}, z) u_{n0}(\mathbf{r}) = \sum_n \frac{e^{i\mathbf{k}_{||}\cdot\mathbf{r}_{||}}}{\sqrt{S}} \chi_n(z) u_{n0}(\mathbf{r}) \tag{39}$$

This choice was used to derive the fundamental Schroedinger-like equation for the envelope $\chi(z)$ (23). In fact, including $k_{||}$ in the differential operator D_{nm} in 19 on page 4 introduces an additive diagonal term $-\hbar^2\partial_z^2/2m_0 \to \hbar^2(k_{||}^2 - \partial_z^2)/2m_0$ and an off-diagonal contribution $+\frac{\hbar k_{||}}{m_0}\langle u_{m0}^*|\hat{\mathbf{p}}_B|u_{n0}\rangle$.
An intuitive explaination may be useful: the transverse confinement due to the superlattice splits each well into many discrete levels, and the in-plane momentum adds a parabolic dispersion on each of these shifted subbands, in the effective mass approximation:

$$E(i, k_{||}) = E_i(k_{||}) + \frac{\hbar^2 k_{||}^2}{2m^*} \tag{40}$$

Even though there are other effects, this physical picture is roughly correct, at least for $k_{||}$ not too far from zero.
An approximate approach to take the in-plane dispersion into account is the following: the subband confinement energy $E_i(0)$ at $k_{||} = 0$ is associated to a wavevector, as if it was a bulk material

$$k_z^{(i)} = \frac{\sqrt{2m^*(E_i(0))}}{\hbar} \tag{41}$$

Then the energy of the subband for any $k_{||}$ is given by

$$E(i, k_{||}) = \frac{\hbar^2}{2m^*\left(E(i, k_{||})\right)} \left(k_{||}^2 + k_z^{(i)2}\right) \tag{42}$$

where the effective mass follows the relation: $m^*(E(\mathbf{k})) = m^*(0)(1 + E(\mathbf{k})/E_g)$. With a little algebra, one finds the confinement energy of the i-th subband [1]:

$$E(i, k_{||}) = \frac{E_g}{2}\left\{-1 + \left[1 + 4\left(\frac{E_i(0)}{E_g} + \frac{E_i^2(0)}{E_g^2} + \frac{\hbar^2 k_{||}^2}{2m^*(0)E_g}\right)\right]^{1/2}\right\} \tag{43}$$

This approximations holds very precisely for the conduction subbands, since the other bands are well separated in energy and no interband interaction is present. In the case of the valence bands, they are too close in energy and the in-plane momentum $\hbar k_{||}$ couples them, requiring a complete multiband $\mathbf{k}\cdot\mathbf{p}$ hamiltonian study which may also include remote bands. This enhances the non-parabolicity effects and prevents the crossing between the light and heavy bands around the Γ point, since they have different masses and different confinement energies. Nevertheless the $\mathbf{k}\cdot\mathbf{p}$ interaction starts mixing the bands for $\mathbf{k} \neq 0$ so that the different states become superpositions of Bloch functions, resulting in a rather complex band structure.

1.4 INTERSUBBAND OPTICAL TRANSITIONS

1.4.1 Interaction with electromagnetic fields

Optical absorption and gain are based on the interaction of the electromagnetic field with the electronic states, which change their energy and momentum when photons are absorbed or emitted. In the case of interest, the fields are strong enugh to change the population distribution among the states, but do not create "dressed states" where the whole system of light+electron states should be treated quantistically. This means a semi-classical description [6] is sufficient and the perturbation theory can be used with the hamiltonian:

$$\hat{H} = \hat{H}_e + \hat{H}_{int}(t) \tag{44}$$

Using the Coulomb gauge for the potential vector $\nabla \cdot \mathbf{A}(\mathbf{r},t) = 0$, the electric field is $\mathbf{E} = -\frac{1}{c}\partial_t \mathbf{A}$ and the magnetic field is $\mathbf{B} = \nabla \times \mathbf{A}$. The kinetic part of the hamiltonian becomes:

$$\hat{K} = \frac{1}{2m}\left(\hat{\mathbf{p}} - \frac{e\mathbf{A}}{c}\right)^2 = \frac{\hat{\mathbf{p}}^2}{2m} - \frac{e}{mc}\mathbf{A}(\mathbf{r},t)\cdot\hat{\mathbf{p}} + o(\mathbf{A}^2) \tag{45}$$

where the effetive mass m^* is needed when using the single band approximation, while, in the multiband case, the bare electron mass m_0 can be used, since the $\mathbf{k}\cdot\mathbf{p}$ part induces itself an effective mass. Hereinafter, the second order contibution in $\mathbf{A}$ and the magnetic coupling $-\boldsymbol{\mu}\cdot\mathbf{B}$ are neglected since we work in the perturbative regime. This means the light-matter interaction is described by

$$\hat{H}_{int}(\mathbf{r},t) = -\frac{e}{mc}\mathbf{A}(\mathbf{r},t)\cdot\hat{\mathbf{p}} \tag{46}$$

For a plane wave the potential vector is $\mathbf{A}(\mathbf{r},t) = \mathbf{A}_0 e^{i(\mathbf{k}\cdot\mathbf{r}-\omega t)} + \mathbf{A}_0^* e^{-i(\mathbf{k}\cdot\mathbf{r}-\omega t)}$ where the polarization is given by the direction of the vector $\mathbf{A}_0 = A_0\mathbf{e}$. Let us take an initial electronic $|i\rangle$ ad a final state $|f\rangle$, so the matrix element is

$$\langle f|\hat{H}_{int}|i\rangle = -\frac{e}{mc}\langle f|\mathbf{A}(\mathbf{r},t)\cdot\hat{\mathbf{p}}|i\rangle \approx -\frac{e}{mc}\mathbf{A}(\mathbf{r},t)\cdot\langle f|\hat{\mathbf{p}}|i\rangle \tag{47}$$

where it is assumed that the scale of variation of the potential $\mathbf{A}$ is much larger than any dimension of electronic origin, extracting it from the integral. Such approximation is effectively good for THz devices whose emitted wavelength is even larger than the device size. This is the famous "dipole approximation", because the relation $\mathbf{p} = m\dot{\mathbf{r}} = m[H_e, \mathbf{r}]$ gives:

$$\langle f|\hat{\mathbf{p}}|i\rangle = im\frac{E_f - E_i}{\hbar}\langle f|\hat{\mathbf{r}}|i\rangle \equiv im\omega_{if}\langle f|\hat{\mathbf{r}}|i\rangle \tag{48}$$

that contains the dipole matrix element $\langle f|\hat{\mathbf{r}}|i\rangle$. Thus 47 turns into

$$\langle f|\hat{H}_{int}|i\rangle \approx -\frac{ie\omega_{if}}{c}\mathbf{A}(\mathbf{r},t)\cdot\langle f|\hat{\mathbf{r}}|i\rangle \tag{49}$$

As seen in the previuos sections, electronic states in a heterostructure can be described with the envelope function, so let us take the initial and final states as: $\psi_i = F_i(\mathbf{r}_{||},z)u_{n0}(\mathbf{r})$ and $\psi_f = F_f(\mathbf{r}_{||},z)u_{n'0}(\mathbf{r})$. The formula 47 highlights the possibility of two kinds of transitions [8]:

$$\langle\psi_f|\hat{\mathbf{p}}|\psi_i\rangle = \underbrace{\langle u_{n'0}|\hat{\mathbf{p}}|u_{n0}\rangle\langle F_f|F_i\rangle}_{interband\ term} + \underbrace{\langle u_{n'0}|u_{n0}\rangle\langle F_f|\hat{\mathbf{p}}|F_i\rangle}_{intersubband\ term} \tag{50}$$

- interband transition:
  radiation changes the electron band $n \to n'$ (e.g., from valence to conduction band) and the processes depends on both the spatial overlap between the envelope functions and the dipole matrix between the two Bloch functions. When the initial and final Bloch states are the same, the parity selection rules gives $\langle u_{n0}|\hat{\mathbf{p}}|u_{n0}\rangle = 0$.

- intersubband transition:
  it becomes relevant when the interband term vanishes, in fact it is non-zero only when the Bloch state is not modified, since $\langle u_{n'0}|u_{n0}\rangle = \delta_{nn'}$ and relies on the dipole matrix element between two different envelope functions.

1.4.2 Intersubband transitions

Strictly speaking this separation between intersubband and interband processes is no longer valid when the multiband approach is used, that is the electron wavefunction is written as a linear combination of many states $\psi_i = \sum_n F_i^{(n)}(\mathbf{r}_{||}, z)u_{n0}(\mathbf{r})$. This is especially true for the valence band which undergoes a strong mixing of states for $\mathbf{k} \neq 0$.
It is instructive to work in the single-band model for now [8]. Using the envelope function 15 on page 4, the intersubband matrix element is:

$$\begin{aligned}\langle F_f|\mathbf{e}\cdot\hat{\mathbf{p}}|F_i\rangle &= \frac{1}{S}\int d^2\mathbf{r}_{||}dz e^{-i\mathbf{k}'_{||}\cdot\mathbf{r}_{||}}\chi^*_{n'}(z)\left[e_x p_x + e_y p_y + e_z p_z\right] e^{i\mathbf{k}_{||}\cdot\mathbf{r}_{||}}\chi_n(z) \\ &= i\hbar(e_x k_x + e_y k_y)\delta(\mathbf{k}'_{||} - \mathbf{k}_{||})\delta_{nn'} + \delta(\mathbf{k}'_{||} - \mathbf{k}_{||})e_z\langle\chi_{n'}|p_z|\chi_n\rangle\end{aligned} \tag{51}$$

because in the single-band model the χ_n eigenfunctions are orthonormal to each other.
The result 51 shows that the in-plane components of the electric field do not produce any transitions, since they have non-zero matrix elements only when the initial state is conserved. Conversely, when the field is polarized along the growth axis $\mathbf{z}$, an intersubband process can connect χ_n and $\chi_{n'}$, though the in-plane momentum $\mathbf{k}_{||}$ is preserved: this very famous selection rule specifies that the intersubband-based device can emit only TM-polarized radiation, with $\mathbf{E} \parallel \mathbf{z}$ and the magnetic field $\mathbf{B}\perp\mathbf{z}$.
It is useful to define the dimensionless oscillator strength

$$f_{nn'} \equiv \frac{2}{m^*\hbar\omega_{nn'}}|\langle\chi_{n'}|p_z|\chi_n\rangle|^2 = \frac{2m^*\omega_{nn'}}{\hbar}|\langle\chi_{n'}|z|\chi_n\rangle|^2 \tag{52}$$

which measures the strength of the dipole interaction. For GaAs and InGaAs this quantity is often very large in the mid- and far-infrared, up to $f \approx 20 \div 30$. Since the relation of completeness $\sum_n |\chi_n\rangle\langle\chi_n| = \mathbb{1}$ holds in the single-band approximation, counting all the transitions starting from χ_n to all the possible final states $\chi_{n'}$ gives the sum rule

$$\sum_{n'} f_{nn'} = 1 \tag{53}$$

where absorption processes are taken positive ($\omega_{nn'} > 0$) while emission has a negative sign ($\omega_{nn'} < 0$). It is worth noticing that the intersubband oscillator strength is inversely proportional to the effective mass: so narrow-gap semiconductors have a larger intersubband strength than large-gap materials.
A simple model based on an infinite quantum well (see [8]) shows that intersubband transitions between high energy consecutive states $\chi_j \to \chi_{j+1}$ have increasing oscillator strength. In fact, the general formula is $f_{n,m} = \frac{64n^2m^2}{\pi^2(n^2-m^2)^3}$ and for high values of j it becomes $f_{j,j+1} \approx jf_{12}$, which means that transitions between excited states have larger intersubband absorption than the processes starting from the fundamental state.

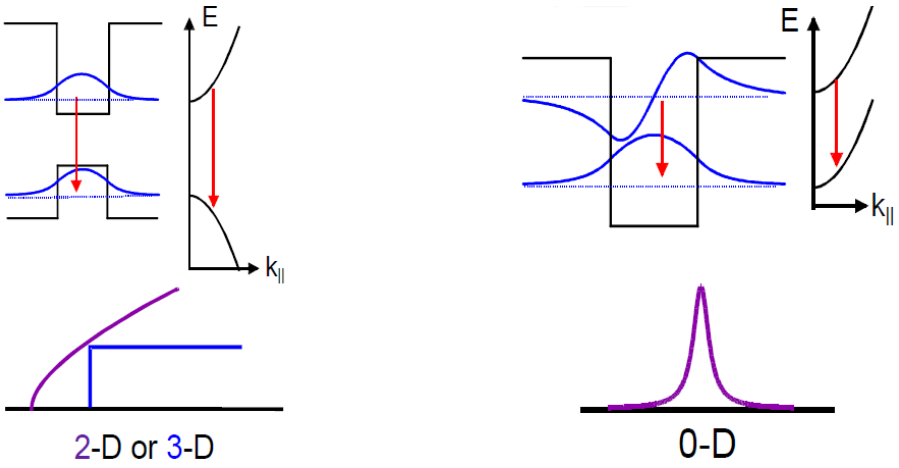

Figure 5: On the left, the interband transition between different Bloch functions has a broad 2D or 3D joint density of states (DOS); on the right the intersubband transition connects two envelope functions of the same band, giving a narrow "0D-like" joint DOS.

Using the Fermi golden rule, the probability of an intersubband dipole transition between two envelope functions of the same band is

$$P_{nn'} = \frac{2\pi}{\hbar}\left(\frac{eA_0}{m^*c}\right)^2 |\langle\chi_{n'}|e_z p_z|\chi_n\rangle|^2 \delta\left(E(n',\mathbf{k}_{||}) - E(n,\mathbf{k}_{||}) - \hbar\omega\right)\Omega(n,n',\mathbf{k}_{||}) \tag{54}$$

taking into account the occupation of the involved subbands with a term that includes the Fermi-Dirac distribution

$$\Omega(n,n',\mathbf{k}_{||}) \equiv f\left(E(n,\mathbf{k}_{||})\right)\left[1 - f\left(E(n',\mathbf{k}_{||})\right)\right] \tag{55}$$

The overall probability for the process $n \leftrightarrow n'$ at a given $\mathbf{k}_{||}$ is

$$W(n,n',\mathbf{k}_{||}) = P_{nn'} - P_{n'n} = \frac{2\pi}{\hbar}\left(\frac{eA_0}{m^*c}\right)^2 |\langle\chi_{n'}|e_z p_z|\chi_n\rangle|^2 \delta\left(E(n',\mathbf{k}_{||}) - E(n,\mathbf{k}_{||}) - \hbar\omega\right)\left[f\left(E(n,\mathbf{k}_{||})\right) - f\left(E(n',\mathbf{k}_{||})\right)\right] \tag{56}$$

Using the approximation 40 at zero temperature, we can treat the $\mathbf{k}_{||}$-dependence of the occupation as a superior order effect and integrate over the 2D in-plane momentum to compute the full transition probability between the subbands:

$$W_{tot}^{n,n'} \propto |\langle\chi_{n'}|e_z p_z|\chi_n\rangle|^2 \left[f(E_n) - f(E_{n'})\right] \int \frac{d^2\mathbf{k}_{||}}{(2\pi)^2}\delta\left(E(n',\mathbf{k}_{||}) - E(n,\mathbf{k}_{||}) - \hbar\omega\right) \tag{57}$$

where the discrete sum is turned into an integral: $\sum_{\mathbf{k}_{||}} \to \int d^2\mathbf{k}_{||}/(2\pi)^2$.

The formula can be written as a surface integral $W_{tot}^{n,n'} \propto \int \frac{dS_{\mathbf{k}_{||}}}{|\nabla_{\mathbf{k}_{||}}\left(E(n',\mathbf{k}_{||}) - E(n,\mathbf{k}_{||})\right)|}$

This is the joint density of state which has a strong singularity when the energy subbands are parallel (the denominator is zero), which is the case of intersubband excitations. This singularity is very sharp and is often referred to as a "δ-like" peak, a bit broadened by non-parabolicity and scattering effects.

Conversely, typical interband transitions are much broader since the joint density of states is step-like in 2D or growing as a square root of the energy in 3D, allowing absorption for photon energies larger than the separation E_g between the bands (figure 5).

Intersubband optical transitions are always at a very well-defined frequency, but this

radiative process suffers from the competition with other elastic and inelastic non-radiative phenomena. Because the two subbands have the same quadratic in-plane dispersion, any scattering process providing the right momentum change can move an electron from the upper to the lower state, so the lifetime in the excited subband is very short (some picoseconds).

1.4.3 Absorption and gain

In a heterostructure each layer is few nanometer-wide along the growth axis, while the in-plane dimension is much bigger. Thus a single semiconductor quantum well can be regarded as an essentially bidimensional system. The absorption coefficient (in cm^{-1}) cannot be described as in 3D situations with

$$\alpha_{3D}(\omega) = \frac{d\ (Power)/d\ (Volume)}{Intensity} = \frac{\hbar\omega W_{tot}(\omega)}{I} \tag{58}$$

assuming monochromatic radiation at frequency ω and intensity $I = \frac{1}{2} n \varepsilon_0 c E_0^2 \cos\theta$ taking a real and constant refractive index n_r of the material for now. θ is the angle between the radiation direction and the growth axis $\mathbf{z}$, so that the useful field component is $e_z = \sin\theta$. Using 57, the total scattering rate $W_{tot}(\omega) = 2\sum_{nn'} W_{tot}^{n,n'}$ counts all the possible channels $n \leftrightarrow n'$ (including the spin degeneracy 2) and gives the radiative lifetime $\tau = 1/W_{tot}(\omega)$. The correct definition of the unitless 2D absorption coefficient is the fraction of radiation which is absorbed by the layer

$$\alpha_{2D} I = \frac{Power\ Loss}{S} \tag{59}$$

One can then write:

$$\begin{aligned} \alpha_{2D}(\omega) = & \frac{Power\ Loss}{Intensity \cdot\ S} = \frac{\hbar\omega}{IS}\frac{4\pi}{\hbar}\sum_{nn'}\left(\frac{eA_0}{m^* c}\right)^2 |\ \langle \chi_{n'}|e_z p_z|\chi_n\rangle\ |^2 \cdot \\ & \cdot \int \frac{d^2\mathbf{k}_{||}}{(2\pi)^2}\delta\left(E(n',\mathbf{k}_{||}) - E(n,\mathbf{k}_{||}) - \hbar\omega\right)\left[f\left(E(n,\mathbf{k}_{||})\right) - f\left(E(n',\mathbf{k}_{||})\right)\right] \end{aligned} \tag{60}$$

This expression can be appropriately computed to find how it depends on the temperature, the electron distribution, the angle of incidence of radiation and its frequency. It is also found the absorption is proportional to the oscillator strength associated to each intersubband transition.
Let us restrict the sum to the transition between the lower subband i and the higher subband f having the highest oscillator strength. If the final state has a non-zero occupation, it has an associate sheet density n_f while the initial state has n_i. Einstein's relation show that the rate of stimulated emission from f is exactly the same as the absorption rate in i computed before, so the overall α_{2D} depends on the difference between the sheet density $n_i - n_f$ of the two subbands:

$$\alpha_{2D}(\omega) = \frac{e^2\omega|z_{if}|^2}{c n_r \varepsilon_0}\frac{\gamma}{(E_f - E_i - \hbar\omega)^2 + \gamma^2}(n_i - n_f)\frac{\sin^2\theta}{\cos\theta} \tag{61}$$

It should be noted that the energy-conserving Dirac delta has been replaced by a lorentzian lineshape which introduces a more realistic broadening γ around the transition energy $E_i - E_f$. The bare intrinsic broadening of the transition is $\gamma/\hbar \approx 100Hz$, but the overall one is bigger. In fact, a variety of mechanisms such as electron-electron scattering, electron-phonon scattering, interface roughness, presence of impurities, etc. make the

transition width larger.
When a plane wave arrives with an incident angle $\theta = 0$, radiation propagates along the growth direction **z** but the electric field is TE-polarized (**E**$\perp$**z**) so it does not couple to intersubband processes. Instead when it is fully TM-polarized (**E** $\parallel$ **z**), expression 61 diverges as it happens when the beam is guided by a waveguide.
In this case it is useful to discuss absorption in the paradigm of the interaction with a material with a thickness L, so that an effective 3D absorption coefficient can be defined as $\alpha = \alpha_{2D} \cos\theta / L$ for $\theta \to \pi/2$. This means the volumic density of electrons $N = n_s / L_P$ should be used, where the period of the heterostructure L_P is the length scale of interest:

$$\alpha(\omega) \equiv \lim_{\theta \to \pi/2} \frac{\alpha_{2D} \cos\theta}{L_P} = \frac{e^2 \omega |z_{if}|^2}{c n_r \varepsilon_0 L_P} \frac{\gamma}{(E_f - E_i - \hbar\omega)^2 + \gamma^2} (n_i - n_f) \tag{62}$$

Depending on the value of $n_i - n_f$, the absorption coefficient changes sign:

- $n_i - n_f > 0$: $\alpha(\omega) > 0$ means the intensity of radiation decays crossing the layer, since absorption from state χ_i is stronger than stimulated emission from χ_f.
- $n_i - n_f < 0$: $\alpha(\omega) < 0$ indicates there is amplification of the passing radiation since stimulated emission prevails. This is the regime of population inversion, a necessary conditio for lasing.
- $n_i - n_f = 0$: $\alpha(\omega) = 0$ because absorption and stimulated emission are in balance.

The gain is simply defined as a negative absorption $g(\omega) \equiv -\alpha(\omega)$. A very useful quantity is the peak-gain cross-section, which is the maximum gain per unit of sheet density, obtained at $\hbar\omega = E_i - E_f$:

$$g_c \equiv \frac{g^{max}(\omega)}{n_f - n_i} = \frac{8 e^2 \omega |z_{if}|^2}{c n_r \varepsilon_0 L_P} \frac{1}{\gamma} \propto \frac{|z_{if}|^2}{L_p \lambda \gamma} \tag{63}$$

This relation highlights that the gain grows with the dipole matrix element of the transition, while a long wavelength λ and a large quantum well size are detrimental. Moreover the broadening γ of the transition lowers the gain peak if it is too large.
Up to now the discussion focused on the absorption mechanism in a single quantum well. In a heterostructure, tens or hundreds of quantum wells form a cascade, so the absorption/gain must be multiplied by N_{QW} and by the number of times N_{pass} that light goes back and forth across the device, according to the designed geometry.
There are two type of intersubband transitions in a semiconductor quantum well, which depend on the kind of states involved:

- bound-to-bound: the dipole $|z_{if}|$ between two discrete subbands gives an absorption spectrum narrowly peaked at the energy $\hbar\omega = E_i - E_f$
- bound-to-continuum: radiation couples a discrete level in the well to a state of the continuum, so that absorption takes place in a broad spectral region around the main transition, starting from the onset of the continuum up to higher energies.

1.4.4 Collective effects and absorption

When the electron density is very high (in typical devices, $n_e \approx 10^{16} \div 10^{18} cm^{-3}$), a shift is produced in the absorption frequency by the screening of the interaction between one carrier and the remaining electron bath.

As shown in [1] and [8], the quantum well (QW) can be treated as a sheet of electronic plasma with a surface density n_s, having a 3D conductivity along the growth axis **z**:

$$\sigma_{zz} = \frac{\sigma_{zz}^{2D}}{L_{eff}} = \frac{n_s e^2 f_{12}}{\varepsilon_0 m^* L_{eff}} \frac{i\omega}{\omega_{12}^2 - \omega^2 - 2i\omega/\tau} \tag{64}$$

introducing an effective QW thickness L_{eff} and a broadening $1/\tau$ of the transition $1 \leftrightarrow 2$ centered at the frequency ω_{12}. An external electric field with **z**-component F_z^{ext} in vacuum is reduced by the effective dielectric function of the quantum well $\varepsilon_{zz}(\omega)$, which is a function of the conductivity:

$$\varepsilon_{zz}(\omega) = 1 + \frac{i\sigma_{zz}(\omega)}{\varepsilon_0 \varepsilon_r^{SC} \omega} \;\rightarrow\; F_z^{QW} = \frac{F_z^{ext}}{\varepsilon_{zz}(\omega)} \tag{65}$$

where ε_r^{SC} is the semiconductor dielectric constant. The associated current density is

$$J_z = \sigma_{zz}(\omega) F_z = \frac{\sigma_{zz}(\omega)}{\varepsilon_{zz}(\omega)} F_z^{ext} \equiv \widetilde{\sigma}(\omega) F_z^{ext} \tag{66}$$

where the effective conductivity $\widetilde{\sigma}$ governs the Joule dissipation power $\sim \widetilde{\sigma}(F_z^{ext})^2$.
The final result shows that the screening creates a blue shift of the absorption, since

$$\widetilde{\sigma}(\omega) = \frac{n_s e^2 f_{12}}{\varepsilon_0 m^* L_{eff}} \frac{i\omega}{\widetilde{\omega}_{12}^2 - \omega^2 - 2i\omega/\tau} \tag{67}$$

contains a new transition frequency $\widetilde{\omega}_{12} = \sqrt{\omega_{12}^2 + \widetilde{\omega}_p^2}$ where an effective plasma frequency appears:

$$\widetilde{\omega}_p^2 = \frac{n_s e^2 f_{12}}{\varepsilon_0 \varepsilon_r^{SC} m^* L_{eff}} \tag{68}$$

This many-body effect creates the "depolarization shift" $\delta\omega_{12} = \widetilde{\omega}_{12} - \omega_{12}$ which becomes relevant for high electron density and at low frequency. Thus THz QCLs suffer from this effect more than infrared QCLs.

1.4.5 Electric tuning of interband transitions

One way to change the transition energy is to add a static electric field F_z along the growth direction, so that a potential energy $-eF_z z$ is superimposed to the heterostructure potential made up by the alternating quantum wells and barriers. This tilts the band structure by Stark effect and shifts the n-th subband in a single-band model by a quantity

$$\Delta E_n(F_z) = \langle \chi_n | - eF_z z | \chi_n \rangle + \sum_{j \neq n} \frac{|\langle \chi_n | - eF_z z | \chi_j \rangle|^2}{E_n - E_j} \tag{69}$$

which is non-negligible because the electron wavefunction is spread over many quantum wells. In the case of symmetric QWs, parity makes the term linear in the field disappear, so the the separation between the two subband 1 and 2 has a quadratic correction:

$$\Delta E_{21}(F_z)\Big|_{sym} = \Delta E_2 - \Delta E_1 = \frac{2e^2 |z_{12}|^2}{E_2 - E_1} F_z^2 \tag{70}$$

taking into account the process $1 \leftrightarrow 2$ only. In asymmetric quantum wells the linear term is instead dominant, achieving a large energy shift of tens of meV in structures with a transition of $10^2 meV$:

$$\Delta E_{21}(F_z)\Big|_{asym} = \Delta E_2 - \Delta E_1 = -e(z_{22} - z_{11}) F_z \tag{71}$$

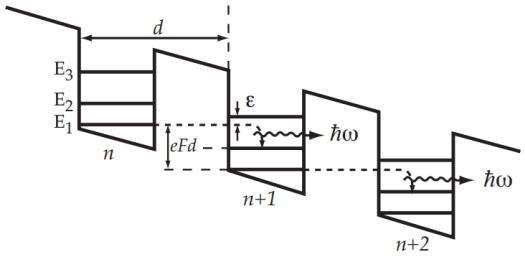

Figure 6: A basic scheme of the cascading mechanism proposed by Kazarinov and Suris, from [1]

1.5 GAIN MEDIA OF QUANTUM CASCADE LASERS

1.5.1 The original idea

As pointed out in [9], the multiple-quantum-well material grown by MBE formed by the alternating layers of GaAs/$Al_xGa_{1-x}As$ is the heart of a typical THz QCL. In the latter system, radiation is produced and amplified according to the specific design of the heterostructure.
In fact, energy levels, wavefunctions and scattering properties can be accurately engineered to ensure the conditions for lasing. As seen in 1.4.3, amplification of the light intensity at a given frequency ω_{12} is achieved when

- population inversion between the final and initial subbands $n_2 > n_1$ is obtained, which means the higher state 2 should have a longer lifetime than the lower state 1
- the gain overcomes the waveguide and active region losses, which happens with sufficiently intense oscillator strength f_{12} and small linewidth γ around the transition energy $\hbar\omega_{12} = E_1 - E_2$
- the device is electrically stable during operation

In the first theoretical proposal [10] by Kazarinov and Suris, a superlattice made up by quantum wells and barrier layers with an applied bias was studied (figure 6). Transitions are possible between subbands of the same QW or between subbands of two adjacent wells. In the latter case, the probability of interaction is governed by the thickness of the tunnel barrier: increasing the barrier layer width, the overlap between the wavefunction diminishes and the oscillator strength lowers, while the intersubband transition in the same QW is favoured. In this scheme, the superlattice is tilted to the point that the ground state of every quantum well is at a higher energy than the first excited level in the next well: on one hand this naturally ensures the population inversion because the decay from the upper level is suppressed, while the depletion of the lower level is very fast. On the other hand, this configuration is electrically unstable since the negative differential resistance (NDR) regime is reached, so it is hard to experimentally prove the phenomenon. Later it was understood that doping could form domains in the superlattice where the energy levels of two adjacent quantum wells are aligned. This resonance enhances the electron tunneling, creating a large current flow which provides a higher electrical stability.

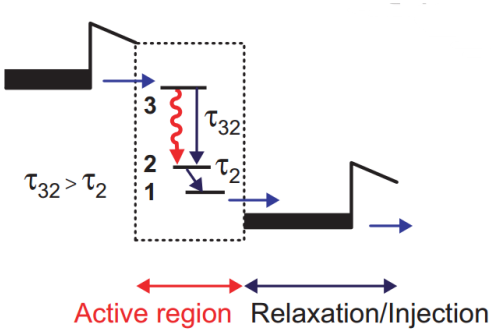

Figure 7: The three-level model for one period of the QCL gain medium [1]

1.5.2 Gain and injection regions in QCLs

Though the superlattice concept proved central to introduce theoretically the idea of intersubband lasing, the experimental development of the first Quantum Cascade Lasers showed a more complex potential stucture, based on the periodic repetition of a unit cell made of finely designed wells and barriers, was needed.
A variety of active region designs has been explored in this two decades, but they share some common features. First of all, the unit period of length L_p consists of a two different zones:

- the gain region:
  it provides and mantains the population inversion between the two subbands involved in the laser transition. In fact electrons are injected in the upper state $n = 3$ and slowly decay downward to the intermediate level $n = 2$, which must be depleted with a typical time τ_2 smaller than the radiative lifetime τ_{32}, if all electrons are injected in level 3 with no leakage to other subbands:

  $$\tau_2 < \tau_{32} \tag{72}$$

  The lower level $n = 1$ is strongly coupled to subband 2, in order to give fast depletion (low τ_2) and carry the electrons to the successive region. See figure 7.

- the injection region:
  it is also called relaxation region and is usually spatially locate before the gain zone. It plays a fundamental role in the transport of electron to the next period, raising the energy of the electron with respect to the bottom of the band, thanks to a series of alternating quantum wells and barriers with changing width, creating a "graded gap" compensating the applied bias. Here doping by silicon donor atoms is inserted, to prevent the formation of local electrical domain and ensure charge-neutrality in the whole period. Appropriate quantum engineering of the levels prevents the escape of the electrons from the upper state of the laser transition $n = 3$, suppressing the non-radiative decay channels 7. Moreover the presence of this stage makes each period longer, reducing the strength of the applied electric field.

Another feature is the cascading mechanism: the presence of an external bias between the top and the bottom layer of the heterostructure produces an electrical field along the growth axis **z**, giving the tilting potential $V(z) = -eE_z z$. Consequently when an electron undergoes a transition emitting a photon, it is recycled and transferred to the next period, where it takes part to another lasing transition and so on, achieving a high rate of emitted

photons per electron.
The increasing of the size of the region in which gain takes place reduces the population density required for each single active region period: the threshold current for which lasing starts is lowered when many periods are built. Operating at a relatively low current I limits the ohmic losses $\sim RI^2$ in the device, but this advantage is obtained at the cost of a larger external voltage. However even if a large number of periods N_p lowers the threshold current and the ohmic effects, the size of the heterostructure is limited by absorption and scattering losses which scale with the total size $L \sim L_p N_p$. The tradeoff between pros and cons gives typical values of $N_p = 10 \div 100$ for mid-IR QCLs and N_p up to 250 for THz QCLs.

1.5.3 QCL rate equations

A simple model of the gain region (see [1]) is useful to understand the physical parameters which govern the lasing in a QCL. Let us consider a one-level injector with a fixed sheet density per period n_g which is aligned with the upper level $n = 3$ of the next period (figure 7). Thus electrons are injected from the injector level to $n = 3$ at a rate J/e where J is the current density electrically pumping the system. Electrons can scatter from $n = 3$ to the lower levels $n = 2$ (by a radiative transition) and $n = 1$ or to the states of the continuum. So the total lifetime of the upper level is

$$\frac{1}{\tau_3} = \frac{1}{\tau_{31}} + \frac{1}{\tau_{32}} + \frac{1}{\tau_{escape}} \tag{73}$$

Level 2 is separated from the injector by an energy Δ and has a total lifetime τ_2. Its population may vary due to thermal fluctuations, so a thermal population should be included $n_2^{therm} = n_g e^{-\beta\Delta}$.
Let us S be the flux of photons per period and unit active region width. We consider monochromatic radiation at the frequency ω_{32} of the system transition. The rate equations of a single period are

$$\begin{aligned}
\frac{d}{dt} n_3 &= J/e - \frac{n_3}{\tau_3} - S g_c (n_3 - n_2) \\
\frac{d}{dt} n_2 &= \frac{n_3}{\tau_3} + S g_c (n_3 - n_2) - \frac{n_2 - n_2^{therm}}{\tau_2} \\
\frac{d}{dt} S &= \frac{c}{n_{refr}} \left[S \left(g_c (n_3 - n_2) - \alpha_{tot} \right) + \beta \frac{n_3}{\tau_{sp}} \right]
\end{aligned} \tag{74}$$

where the equation for the photon flux S takes into account the gain produced by the population inversion $g_c(n_3 - n_2)$ and the total modal losses in the period α_{tot}. The term $\beta \frac{n_3}{\tau_{sp}}$ represents the small fraction β of spontaneously emitted light from the upper level 3, which happens to be in the same direction of the flux S.
The gain cross-section g_c used in this model is taken for the whole active region of the lase, so it is proportional to the overlap factor which indicates the confinement of the optical mode in the gain medium

$$\Gamma = \frac{\int_{active\ region} |\mathbf{E}(\mathbf{r})|^2 d^3\mathbf{r}}{\int_{-\infty}^{\infty} |\mathbf{E}(\mathbf{r})|^2 d^3\mathbf{r}} \tag{75}$$

so that the gain-peak cross section (63) is used in the form:

$$g_c \to \Gamma g_c = \Gamma \frac{8e^2 \omega |z_{if}|^2}{c n_r \varepsilon_0 L_P} \frac{1}{\gamma_{32}} \tag{76}$$

The set of rate equations 74 can describe three regimes:

- below threshold:
  the flux of radiation is $S = 0$, the spontaneous emission is negligible and the steady-state population densities are:

$$\begin{cases} n_3 = \dfrac{J\tau_3}{e} \\ n_2 = \dfrac{J\tau_3}{e\tau_{32}}\tau_2 + n_2^{therm} \end{cases} \Rightarrow \Delta n = n_3 - n_2 = \frac{J}{e}\underbrace{\tau_3\left(1 - \frac{\tau_2}{\tau_{32}}\right)}_{\tau_{eff}} - n_2^{therm} \tag{77}$$

  in which an effective lifetime τ_{eff} can be defined. Inversion is possible only when $\tau_{eff} > 0$ i.e. $\tau_2 < \tau_{32}$

- at threshold:
  the amplification of radiation is beginning. The gain of the system compensates the total loss $\alpha_{tot} = \alpha_w + \alpha_m$ due to the waveguide and the mirrors:

$$\Gamma g_c \Delta n = \alpha_{tot} = \alpha_w + \alpha_m \tag{78}$$

  and using 77 one finds the threshold current density at which lasing starts:

$$J_{th} = \frac{e}{\tau_{eff}}\left(\frac{\alpha_{tot}}{\Gamma g_c} + n_2^{therm}\right) \tag{79}$$

- above threshold, gain is clamped at the value 78, so putting all the time-derivatives equal to zero the steady state behaviour is:

$$S = \frac{1}{\alpha_{tot}}\left(\frac{J}{e} - \frac{n_3}{\tau_3}\right) \quad \text{for } J > J_{th} \tag{80}$$

  which shows the flux grows linearly with the injected current $S \propto J$.

Unlike interband lasers, QCLs are limited in current by the onset of the negative differential resistance (NDR) up to J_{max}. This happens when the applied electric field makes the energy of the injector's lowest state resonant with the upper level 3 of the laser transition. If the bias is further increased, the injector gets a bit higher than the level 3, so the current drops.
Though real QCLs are generally based on a more complex structure of different levels and transitions, this model sheds a light on the interplay between the main parameters, such as gain, modal losses, transition linewidth, threshold current, thermal fluctuations. More refined models include a higher number of levels, the transport to the next period, the leakage of the injected current to levels different from the upper subband of the optical transition and other effects. This requires a full out-of-equilibrium treatement, which can be studied numerically.

1.5.4 Figures of merit of a QCL

The threshold current (eq. 79) is determined by the competition between the detrimental losses α_{tot} and the peak-gain cross section g_c, which should as high as possible. Experimentally it shows a weak dependence on the temperature that can be fitted by $J(T) = J_0 e^{T/T_0}$. In fact, as the temperature grows, the interaction of the electron with LO-phonons increases the population of the lower level of the transition and decreases the non-radiative lifetimes.
Other quantities which help assess the performance of a QCL are the optical power and its derivative over the current I, i.e. the slope efficiency. For a heterostructure of N_p

periods, the optical power grows with the injected current above threshold giving the following slope efficiency:

$$\frac{dP_{out}}{dI} = N_p \hbar \omega_{32} \alpha_{m1} \frac{dS}{dJ} \eta_{int} = \frac{N_p \hbar \omega_{32}}{e} \frac{\alpha_{m1}}{\alpha_{tot}} \eta_{int} \tag{81}$$

where α_{m1} represents the front mirror loss, which allows photons to escape from the device. η_{int} is the internal quantum efficiency which counts the percentage of electron transitions which contribute to the amplification of radiation and reaches $\eta_{int} \approx 1$ at best. In our three-level model, it can be computed as $\eta_{int} = \frac{\tau_{eff}}{\tau_{eff}+\tau_2}$.
The differential external quantum efficiency is defined as

$$\eta_{ext} \equiv \frac{e}{N_p \hbar \omega_{32}} \frac{dP_{out}}{dI} = \eta_{int} \frac{\alpha_{m1}}{\alpha_{tot}} \tag{82}$$

and weights the internal quantum efficiency with the extraction of light from the device. Finally the wallplug efficiency [11] describes how much electrical power $V_{max} I_{max}$ is converted into peak optical power P_{out}^{max}:

$$\eta_{wp} = \frac{P_{out}^{max}}{I_{max} V_{max}} = \frac{I_{max} - I_{th}}{I_{max}} \frac{dP_{out}/dI}{V_{max}} \tag{83}$$

at the maximum of the peak optical power. Wallplug efficiency can be viewed as an overall figure of merit of the device, because in order to have the highest η_{wp}, all other figures of merit need to be optimized. In the end the improvement of QCL performances strongly depends on the parameters of the active region and some general design rule can be outlined:

- small ratio τ_2/τ_{32} to ensure population inversion and low $J_{th} \propto \tau_{eff}^{-1} = \frac{1}{\tau_3}\left(1 - \frac{\tau_2}{\tau_{32}}\right)^{-1}$
- long lifetime τ_3 of the upper level of the laser transition
- narrow linewidth γ_{32} of the transition to increase g_c
- low waveguide losses α_w and good optical confinement $\Gamma \approx 1$

Thus the importance of a good lower state extraction efficiency, the efficient quenching of thermal electron escape from the upper state of the laser transition, the necessity to provide both low waveguide losses and good thermal extraction efficiency should be carefully considered.

1.5.5 Major active region designs of THz QCLs

The task of demostrating THz QCLs was harder than the mid-infrared for two reasons, both connected to the long wavelength of terahertz radiation. First, the small energy of the photons $\hbar\omega \approx 4 \div 20 meV$ create a difficult selective injection and extraction of electrons in/from the desired levels, since the subbands are closely spaced. This makes population inversion harder to achieve. Secondly, losses due to the absorption of radiation by free carriers scale with $\sim \lambda^2$ as we will see later. So waveguides have been developed to minimize the overlap of the optical modes with doped regions (figure 8).
The three major design classes of the active region are the "chirped superlattice" (CSL), the "bound-to-continuum" (BTC) and the "resonant-phonon" (RP) designs, though some "interlaced" structures have been used to merge the best features of the different schemes [9].

Chirped Superlattice

The heterostructure is built with several quantum wells coupled together to form minibands of states. The wells and barriers have gradually changing size along the growth direction to allow a properly enginereed alignment of the levels (see figure 8.a).
The radiative transition involves the lowest state of the upper miniband 2 and the highest state of the lower miniband 1. Population inversion is guaranteed by two mechanisms:

- the electron scattering is stronger between the tightly coupled states of the same miniband (intra-miniband scattering: $\tau \approx 1ps$) than the one between states of different minibands (inter-miniband scattering: $\tau \approx 10ps$). Thus electrons relax to the bottom of each miniband and tend to populate 2 and deplete 1.

- the carriers are injected in the lower state of the upper miniband, and population inversion and optical gain is achieved at the edges of the minigap. Because of the nature of the electron-phonon interaction that depends on the exchanged wavevector, the intersubband lifetime in a single quantum well will be almost identical (within 20%) to the one of a superlattice with a minigap of identical size. For this reason, the scattering rate between levels at the edges of the minigap tends to decrease with the number of wells N_{QW} in the superlattice, as the total rate must be shared between more and more lower levels. In addition, the lower state lifetime τ_2 is very short because electrons in the upper state of the lower miniband may scatter to any point the the lower miniband very efficiently. This is the so-called "phase-space argument" [1].

Typical values of the oscillator strength of the transition are $f_{21}^{CSL} \approx 2.5 \div 3$ for the CSL. In general, the period is $L_p \approx 100nm$. The Chirped Superlattice was the first design successfully used to demonstrate THz laser action in 2001 (see [12]).

Bound-to-continuum

The BTC design differs from the CSL mainly because the upper radiative state is engineered to lie in the forbidden minigap and to give place to a diagonal transition in real space. This means the states 1 and 2 have the maxima of their distribution localised in two adjiacent wells. The diminished overlap between the ψ_1 and ψ_2 lowers the oscillator strength to $f_{21}^{BTC} \approx 1.5 \div 2$. Conversely, there is an increase of the upper miniband lifetime due to a similar reduction of the non-radiative scattering rate. Even the injection of carriers is improved because the injector states are much better coupled to the upper state than to the lower miniband.
In the end the bound-to-continuum design has led to a general improvement of power efficiency and maximum operating temperature. Its period is $L_p \approx 110nm$ (figure 8.b).

Resonant-phonon

The resonant-phonon scheme exploits one of the main scattering mechanisms acting in a QCL. Lattice vibrations perturb the crystal periodicity so the electronic states are no longer eigenstates of the system and energy is exchanged between electrons and the lattice. The main contribution comes from the longitudinal optical (LO) phonons, which have very little dispersion around their average energy ($\hbar\omega_{LO} = 36meV$ in GaAs).
A collector/injector state is engineered to lie at an energy $\hbar\omega_{LO}$ below the lower radiative state 1 involved in the THz transition: electrons undergo fast sub-picosecond relaxation from 1 by emission of a LO-phonon. This selective phonon-assisted depopulation is obtained by creating a huge overlap between 1 and the collector/injector states of the

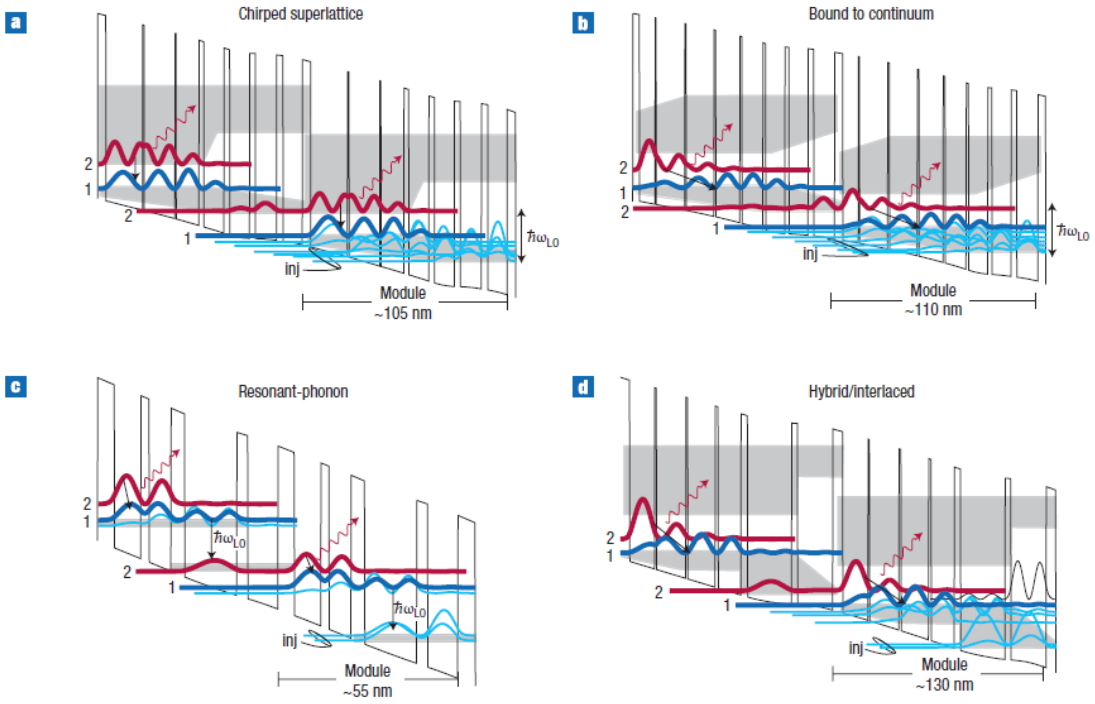

Figure 8: The examples shown are CSL (a), BTC (b), RP (c) and interlaced (d) designs. Two modules of each design are drawn, with the plot of the squared magnitude $|\chi(z)|^2$ of the different subband states. The red and blue lines are the upper and lower radiative subbands respectively. Grey shaded regions indicate minibands of states. [9]

adjiacent wells. Instead the upper state 2 is kept localised suppressing the scattering with the collector states, so that its lifetime is a few ps.
The mechanism very efficiently enhances the population inversion. The fine control of the wavefunctions' extension relies on the appropriate preparation of a few quantum wells in a repeated module with length $L_p \approx 55nm$ (figure 8.c). This means the RP design does not exploit minibands unlike the CSL and BTC schemes, so the typical oscillator strength is smaller $f_{21}^{RP} \approx 0.5 \div 1$. Indeed the resonant-phonon heterostructures can take advantage of the smaller period, since the gain is $g \propto L_p^{-1}$.

1.5.6 The role of doping

To provide the electrons necessary to observe the intersubband transitions, doping is needed in the gain medium of a QCL. When the donors (conventionally, silicon atoms) are placed in the semiconductor, the electron distribution is not uniform and creates an electrostatic potential which has a large effect when dopants are in the injection region. In fact, the electrons are transferred to the active well while the donors lie in the barrier material producing a strong modification of the potential. This increases the electron mobility and reduces the intersubband broadening, because impurities are spatially separated from the carriers.
This additional "Hartree potential" $V_H(z) = -e\Phi(z)$ is added to the QCL potential and treated in a mean-field approximation [8]:

$$\hat{H}_e = -\frac{\hbar^2\nabla^2}{2m^*} + \hat{V}_{QC}(z) + \hat{V}_H(z) \tag{84}$$

The local charge density is $\rho = eN_D(z) - e\sum_i n_i|\chi(z)|^2$ where $N_D(z)$ is the doping profile of ionized donors and n_i is the electron sheet density associated to the i-th subband. So Poisson's equation can be computed as:

$$\frac{\partial^2}{\partial^2 z}\Phi(z) = \frac{\rho(z)}{\varepsilon_0\varepsilon} \tag{85}$$

The subband densities are not known a priori, since they depend on the transport but the thermal Fermi-Dirac distribution is a good initial approximation, if the same chemical potential μ is used in every module of the QCL. Charge neutrality must be respected in each period:

$$\sum_i n_i = \int dz N_D(z) = n_s \tag{86}$$

since the surface impurity concentration must be equal to the overall electron sheet density n_s. As the density depends on the envelope functions $\chi_i(z)$, Poisson's and Schroedinger's equations have to be solved iteratively together, until the self-consistent approach converges.
The free carrier absorption (FCA) is a phenomenon related to the electrons provided by dopants, i.e. the promotion of an electron from an already-excited subband to a higher level. This can be evaluated with the semiclassical Drude model of free electrons of mass m^* undergoing a dumping γ. Doped semiconductors typically have $\gamma^{-1} = 100 \div 200 fs$. The susceptibility of a this system with a volume density n is

$$\chi_{fc} = -\frac{ne^2}{m^*\varepsilon_0}\frac{1}{\omega^2 + i\gamma\omega} \tag{87}$$

The complete dielectric response function must take into account the semiconductor susceptibility $\chi_{sc} = 1 - \varepsilon_{sc}$:

$$\varepsilon_r(\omega) = 1 + \chi_{sc} + \chi_{fc} = \varepsilon_{sc}\left(1 - \frac{\omega_p^2}{\omega^2 + i\gamma\omega}\right) \tag{88}$$

where the plasma frequency in the semiconductor is

$$\omega_p \equiv \sqrt{\frac{ne^2}{\varepsilon_0\varepsilon_{sc}m^*}} \tag{89}$$

The complex refractive index is $n_{refr}(\omega) = \sqrt{\varepsilon(\omega)} = n_r + in_i$ from which the absorption coefficient is:

$$\alpha_{fc} = 2\frac{2\pi n_i}{\lambda} = \frac{4\pi}{\lambda}\frac{\Im[\varepsilon_r(\omega)]}{n_r} \tag{90}$$

For frequencies much higher than ω_p, the real part n_r is almost constant, so that the free carrier absorption is

$$\alpha_{fc} \approx \frac{e^2}{4\pi^2c^2\varepsilon_0 n_r}\frac{\gamma n\lambda^2}{m^*} \propto n\lambda^2 \tag{91}$$

This result shows that this losses become more and more relevant for long wavelengths, so THz QCLs are more hindered by this effect than mid-IR QCLs. In order to limit these losses, doping should be very low, but at the same time it is essential for an efficient current injection in the device. A good compromise between these opposite requirements sets the usual doping level at $n \approx 10^{16} cm^{-3}$ at THz frequencies.
As a rule of thumb, dopants' diffusion from the injector to the active region during the growth should be as limited as possible. However, recent findings suggest that a strategical doping of the optically active zone could eventually improve the performance of QCLs [13].

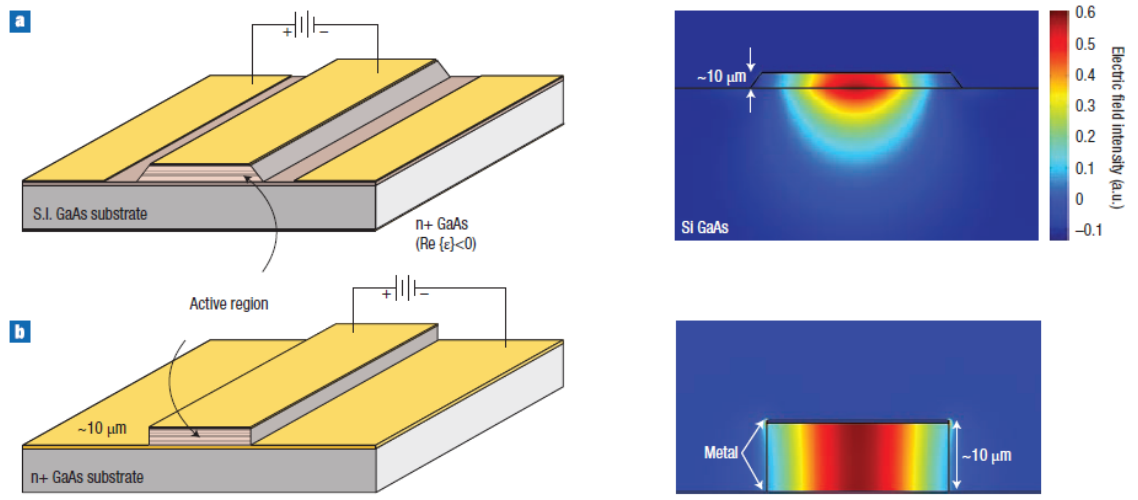

Figure 9: A comparison between the semi-insulating single-plasmon (a) and the double-metal (b) waveguides in the case of a ridge laser. On the right, the simulation of a THz electric field shows the different optical confinement provided by these structures. [9]

1.6 TERAHERTZ WAVEGUIDES

1.6.1 Main characteristics

In a QCL, light is confined both vertically by the sequence of epitaxial layers and in the horizontal plane, due to the refractive index difference between the laser's ridge or mesa and the surrounding domains. Due to the accurate control of the layer thickness during the growth process, light confinement is more efficient in the vertical direction.
A laser waveguide is characterised by

- the loss coefficient α_w, due to scattering and absorption processes in its volume
- the mirror loss coefficient α_m due finite reflectivity of the laser facets
- the optical confinement factor Γ (see 75) indicating the overlap of the electromagnetic mode with the gain medium.

In mid-infrared QCLs, waveguiding is provided by metallic or dielectric confinement, but the latter is highly impractical in the THz regime. In fact, dielectric confinement would require $100\mu m$-thick cladding layers which are even bigger than the typical $10\mu m$-high heterostructure itself. Moreover a larger doping would be needed to feed in current in the device, leading to huge optical losses dominated by free carrier absorption.
The solution is the exploitation of metallic or quasi-metallic confinement, for which two types of waveguides have been developed: the "semi-insulating surface-plasmon" (SI-SP or briefly SP) and the "double metal" (MM) designs (see figure 9).

1.6.2 Surface-plasmon waveguide

Using eq. 89, it can be seen that a heavily doped semiconductor layer ($N_D \approx 10^{18} cm^{-3}$) has a plasma frequency $\omega_p \approx 10\ THz$. So it exhibits an overall negative real part of the dielectric constant for all $\omega < 10\ THz$. Let us consider a plane wave propagating with a complex wavevector $k_z^2 = \varepsilon_i \left(\frac{\omega}{c}\right)^2 - \beta^2$. If at the interface between two materials the

dielectric constant changes sign along the growth direction **z**, the EM field exponentially decays in the layer with $\varepsilon_i = n_i^2 < 0$, due to the Helmholtz equations:

$$\left(\nabla^2 + \frac{\varepsilon_i \omega^2}{c^2}\right)\mathbf{H} = \beta^2 \mathbf{H} \qquad \left(\nabla^2 + \frac{\varepsilon_i \omega^2}{c^2}\right)\mathbf{E} = \beta^2 \mathbf{E} \tag{92}$$

with the boundary condition of continuous in-plane components H_x and E_y for TM-radiation [1]. In fact, a simplified model of a highly doped layer with $\varepsilon_d < 0$ for $z < 0$ and a material with $\varepsilon_s > 0$ for $z > 0$ has the solution

$$H(z) = \begin{cases} Ae^{qz} & \text{for } z < 0 \\ Be^{-hz} & \text{for } z > 0 \end{cases} \tag{93}$$

where $q = \sqrt{\beta^2 - \varepsilon_d(\omega/c)^2}$ and $h = \sqrt{\beta^2 - \varepsilon_s(\omega/c)^2}$. Imposing the boundary conditions, one finds $A = B$ and $Aq/\varepsilon_d = -Bh/\varepsilon_s$, which are compatible only if the dielectric constant changes sign across the interface. The result is a propagation constant affected by an effective index of refraction

$$\beta = \frac{\omega}{c}\sqrt{\frac{\varepsilon_s \varepsilon_d}{\varepsilon_s + \varepsilon_d}} \tag{94}$$

Setting the highly-doped semiconductor's $\varepsilon_d = (n_d + i\kappa_d)^2$ and the other material's $\varepsilon_s = n_s^2$ and assuming $|\varepsilon_d| > |\varepsilon_s|$, the absorption coefficient associated to the loss in a single-plasmon waveguide is

$$\alpha_w^{SP} = 2\Im(\beta) = \frac{4\pi}{\lambda}\frac{n_d n_s^3}{\kappa_d^3} \propto \frac{1}{\lambda} \tag{95}$$

The single plasmon losses scale as $\sim 1/\lambda$, which makes this confinement more convenient for THz QCLs than for mid-IR QCLs due to the longer wavelength of THz radiation, with typical losses of the order of $10cm^{-1}$.
This discussion demonstrates the principle of the surface-plasmon waveguide, which is built this way: a heavily doped semiconductor layer of $0.2 \div 0.8\mu m$ is grown underneath the $10\mu m$-thick active medium, but it is built on a semi-insulating GaAs substrate. This creates a compound sufrace-plasmon mode which is bound to both the top metallization and the lower plasma layer produced by doping [9].
The doped layer is sufficiently thin to confine THz radiation better than dielectric cladding, reaching $\Gamma = 0.1 \div 0.5$, yet the mode significantly extends over the intrinsic GaAs substrate: the absence of doping minimizes the free carrier absorption in this region.

1.6.3 Double metal waveguide

A MM waveguide uses two metal layers (typically Au) which are placed immediately above and below the epitaxyal active region by wafer bonding. The electromagnetic field is highly confined by the metallic surfaces, so that $\Gamma \approx 1$ and the vertical and lateral dimensions of the device can be made much smaller than λ. This helps reducing the thermal dissipation, the threshold current and gives a good high-temperature performance. Unfortunately the sub-wavelength nature of the MM waveguide affects the beam quality leading also to poor output power levels due to the larger mirror losses at the subwavelength facet.[9]. On the one hand there are huge diffractive effects, on the other hand there is an impedance mismatch between the mode inside the laser and in free space, so that only a small fraction ($5\% \div 20\%$) of photons goes out. In spite of the lack of significant doping, there are non-neglible losses by the metal and reabsorption by the gain medium that result in a higher absorption coefficient $\alpha_w^{MM} = 10 \div 60cm^{-1}$.

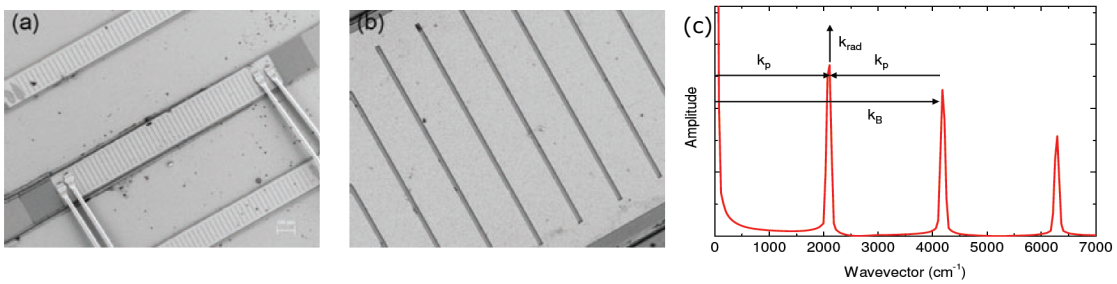

Figure 10: A THz QCL distributed-feedback resonator (a) with the top metallization patterned with a one-dimensional periodic grating (detail in b). The Fourier transform of the grating shows the Bragg peaks for the case $\Lambda = 30\mu m$ and the involved wavevectors (c). [14]

1.6.4 Distributed-feedback lasers

Due to the promising high-temperature performance and optimal Γ, a lot of effort has been made to improve the optical outcoupling and the far-field shape of the beam in MM waveguides. One of the most interesting approach is the use of surface-emitting devices, in which a specially designed pattern of scatterers (gratings, holes, etc. in the top metallization) allows vertical extraction of radiation. In a traditional QCL, this is impossible to achieve since intersubband transitions do not provide gain parallel to the growth direction and light propagates in the orthogonal plane. Instead, the implementation of photonic structures coupled to the active region overcomes this limit. Since the wavelength of the amplified THz radiation is much larger than the size of the scatterers, a mechanism of distributed feedback (DFB) takes place, so that the interplay between the modes in the whole resonator produces vertical emission.
The simpler example of such DFB devices is a one-dimensional periodic grating with characteristic length Λ (see figure 10), where Bragg diffraction has a central role. In fact, this structure is characterised by the wavevectors $k_B^{(m)} = 2\pi m/\Lambda$ ("Bragg peaks") for $m = 0, 1, 2, 3 \ldots$ They are evident in the grating's Fourier transform in figure 10.c. The photons are completely backscattered if their wavevector k_P is such that the condition $k_P = nk_B - k_P$ is fulfilled, where n is an integer called order of the grating. In general, surface emission of light with free space wavevector $|k_{rad}| = \omega/c$ is obtained if the following relation holds [14]:

$$|k_{rad}| \sin\theta = |k_b - k_P| \quad \text{for} \quad \theta < \pi/2 \tag{96}$$

In a second order grating, the first Bragg peak is $k_B = k_P$ and the in-plane components cancel each other. This forces the extraction angle to be $\theta = 0$, leading to vertical emission. The same mechanism of distributed feedback works in more complicated geometries, which have attracted more and more attention in the last years. In fact, an accurate design of the feedback structure can significantly improve lasing threshold, output power and beam pattern. This is the main motivation of the present thesis that I will discuss in detail in the next chapter.

2 PHOTONIC STRUCTURES

Optical interference is a fundamental phenomenon exploited in a wide variety of fields of physics and technological applications, for example the enhancement of device performance in photonics. In fact, complete control over light propagation can be obtained through the appropriate preparation of systems with different low-loss dielectric media. If refractive indices of these regions are sufficiently different and and the absorption of light is minimal, then the interplay between refractions and reflections of light across all the interfaces strongly affects the propagation of the electromagnetic radiation, both in its spatial distribution and its frequency. To this aim, for a long time mainly periodic structures have been proposed, but a recent surge of interest has brought aperiodic photonic structures in the spotlight. As we will see, their deviation from periodicity may result into a large variety of possible geometries, characterised by a higher degree of flexibility and richness of effects when compared to their periodic counterparts [2].

2.1 LIGHT PROPAGATION IN MIXED DIELECTRIC MEDIA

Let us consider the macroscopic electric field $\mathbf{E}$, the magnetic field $\mathbf{H}$, the electric displacement $\mathbf{D}$ and the magnetic induction $\mathbf{H}$. The macroscopic Maxwell equations are

$$\begin{aligned} \nabla \cdot \mathbf{D} &= \rho & \nabla \times \mathbf{E} &= -\partial_t \mathbf{B} \\ \nabla \cdot \mathbf{B} &= 0 & \nabla \times \mathbf{H} &= \mathbf{J} + \partial_t \mathbf{D} \end{aligned} \tag{97}$$

where $\mathbf{J}$ is the current density in the system and ρ is the charge density. In a system made up of homogeneous regions with different dielectric constant (figure 11), we can set $\varepsilon = \varepsilon(\mathbf{r})$ and restrict to the case where no source terms exist: $\mathbf{J} = 0$ and $\rho = 0$ [15]. The electric displacement can be written as a power series expansion in the electric components E_i:

$$D_i = \varepsilon_0 \sum_j \varepsilon_{ij} E_j + o(E_i^2) \tag{98}$$

where $\varepsilon_0 \approx 8.85\ 10^{-12} F/m$ is the vacuum permittivity. Four essential hypoteses will be introduced:

- the response of the system is linear in the electric field, so higher order terms can be neglected in 98
- the material is isotropic, thus the permittivity tensor ε_{ij} is actually a scalar dielectric function, giving $\mathbf{D}(\mathbf{r}, \omega) = \varepsilon(\mathbf{r}, \omega)\mathbf{E}(\mathbf{r}, \omega)$
- the dielectric dispersion in frequency can be ignored, chosing a dielectric constant $\varepsilon(\mathbf{r}, \omega) \approx \varepsilon(\mathbf{r})$ appropriate to the spectral range of interest
- the material is transparent, which means that $\varepsilon(\mathbf{r})$ is real and positive.

Under these approximations, one finds

$$\mathbf{D}(\mathbf{r}) = \varepsilon_0 \varepsilon(\mathbf{r}) \mathbf{E}(\mathbf{r}) \tag{99}$$

Similarly, the magnetic and induction fields are related by

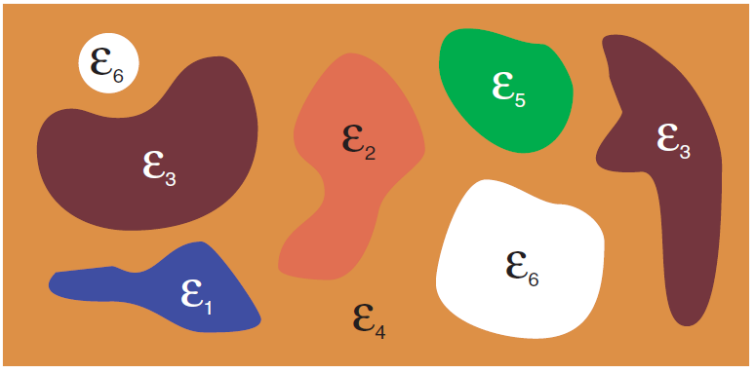

Figure 11: An example of mixed dieletric medium made up of different homogeneous regions. [15]

$$\mathbf{B}(\mathbf{r}) = \mu_0 \mu(\mathbf{r}) \mathbf{H}(\mathbf{r}) \tag{100}$$

in which $\mu_0 = 4\pi\ 10^{-7} Henry/m$ and $\mu(\mathbf{r})$ is the relative magnetic permeability (nearly 1 for most materials). Thus, the refractive index of a composite dielectric material is a function of space

$$n(\mathbf{r}) = \sqrt{\mu(\mathbf{r})\varepsilon(\mathbf{r})} \approx \sqrt{\varepsilon(\mathbf{r})} \tag{101}$$

Though these assumptions of linear and lossless materials may appear unnecessarily strict, many interesting and useful properties of such systems arise from their linear response. Thus the Maxwell equations 97 then reduce to:

$$\begin{aligned} \nabla \cdot [\varepsilon(\mathbf{r})\mathbf{E}(\mathbf{r},t)] &= 0 \qquad & \nabla \times \mathbf{E}(\mathbf{r},t) &= -\mu_0 \partial_t \mathbf{H}(\mathbf{r},t) \\ \nabla \cdot \mathbf{H}(\mathbf{r},t) &= 0 & \nabla \times \mathbf{H}(\mathbf{r},t) &= \varepsilon_0 \varepsilon(\mathbf{r}) \partial_t \mathbf{E}(\mathbf{r},t) \end{aligned} \tag{102}$$

The spatial and time dependence of the fields $\mathbf{E}(\mathbf{r},t)$ and $\mathbf{H}(\mathbf{r},t)$ can be decomposed into Fourier components extracting the time-dependent part, no matter how complex these functions are, using the so-called "harmonic modes" of the type:

$$\begin{aligned} \mathbf{H}(\mathbf{r},t) &= \mathbf{H}(\mathbf{r}) e^{-i\omega t} \\ \mathbf{E}(\mathbf{r},t) &= \mathbf{E}(\mathbf{r}) e^{-i\omega t} \end{aligned} \tag{103}$$

Inserting this expansion in Maxwell equations, the divergence formulas $\nabla \cdot \mathbf{H}(\mathbf{r}) = 0$ and $\nabla \cdot [\varepsilon(\mathbf{r})\mathbf{E}(\mathbf{r})] = 0$ indicate the absence of point sources or sinks for the displacement and magnetic fields. The curl equations instead highlight the connection between $\mathbf{E}(\mathbf{r})$ and $\mathbf{H}(\mathbf{r})$:

$$\begin{aligned} \nabla \times \mathbf{E}(\mathbf{r}) - i\omega\mu_0 \mathbf{H}(\mathbf{r}) &= 0 \\ \nabla \times \mathbf{H}(\mathbf{r}) + i\omega\varepsilon_0 \mathbf{E}(\mathbf{r}) &= 0 \end{aligned} \tag{104}$$

Since the vacuum speed of light is $c = 1/\sqrt{\mu_0 \varepsilon_0}$, one finds:

$$\begin{aligned} \mathbf{E}(\mathbf{r}) &= \frac{i}{\omega \varepsilon_0 \varepsilon(\mathbf{r})} \nabla \times \mathbf{H}(\mathbf{r}) \\ \hat{\Theta}(\mathbf{r})\mathbf{H}(\mathbf{r}) &\equiv \nabla \times \left[\frac{1}{\varepsilon(\mathbf{r})} \nabla \times \mathbf{H}(\mathbf{r}) \right] = \left(\frac{\omega}{c} \right)^2 \mathbf{H}(\mathbf{r}) \end{aligned} \tag{105}$$

where we define the linear differential operator $\hat{\Theta}(\mathbf{r})$ to formulate the electrodynamics eigenvalue problem

$$\hat{\Theta}(\mathbf{r})\mathbf{H}(\mathbf{r}) = \left(\frac{\omega}{c} \right)^2 \mathbf{H}(\mathbf{r}) \tag{106}$$

This master equation is solved by the spatial patterns $\mathbf{H}(\mathbf{r})$ of the magnetic field which which are eigenfunctions for the system, with the corresponding eigenvalue ω^2/c^2.
The interesting and powerful properties of such mathematical formulation are now briefly introduced. Let us consider the complex vector fields $\mathbf{F}(\mathbf{r}), \mathbf{G}(\mathbf{r})$ belonging to a vector space $\mathcal{V}$. The scalar product between the two over the volume Ω is defined as:

$$\langle \mathbf{F}|\mathbf{G}\rangle \equiv \int_\Omega d^3\mathbf{r}\, \mathbf{F}^*(\mathbf{r})\mathbf{G}(\mathbf{r}) \tag{107}$$

The vector space $\mathcal{V}$ with the product $\langle|\rangle$ is a Hilbert space $\mathcal{H}$. An operator $\hat{\Pi} : \mathcal{H} \to \mathcal{H}$ is hermitian if its action on two generic vector fields is $\langle \hat{\Pi}\mathbf{F}|\mathbf{G}\rangle = \langle \mathbf{F}|\hat{\Pi}\mathbf{G}\rangle$. From the hermitian spectral theorem and the theory of linear algebra, the eigenfunctions of an hermitian operator $\{\mathbf{H}_i\}_i$ form a complete set, have real eigenvalues and are orthogonal, i.e. $\langle \mathbf{H}_i|\mathbf{H}_j\rangle = 0$ for $i \neq j$ if they have different eigenvalues. In particular, every vector field can be written as a linear combination of the type $\mathbf{F} = \sum_i \alpha_i \mathbf{H}_i$.
This discussion applies to our physical case where the vector fields are the magnetic ones, in fact the operator $\hat{\Theta}(\mathbf{r})$ is hermitian[1]. There exists a complete set of eigenfunctions $\{\mathbf{H}_n(\mathbf{r})\}_n$ with eigenvalues $(\omega_n/c)^2$, so that every magnetic field in the system can be expanded as:

$$\mathbf{H}(\mathbf{r}, t) = \sum_n \alpha_n \mathbf{H}_n(\mathbf{r}) e^{-i\omega_n t} \tag{108}$$

with the costraint $\nabla \cdot \mathbf{H}_n(\mathbf{r}, t) = 0$. A similar master equation for the displacement field $\mathbf{D}$ can be found , but it is not hermitian, unlike 106. So it is computationally convenient to work with $\mathbf{H}(\mathbf{r})$ first and then calculate $\mathbf{E}(\mathbf{r})$ and $\mathbf{D}(\mathbf{r})$, each taken as a complex field. However, one should always remember that the quantities of physical interest are their real parts only.
When dealing with macroscopic systems, the absence of a fundamental length in Maxwell equations produces the scale invariance of the master equation. In fact, the transformation of the space coordinate $\mathbf{r} \to \mathbf{r}' = s\mathbf{r}$ and $\nabla \to \nabla' = \nabla/s$ results in:

$$\nabla' \times \left(\frac{1}{\varepsilon'(\mathbf{r}')} \nabla \times \mathbf{H}(\mathbf{r}'/s) \right) = \left(\frac{\omega}{cs} \right)^2 \mathbf{H}(\mathbf{r}'/s) \tag{109}$$

defining $\varepsilon'(\mathbf{r}') \equiv \varepsilon(\mathbf{r}'/s)$. This means that the new mode profile $\mathbf{H}'(\mathbf{r}') = \mathbf{H}(\mathbf{r}'/s)$ and its frequency $\omega' = \omega/s$ can be obtained by simply rescaling the old solution. Thanks to this powerful feature, the solution at one length scale fully determines the solutions at every length scale.
Moreover, rescaling the dielectric function with $\varepsilon(\mathbf{r}) \to \varepsilon'(\mathbf{r}) = \varepsilon(\mathbf{r})/s^2$ does not change the shape of $\mathbf{H}(\mathbf{r})$, but changes its frequency $\omega \to \omega' = s\omega$.
It is worth noticing that this formulation of the electrodynamics in mixed dielectric media has a clear analogy with the quantum mechanical formalism (see table 1). In quantum mechanics, solving Schroedinger equation leads to a truly complex scalar wavefunction $\psi(\mathbf{r})$, while the electromagnetic problem gives the real part of a vector field $\mathbf{H}(\mathbf{r})$, treated as a complex quantity for computational convenience only.
In the case of a separable quantum potential, i.e. decomposed as $V(\mathbf{r}) = V_x(x) + V_y(y) + V_z(z)$, one can factorize $\psi(\mathbf{r}) = X(x)Y(y)Z(z)$ as the product of three independent functions and often find an analytical solution. Instead the operator $\hat{\Theta}(\mathbf{r})$ couples the

[1] This can be shown by double integration by parts over the volume Ω, assuming either vanishing fields at the boundaries of the volume $\partial\Omega$ or periodic conditions:

$$\langle \mathbf{F}|\hat{\Theta}\mathbf{G}\rangle = \int d^3\mathbf{r}\, \mathbf{F}^* \cdot \nabla \times \left(\frac{1}{\varepsilon} \nabla \times \mathbf{G} \right) = \int d^3\mathbf{r} (\nabla \times \mathbf{F})^* \cdot \frac{1}{\varepsilon} \nabla \times \mathbf{G} = \int d^3\mathbf{r} \left[\nabla \times \left(\frac{1}{\varepsilon} \nabla \times \mathbf{F} \right) \right]^* \cdot \mathbf{G} = \langle \hat{\Theta}\mathbf{F}|\mathbf{G}\rangle$$

	Quantum Mechanics	Electrodynamics
Field	$\psi(\mathbf{r},t) = \psi(\mathbf{r})e^{-iEt/\hbar}$	$\mathbf{H}(\mathbf{r},t) = \mathbf{H}(\mathbf{r})e^{-i\omega t}$
Eigenvalue problem	$\hat{H}\psi = E\psi$	$\hat{\Theta}\mathbf{H} = \frac{\omega^2}{c^2}\mathbf{H}$
Hermitian operator	$\hat{H} = -\frac{\hbar}{2m}\nabla^2 + \hat{V}(\mathbf{r})$	$\hat{\Theta} = \nabla \times \frac{1}{\varepsilon(\mathbf{r})}\nabla\times$

Table 1: Comparison between the formalism of Quantum Mechanics and of Electrodynamics in mixed dielectric media

three spatial coordinates even in the simple case when the dielectric function $\varepsilon(\mathbf{r})$ is separable, so the master equation is rarely solved analytically and numerical tools are required.

2.2 TYPES OF PHOTONIC STRUCTURES

As seen in section 2.1, light propagation in a mixed dielectric medium is determined by the form of the dielectric function $\varepsilon(\mathbf{r})$. This means that the allowed magnetic and electric field can be engineered both in their spatial pattern and spectrum by an appropriate preparation of the system. When such photonic structures are superimposed to the gain medium of a QCL, they control the properties of the emitted light. On the one hand, the photonic structure selects the permitted frequencies $\nu = \omega/2\pi$ within the active region's gain bandwidth; on the other one, it defines the shape of $\mathbf{H}(\mathbf{r})$ and $\mathbf{E}(\mathbf{r})$ at the surface of the device, thus determining the far-field pattern of emission.
There is a variety of possible solutions, for example the use of one-, two- or three-dimensional arrangement of regions ("scatterers") with refractive index different from that of the surrounding material. A widely used classification (see [2]) for such systems is the following:

- photonic crystals (PC): as shown in the examples of figure 12, they are characterised by discrete translational invariance. By analogy with crystalline solids, this induces photonic band gaps, preventing light from propagating in certain directions and at selected frequencies;

- aperiodic deterministic structures: although they lack translational symmetry, they still show long-range order, dictated by their generation rule. These include photonic quasicrystals (PQC) which are characterised by a peculiar control of the allowed electromagnetic modes;

- amorphous or random structures: no deterministic algorithm can produce such irregular geometries. When they are implemented in optical media, they give raise to multiple scattering of light.

The main properties of some of these structure will be analysed in the next sections, highlighting how they can be used to manipulate the light emitted by a QCL.

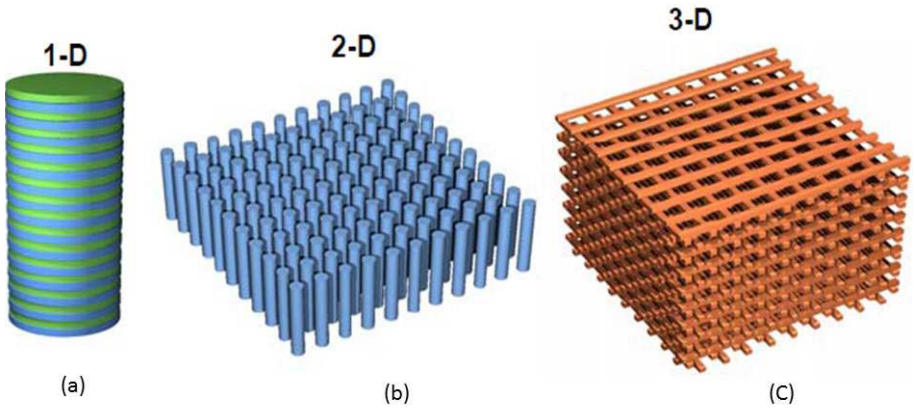

Figure 12: Examples of photonic crystals in 1D (a), 2D (b) and 3D (c) systems [16]

2.3 PHOTONIC CRYSTALS

2.3.1 Master equation in a periodic system

A photonic crystal (PC) is a structure characterised by a periodic modulation of the refractive index $n(\mathbf{r})$, or equivalently $\varepsilon(\mathbf{r})$. The three-dimensional case will be discussed, but the low-dimensional systems are analogous. PCs possess a discrete traslational invariance so that their refractive index $n(\mathbf{r}) = n(\mathbf{r}+\mathbf{R})$, where $\mathbf{R}$ can be expressed as a linear combination of three non coplanar vectors $\mathbf{v}_1, \mathbf{v}_2, \mathbf{v}_3$, called fundamental translational vectors:

$$\mathbf{R} = m_1\mathbf{v}_1 + m_2\mathbf{v}_2 + m_3\mathbf{v}_3 \tag{110}$$

where m_1, m_2, m_3 are any integer numbers. This defines an infinite set of mathematical points called "Bravais lattice" $\mathcal{B}$, whose primitive cell is the parallelepiped formed by $\mathbf{v}_1, \mathbf{v}_2, \mathbf{v}_3$. The whole structure is constructed by the repetition of such cell, translated by a vector of the Bravais lattice. Its physical realization consists in arranging a finite number of dielectric scatterers in the positions indicated by a subset of the lattice vectors.
The periodicity of $n(\mathbf{r})$ implies that the operator $\hat{\Theta}(\mathbf{r})$ defined in equation 105 is periodic too, so that $\hat{\Theta}(\mathbf{r}) = \hat{\Theta}(\mathbf{r}+\mathbf{R})$ for every $\mathbf{R} \in \mathcal{B}$. Using the same scheme of the Bloch theorem in solid state physics, the magnetic normal modes can be decomposed as

$$\mathbf{H}_{n,\mathbf{k}} = \mathbf{u}_{n,\mathbf{k}}(\mathbf{r})e^{i\mathbf{kr}} \tag{111}$$

in which $\mathbf{u}_{n,\mathbf{k}}(\mathbf{r}) = \mathbf{u}_{n,\mathbf{k}}(\mathbf{r}+\mathbf{R})$ is a function with the same periodicity as the lattice. The wavevector $\mathbf{k}$ belongs to the reciprocal lattice $\mathcal{R}$, which is the dual of the real space lattice. Its fundamental vectors $\mathbf{g}$ are defined by the relation $\mathbf{g}_i = 2\pi\mathbf{v}_j \times \mathbf{v}_k / V$, where V is the volume of the primitive cell. Due to the periodic boundary conditions, the eigenvalue problem can be restricted to the finite volume of a single unit cell of the photonic crystal, leading to a discrete spectrum of eigenvalues. So at every value of $\mathbf{k}$, an infinite sets of modes with discretely spaced frequencies $\omega_n(\mathbf{k})$ appears. These eigenvalues vary continuously as $\mathbf{k}$ varies, thus forming a family of continuous functions indexed by tha band number n: this is the band structure of a photonic crystal.
One key fact about this formulation is that two Bloch states differing by a reciprocal vector $\mathbf{K}$ are physically identical, thus even the mode frequency must be periodic: $\omega_n(\mathbf{k}+\mathbf{K}) = \omega_n(\mathbf{k})$. Thanks to the discrete translational symmetry, we can then exclude the redundant reciprocal vectors which do not give distinct states and focus on the first Brillouin zone (BZ) of the reciprocal space. Using the expression 111, the eigenvalue

problem 106 is transformed into the study the action of a $\mathbf{k}$-parametric operator $\hat{\Theta}_{\mathbf{k}}(\mathbf{r})$ on $\mathbf{u}_{n,\mathbf{k}}$ only:

$$\hat{\Theta}_{\mathbf{k}}(\mathbf{r})\mathbf{u}_{n,\mathbf{k}}(\mathbf{r}) \equiv \left[(i\mathbf{k}+\nabla)\times\frac{1}{\varepsilon(\mathbf{r})}(i\mathbf{k}+\nabla)\times\right]\mathbf{u}_{n,\mathbf{k}}(\mathbf{r}) = \frac{\omega_n^2(\mathbf{k})}{c^2}\mathbf{u}_{n,\mathbf{k}}(\mathbf{r}) \tag{112}$$

since $\nabla\times[\mathbf{u}_{n,\mathbf{k}}(\mathbf{r})e^{i\mathbf{kr}}] = e^{i\mathbf{kr}}[(\nabla+i\mathbf{k})\times\mathbf{u}_{n,\mathbf{k}}(\mathbf{r})]$. In addition to the eigenequation , $\mathbf{u}_{n,\mathbf{k}}(\mathbf{r})$ must also satisfy the transversality costraint

$$(i\mathbf{k}+\nabla)\cdot\mathbf{u}_{n,\mathbf{k}}(\mathbf{r}) = 0 \tag{113}$$

deriving from the Maxwell equation $\nabla\cdot\mathbf{H}_{n,\mathbf{k}}(\mathbf{r}) = 0$.
If other symmetries characterise the system (i.e., invariance under rotation, mirror reflection, inversion etc.), they prove powerful in symplifying the problem. In fact, when the system is left unchanged by a certain transformation, the transformed mode are again allowed physical solutions and the corrisponding $\omega_n(\mathbf{k})$ functions have the same symmetry as well. The collection of these symmetry operations is called the point group of the photonic crystal. The smallest region within the Brilloiun zone for which the $\omega_n(\mathbf{k})$ are not related by such symmetries is the irreducible Brillouin zone. So the calculations can be restricted to this smaller domain in the reciprocal space, reducing the computational effort.

2.3.2 The plane-wave method

Among the different solving approaches, a widely used technique is to represent the unknown function as a series expansion in a complete basis set of smooth functions (see reference [15], appendix D). Usually a Fourier series is chosen, so it is called plane-wave method in the case of two- and threedimensional systems.
Since $\mathbf{u}_{n,\mathbf{k}}(\mathbf{r})$ has the same periodicity of the lattice, it can be written as a multidimensional Fourier series:

$$\mathbf{u}_{n,\mathbf{k}}(\mathbf{r}) = \sum_{\mathbf{G}}\mathbf{D}_{\mathbf{G}}^{(n)}(\mathbf{k})e^{i\mathbf{G}\cdot\mathbf{r}} \tag{114}$$

where the sum is over all of the reciprocal lattice vectors $\mathbf{G}$ and the Fourier coefficients $\mathbf{D}_{\mathbf{G}}^{(n)}(\mathbf{k})$ are vectors as well. Using the expansion 114, the eigenvalue problem 112 can be Fourier transformed by integrating in $\int d^3\mathbf{r}\, e^{-i\mathbf{G}'\cdot\mathbf{r}}$. This results in an infinite set of equations for the coefficients:

$$\sum_{\mathbf{G}}\left[-\varepsilon^{-1}_{\mathbf{G}-\mathbf{G}'}(\mathbf{k}+\mathbf{G}')\times(\mathbf{k}+\mathbf{G})\times\right]\mathbf{D}_{\mathbf{G}}^{(n)}(\mathbf{k}) = \frac{\omega_n^2(\mathbf{k})}{c^2}\mathbf{D}_{\mathbf{G}'}^{(n)}(\mathbf{k}) \tag{115}$$

Here $\varepsilon^{-1}_{\mathbf{G}-\mathbf{G}'}$ indicates the series coefficients of Fourier transform of the inverse dielectric function, given by:

$$\varepsilon^{-1}_{\mathbf{G}-\mathbf{G}'} = \int_V d^3\mathbf{r}\frac{1}{\varepsilon(\mathbf{r})}e^{-i(\mathbf{G}'-\mathbf{G})\cdot\mathbf{r}}\sum_i e^{i\mathbf{k}\cdot\mathbf{R}_i} \tag{116}$$

where the summation is over all the crystal sites $\mathbf{R}_i$. Due to the transversality condition 113, the costraint $(\mathbf{k}+\mathbf{G})\cdot\mathbf{D}_{\mathbf{G}}^{(n)}(\mathbf{k}) = 0$ is respected. Thus there are two perpendicular unit vectors $\hat{\mathbf{e}}_{\mathbf{G}}^{(1)}$ and $\hat{\mathbf{e}}_{\mathbf{G}}^{(2)}$ orthogonal to $\mathbf{k}+\mathbf{G}$. Defining the projections of the Fourier components as $D_{\mathbf{G},1}^{(n)}(\mathbf{k}) = \langle\hat{\mathbf{e}}_{\mathbf{G}}^{(1)}|\mathbf{D}_{\mathbf{G}}^{(n)}(\mathbf{k})\rangle$ and $D_{\mathbf{G},2}^{(n)}(\mathbf{k}) = \langle\hat{\mathbf{e}}_{\mathbf{G}}^{(2)}|\mathbf{D}_{\mathbf{G}}^{(n)}(\mathbf{k})\rangle$, the following expression holds:

$$\mathbf{u}_{n,\mathbf{k}}(\mathbf{r}) = \sum_{\mathbf{G}}\left(D_{\mathbf{G},1}^{(n)}(\mathbf{k})\hat{\mathbf{e}}_{\mathbf{G}}^{(1)} + D_{\mathbf{G},2}^{(n)}(\mathbf{k})\hat{\mathbf{e}}_{\mathbf{G}}^{(2)}\right)e^{i\mathbf{G}\cdot\mathbf{r}} \tag{117}$$

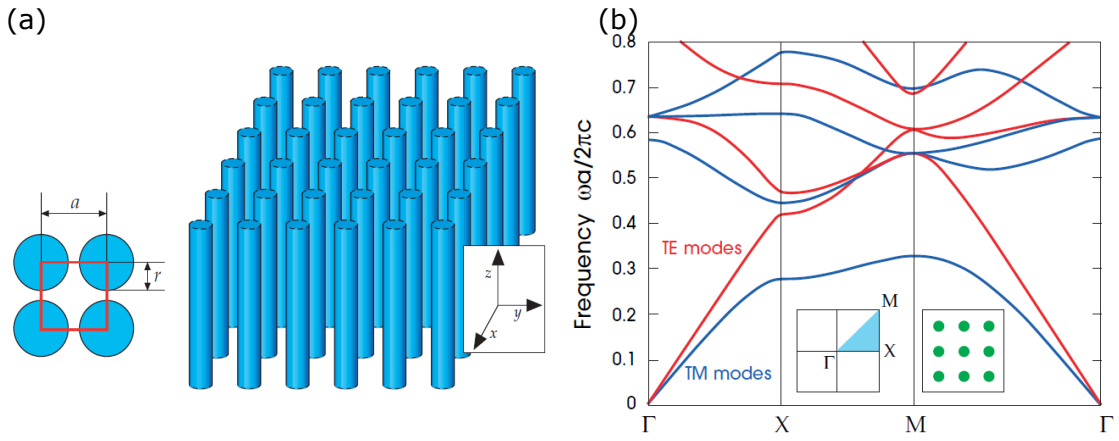

Figure 13: A square photonic crystals of dielectric rods embedded in air, with radius r and lattice parameter a, is illustrated in (a). The photonic band structure $\omega_n(\mathbf{k})$ (b) is calculated for the case $FF = r/a = 0.2$, $\varepsilon_{rod} = 8.9$ and $\varepsilon_{air} = 1$. The plot is computed for in-plane wavevectors $\mathbf{k}_{||}$ in the irreducible Brillouin zone, highlighted in blue in the inset. The frequencies are reported in the dimensionless unit $\omega a/2\pi c$. TM modes are in blue, while TE modes are red. [15]

Thanks to this decomposition, an alternative form for the system of equations 115 can be found:

$$-\sum_{j=1,2}\sum_{\mathbf{G}}\varepsilon^{-1}_{\mathbf{G}-\mathbf{G}'}\,\hat{\mathbf{e}}^{(i)}_{\mathbf{G}}\cdot[(\mathbf{k}+\mathbf{G}')\times(\mathbf{k}+\mathbf{G})\times\hat{\mathbf{e}}^{(j)}_{\mathbf{G}}]D^{(n)}_{\mathbf{G},j}(\mathbf{k}) = \frac{\omega_n^2(\mathbf{k})}{c^2}D^{(n)}_{\mathbf{G}',i}(\mathbf{k})\hat{\mathbf{e}}^{(i)}_{\mathbf{G}'} \tag{118}$$

Solving these equations to obtain the band structure $\omega_n(\mathbf{k})$ of the photonic crystal is often computationally expensive. Even if the series can be truncated at some point taking a finite set of plane waves, knowing the exact transform of $\frac{1}{\varepsilon(\mathbf{r})}$ remains a problem. The use of Fast Fourier Transform (FFT) algorithms speeds up the calculation of a multidimensional discrete Fourier transform. In fact, when the Fourier transform is approximated as a sum over N points, the computation time grows as $\sim N \log N$ and the required data storage scales with $\sim N$, making this method very efficient.

2.3.3 Two-dimensional photonic crystals

Two-dimensional photonic structures are the typical solutions used with a QCL, since they can be implemented by patterning the upper surface of the active region. So it is interesting to examine the behaviour of light in this particular systems. They are periodic along the two axes $\hat{\mathbf{x}}$ and $\hat{\mathbf{y}}$ and homogeneous along the third direction $\hat{\mathbf{z}}$. Assuming the system is infinite along $\hat{\mathbf{z}}$, the modes must be oscillatory in that direction with no restriction on the value of k_z. Since the dielectric function $\varepsilon(\mathbf{r})$ has a discrete translational invariance in the horizontal plane, we can focus on the in-plane momentum $\mathbf{k}_{||} = (k_x, k_y)$ restricted to the Brillouin zone. The modes can be indexed by n (for growing frequencies), k_z and $\mathbf{k}_{||}$:

$$\mathbf{H}_{(n,k_z,\mathbf{k}_{||})}(\boldsymbol{\rho}) = e^{ik_z z}e^{i\mathbf{k}_{||}\cdot\boldsymbol{\rho}}\mathbf{u}_{(n,k_z,\mathbf{k}_{||})}(\boldsymbol{\rho}) \tag{119}$$

where $\boldsymbol{\rho} = (x, y)$ and $\mathbf{u}_{(n,k_z,\mathbf{k}_{||})}(\boldsymbol{\rho})$ is a vector function with the same periodicity as the crystal.

The modes propagating strictly parallel to the $x-y$ plane (with $k_z = 0$) are invariant under reflections throug the $x-y$ plane. This mirror symmetry allows distinguishing between two types of polarizations. Transverse-electric (TE) modes have $\mathbf{H} = H(\boldsymbol{\rho})\hat{\mathbf{z}}$

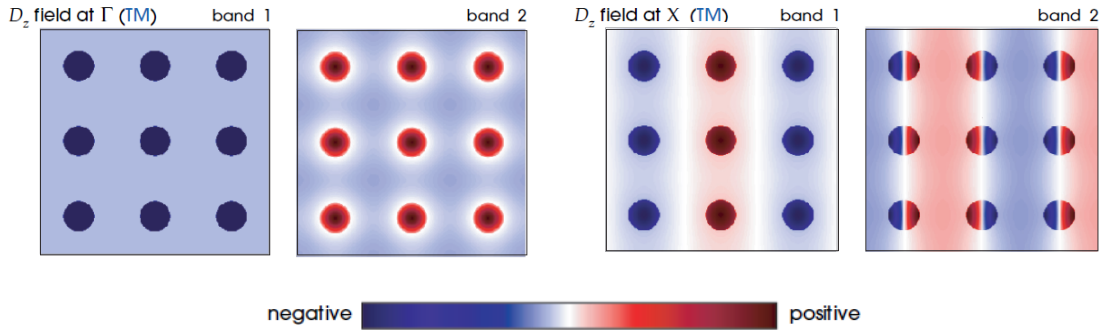

Figure 14: The electric displacement components D_z of TM modes are simulated in a square array of dielectric columns ($\varepsilon = 8.9$) in air, having $FF = 0.2$. The color indicates the amplitude of D_z. The reported plots refer to the fields of band 1 and 2 at the Γ (left) and X (right) points of the irreducible Brillouin zone. [15]

normal to the plane and $\mathbf{E}(\boldsymbol{\rho}) \cdot \hat{\mathbf{z}} = 0$ lying in the plane, while transverse-magnetic (TM) modes have just the reverse $\mathbf{E} = E(\boldsymbol{\rho})\hat{\mathbf{z}}$ and $\mathbf{H}(\boldsymbol{\rho}) \cdot \hat{\mathbf{z}} = 0$. Thus in order to separate the two polarizations in the eigenvalue problem, it is convenient to chose $\hat{\mathbf{e}}_1 \perp \hat{\mathbf{z}}$ and $\hat{\mathbf{e}}_2 \parallel \hat{\mathbf{z}}$. In this way, equation 118 contains a simpler term:

$$\hat{\mathbf{e}}_{\mathbf{G}}^{(i)} \cdot \left[(\mathbf{k}+\mathbf{G}') \times (\mathbf{k}+\mathbf{G}) \times \hat{\mathbf{e}}_{\mathbf{G}}^{(j)}\right] = \begin{cases} |\mathbf{k}+\mathbf{G}'| \cdot |\mathbf{k}+\mathbf{G}| & \text{(TM)} \\ (\mathbf{k}+\mathbf{G}') \cdot (\mathbf{k}+\mathbf{G}) & \text{(TE)} \end{cases} \tag{120}$$

In general, the photonic band structure for the two polarizations can be very different, as illustrated by the example in figure 13. The system is a square array of dielectric columns in air, having a radius r and a lattice parameter a. A very important parameter for 2D photonic structures is the filling factor $FF \equiv r/a$, containing information on both the concentration and the size of the scatterers. Moreover, the refractive index contrast between the materials is crucial too. In the reported case, the study can be limited by symmetry to the irriducible Brillouin zone, characterised by the special points Γ ($\mathbf{k}_{||} = 0$), X ($\mathbf{k}_{||} = \pi/a\hat{\mathbf{x}}$) and M ($\mathbf{k}_{||} = \pi/a(\hat{\mathbf{x}} + \hat{\mathbf{y}})$).
The TM modes show a complete band gap between the first and the second bands, while it does not appear for TE modes. Simulations suggest that the fields associated with the lowest TM band are strongly concentrated in the dielectric rods. Conversely, the field patterns of the second TM band are characterised by a nodal plane which cuts through the columns (see figure 14). So some of the electrical displacement field amplitude is expelled from the region with high refractive index, creating a large energy difference between the two modes. In fact, by a variational principle (see [15], Chapter 2), a mode concentrates most of its electric-field amplitude in the regions with high refractive index to have a lower frequency, as the fields of the first TM band do. Anyway the upper TM band must be orthogonal to the lower one, having a nodal plane. This means a larger part of its electric-field amplitude lies in the air region, so that its frequency is significantly higher than that of the previous mode. This strong difference of the fields' confinement in the columns explains the appearence of the TM band gap. In the case of TE radiation, the concentration of the modes does not contrast so strongly, meaning that the photonic bands are not separated by any gaps.
This phenomenon is caused by the discontinuous boundary conditions for the electromagnetic field at material interfaces. If we move across a boundary from a high ε_1 to a lower $\varepsilon_2 < \varepsilon_1$, the energy density $\sim \varepsilon|\mathbf{E}|^2$ will change discontinuously:

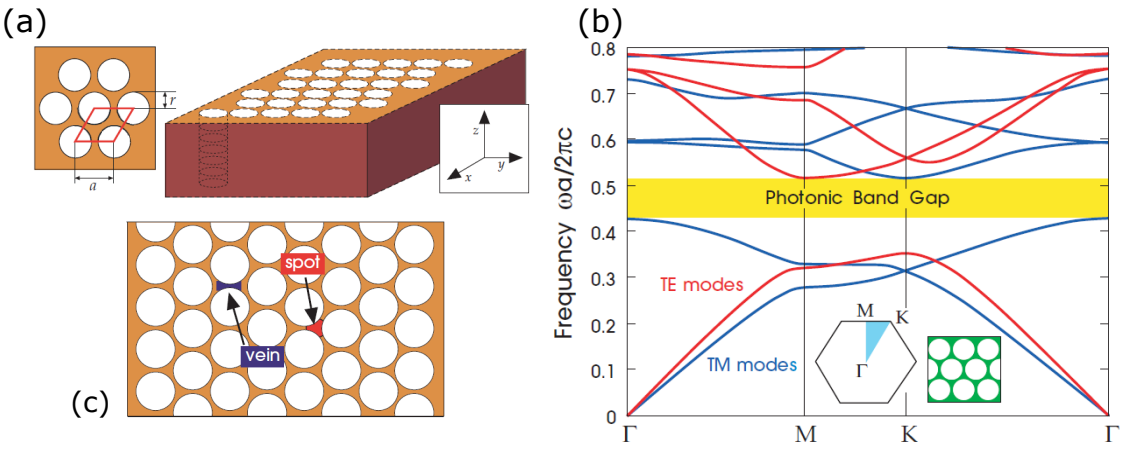

Figure 15: A triangular array of air columns ($\varepsilon = 1$) is immersed in a material with high $\varepsilon = 13$. The left inset shows the unit cell framed in red (a). It has radius r and lattice costant a. For $FF = 0.48$, the band structure possesses a complete band gap for both TE (red) and TM (blue) modes, as seen in (b). The calculations are made in the irreducible BZ highlighted in blue in the inset of (b). Figure (c) shows the formation of spots between three near columns connected by narrow dielectric veins. [15]

- if **E** is parallel to the interface (as in the TM case), then $\mathbf{E}_{||}$ is the same on both sides and the energy will decrease by a factor $\varepsilon_2/\varepsilon_1$. This allows a strict confinement of the electric field in the isolated rods.

- if **E** is perpendicular to the interface (as for TE modes), the continuity of $\varepsilon\mathbf{E}$ makes the energy increase by a factor $\varepsilon_1/\varepsilon_2$. So the TE modes are forced to cross the boundary at some point, letting the electrical energy out of the regions with high index of refraction and preventing a strong confinement.

Instead, the situation is reversed in a connected 2D structure, for example a square grid of dielectric veins with high ε. In this case, the presence of a connected path with high refractive index avoids the leakage of the TE modes in the outer region. The resulting higher concentration of such modes easily induces a photonic band gap for TE modes, while the TM radiation is not well confined in the veins and thus the band gap formation is not favored in such systems.
If these opposite requirements are well balanced, it also possible to engineer a photonic crystal with a complete band gap, i.e. having a good overlap between the TE and TM prohibited frequency intervals. An example is the triangular lattice of air columns with radius r and lattice parameter a, immersed in a high-ε medium illustrated in 15. When the filling factor $FF = r/a$ is high enough, the spaces between three near columns form distinct spots with high refractive index, where the TM modes are well confined. The narrow material veins between two columns instead guarantees the connectivity needed for the TE modes, which are well concentrated too. All this discussion holds in the limit $k_z << |\mathbf{k}_{||}|$, which is the typical case of a QCL active region where the electric field is parallel to the growth axis $\hat{\mathbf{z}}$ and propagation takes place in the perpendicular plane.

2.3.4 Light amplification and extraction in photonic crystals

In a resonator, the existing modes slowly decay due to absorption and losses. They act like fields having a complex frequency $\nu_c = (\omega_0 - i\delta)/2\pi$, so they oscillate while exponentially decaying: $\mathbf{E}(t) \propto e^{i\omega_0 t}e^{-\delta t}$. The energy associated with the mode decays

even faster, according to the relation $\sim e^{-2\delta t}$. The overall loss rate can be described by a dimensionless quantity called quality factor:

$$Q \equiv \frac{\omega_0}{2\delta} \tag{121}$$

It can be shown that Q^{-1} represents a dimensionless decay rate:

$$\frac{1}{Q} = \frac{P}{\omega_0 U} \tag{122}$$

where P is the outgoing power and U is the electromagnetic energy localised in the resonator. In the case of our interest, two decay mechanisms are dominant: the losses due to the patterned waveguide/photonic structure (Q_w) and the extraction of light from the device, which gives the radiative term Q_r. The overall quality factor is:

$$\frac{1}{Q} = \frac{1}{Q_w} + \frac{1}{Q_r} \tag{123}$$

In photonic crystals featuring a band gap, the modes near the band edge typically show the highest quality factors. In an active region, modes characterised by a high quality factor are more likely to start lasing, since their long lifetime in the gain medium allows a stronger amplification. Focusing on the specific case of two-dimensional devices with vertical emission, light amplification and extraction feature some important properties:

- the slope of the photonic band can be interpreted as the group velocity $\mathbf{v}_g = \nabla_{\mathbf{k}}\omega_n(\mathbf{k})$ at which the mode energy propagates. For fields with $|\mathbf{v}_g| \approx 0$, behaving like standing waves, the interaction time with the material is increased, enhancing the gain in distributed feedback laser;
- the photonic crystal allows two or more fields to diffract with each other, possibly producing a mode with zero in-plane $\mathbf{k}_{||}$. In the reciprocal lattice, the only wavevectors whose sum can give $\mathbf{k}_{||} = 0$ are those which lie at the high-symmetry points of the first Brillouin zone. When the in-plane component disappears, radiation can be vertically extracted from the device.

A further analysis of this characteristics, with a collection of representative geometries, can be found in [17].

2.4 PHOTONIC QUASICRYSTALS

2.4.1 Fundamental definitions and properties of quasicrystals

A photonic quasicrystal (PQC) is a structure whose refractive index $n(\mathbf{r})$ is not periodic in space, yet it is modulated by a deterministic rule. Such geometries gained an increasing attention in physics since the 80's, after the unexpected discovery of some Al-Mn alloys, whose atoms are arranged in a quasicrystalline scheme [18]. In fact, the samples exhibited a surprising electron diffraction pattern, charaterised by symmetries which are strictly forbidden for crystals. This was the first reported case of a new material phase, different from both the well known crystals and amorphous solids. Since then, the discovery has had a deep impact, far beyond crystallography. In photonics, the use of these irregular patterns was proposed, starting a new and intriguing field of reasearch.
An ideal quasicrystal is built by the infinite repetition of two or more distinct structural units, named "unit cells", that are packed in a lattice with long-range quasiperiodic

translational order and long-range rotational order. The different unit cells are motifs which are not repeated periodically and yet fill the whole space. In two dimensions, the unit cells are called tiles and can form a full tessellation of the plane, leaving no empty space ("frustration"). The quasicrystals have the following formal properties [19].

- Orientational order:
  the bond angles between neighboring atoms (measured with respect to a a fixed set of axes) are oriented, on the average, along a set of "star" axes, defining the orientational order. In general, the set of star axes can be chosen arbitrarly.

- Minimal separation between atomic sites:
  there exist distances $r > 0$ and $R > r$ such that any two nearest-neighbor sites have a separation $d \in [r, R]$. This distinguishes quasicrystals from a set of sites given by the superposition of two crystals, whose periodicities have an irrational ratio. In the latter case, the distance d can be arbitrarly small. Minimal separation is also a necessary condition to have a finite number of fundamental unit cells.

- Quasiperiodic translational order:
  the mass density function of a quasicrystal is quasiperiodic. A quasiperiodic function can be written as the sum of periodic terms, where at least some of the periods are in incommensurate ratios. For example, the function $f(x) = cos(x) + cos(\pi x)$ is quasiperiodic.

These geometries do not have any trivial translational invariances, and often are self-similar, i.e. their global structure is similar to a part of itself. Anyway this property is not present if the star vectors do not have a high degree of orientational symmetry. An important feature of quasicrystals is their diffraction pattern, which strongly depends on their structure factor $S(\mathbf{k})$, that is, the Fourier transform of the geometrical structure in real space (see [2]). It contains a summation over all the N sites $\mathbf{R}_i$, so that one can write

$$S(\mathbf{k}) = \lim_{N\to\infty} \frac{1}{N} \sum_i e^{i\mathbf{k}\cdot\mathbf{R}_i} \tag{124}$$

for an infinite quasilattice. In the case of a periodic crystal, the Fourier components identify well defined reciprocal vectors $\mathbf{k}$ thanks to the Bragg peaks of $S(\mathbf{k})$, as seen at the end of Chapter 1. A quasicrystal has a much richer spectrum, ideally dense or singular continuous, i.e. for every two maxima of $S(\mathbf{k})$ there is always a third peak in-between. The fact that the quasicrystal's structure factor has discrete Fourier components is a typical sign of long-range order and gives information about the symmetries of the structure.
The large variety of complex quasicrystal patterns can be produced with many different methods. Among them, the most famous techniques are:

- matching and inflation rules;

- strip and cut projections from higher-dimensional periodic crystals ("hyper-crystal");

- the generalized dual method (GDM), which will be introduced in detail and used to construct the pattern of our quasiperiodic photonic structures.

The photonic applications of these structures are implemented by placing dielectric scatterers in the sites of the quasilattice, as seen with photonic crystals. The huge difference is the presence of deviations from periodicity in the PQCs. This means that all the solving tools based on the Bloch theorem cannot be applied. In particular, the restriction of the problem to the small irreducible Brillouin zone is impossible, and the

n	Fibonacci string	ν_n^A	ν_n^B
0	A	1	0
1	AB	1	1
2	ABA	2	1
3	$ABAAB$	3	2
4	$ABAABABA$	5	3
5	$ABAABABAABAAB$	8	5
⋮	⋮	⋮	⋮
n		F_{n+1}	F_n

Table 2: The first elements of the Fibonacci chain are shown. ν_n^A and ν_n^A count the occurrence of the elements A and B at the n-th step. Their values correspond to the numbers the Fibonacci sequence $F_n = F_{n-1} + F_{n-2}$, with initial value $F_0 = 0$ and $F_1 = 1$.

diagonalization of the operator $\hat{\Theta}(\mathbf{r})$ of eq. 105 must be performed on the whole system. Even if the presence of some symmetries can diminish the computational effort, usually the eigenmode analysis is much more demanding than in the photonic crystal case.

2.4.2 A one-dimensional photonic quasicrystal

A simple case of quasicrystal in one dimension is based on the famous Fibonacci chain. Let us consider two basic segments A with length L_A and B with length L_B, and impose the inflation rule σ: $A \to AB$ and $B \to A$. The matrix representation the transformation is (see [20]):

$$\sigma : \begin{pmatrix} A \\ B \end{pmatrix} \to \begin{pmatrix} 1 & 1 \\ 1 & 0 \end{pmatrix} \begin{pmatrix} A \\ B \end{pmatrix} = \begin{pmatrix} AB \\ A \end{pmatrix} \tag{125}$$

Starting from element A, the n-th iteration of σ produces a string $w_n = \sigma^n(A)$ or equivalently: $w_{n+2} = w_{n+1}w_n$, as shown in table 2. The occurence of the unit elements ν_n^A, ν_n^B at the n-th step are consecutive numbers of the Fibonacci sequence, so that their limit is:

$$\lim_{n\to\infty} \frac{\nu_n^A}{\nu_n^B} = \lim_{n\to\infty} \frac{F_{n+1}}{F_n} = \phi = \frac{1+\sqrt{5}}{2} \approx 1.618 \tag{126}$$

where ϕ is the golden mean. Let us consider the special case when the ratio $L_A/L_B = \phi$, which ensures self-similarity. The Fibonacci structure factor consists in a set of discrete Fourier components, which may induce intense Bragg peaks in $S(\mathbf{k})$. For an infinite chain, it can be demonstrated that the peaks occur at the wavevectors (see figure 16.b):

$$Q_{hh'} = \frac{2\pi}{L_B} \frac{\phi^2}{\phi^2+1} \left(h + h'/\phi\right) \tag{127}$$

where h, h' are independent integers. The Fourier components associated with such reciprocal vectors can be calculated, showing large values when the integers correspond to consecutive Fibonacci numbers.

A Fibonacci photonic quasicrystal is constructed from two types of dielectric layers with permittivity ε_A, ε_B and thickness L_A, L_B, as in figure 16.a. In this system, the structure factor is given by the Fourier components ε_{k_z} of the dielectric function, which varies along the $\hat{\mathbf{z}}$ direction, perpendicular to the slabs: $\varepsilon(z) = \sum_{k_z} \varepsilon_{k_z} e^{ik_z z}$ with $k_z = Q_{hh'}$. As

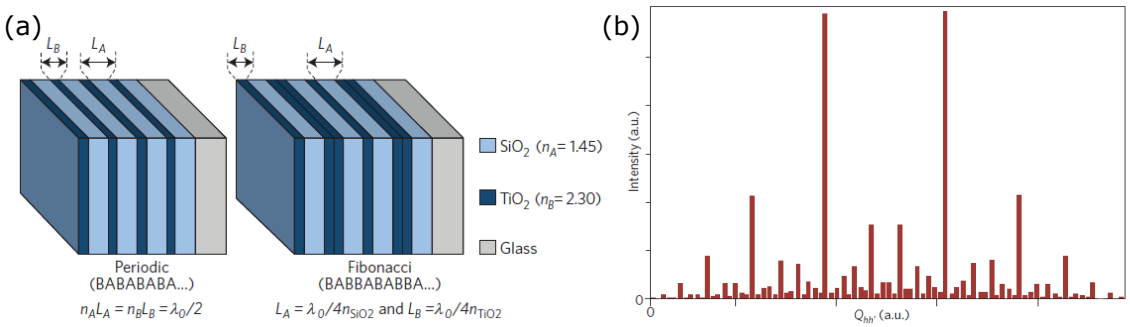

Figure 16: Comparison between two multilayer structures, in which SiO_2 (A) and TiO_2 (B) slabs are arranged in a periodic fashion (a, left) or according to the Fibonacci scheme (a, right). Since the layers are built with $n_A L_A = n_B L_B$ and the refractive index are in golden ratio $n_B/n_A \approx \phi$, this results in $L_A/L_B \approx \phi$. The structure factor of a 1D Fibonacci quasicrystal (after 987 inflation steps) is plotted as a function of $Q_{hh'}$ (b). [21]

reported in [2], light propagation in this multilayered system is described by the equation for the electric field:

$$\left(-\frac{d^2}{dz^2} - q^2\right) E(z) = q^2 \sum_{k_z} \frac{\varepsilon_{k_z}}{\varepsilon} e^{ik_z z} E(z) \tag{128}$$

where the average dielectric constant is $\varepsilon = (\varepsilon_A N_A L_A + \varepsilon_B N_B L_B)/(N_A L_A + N_B L_B)$ and $q = \omega c/\sqrt{\varepsilon}$. A numerical solution indicates that the reflectivity and transmission spectra show prohibited intervals, or pseudo gaps, around the critical frequencies $\omega_{hh'} = cQ_{hh'}/2\sqrt{\varepsilon}$. These correspond to fields with wavevectors $\mathbf{k} = (\pm Q_{hh'}/2)\hat{\mathbf{z}}$.
Recently, lasing was demonstrated in a Hz QCL based on the distributed feedback provided by a 1D Fibonacci quasicrystal (see [22]). The Fibonacci sequence was mapped to a metallic grating by replacing every interface between A and B by a slit in the top metallization of the device. This produced vertical emission at a precise angle, determined by the parameters of the structure. The mode with largest quality factor was obtained near the edge of the gap, with a wavevector $|\mathbf{k}| = Q_{11}/2$, which is analogous to the behaviour of periodic structures introduced in section 2.3.4. Using an active region with a broad gain bandwidth allowed observing emission at different wavelengths.

2.4.3 Two-dimensional photonic quasicrystals

In the case of two-dimensional geometries, a typical solution is the use of dielectric rods at the vertices of the quasilattice, embedded in a material with high contrast of refractive index. As seen in periodic structures, the size and distribution of the scatterers and their indices n influence the local concentration of TM- and TE-polarized electromagnetic fields. In turn, this affects both the quality factor Q and the outcoupling of the modes to free space. It is important to characterise the geometrical properties of the PQC, defining a quasilattice constant a. If the quasicrystal consists of N sites enclosed in a surface area A, one can write

$$a \equiv \sqrt{\frac{A}{N}} \tag{129}$$

which gives a characteristic scale of length of the system. Thus it is possible to introduce a filling factor even for such 2D aperiodic structures: $FF = r/a$.
Let us consider the case of a connected photonic quasicrystal, an array of low refractive

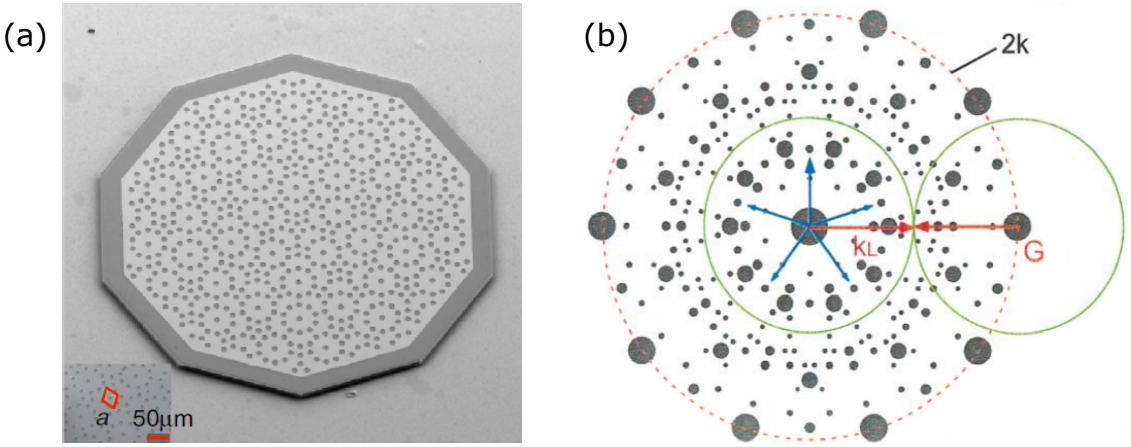

Figure 17: A Scanning Electron Microscope (SEM) image of a Terahertz photonic resonator based on a 5-fold Penrose quasicrystal (a), showing the air holes imprinted on the top metallization in the inset [23]. A graphical scheme of the feedback mechanism in a 5-fold Penrose quasicrystal (b) highlights the interaction between the photonic wavevector $\mathbf{k}_L$ and the reciprocal vectors $\mathbf{G}$ of the quasicrystal, corresponding to the Bragg peaks of the structure factor. The diameter of the dark spots is proportional to the intensity of the associated Fourier component [24].

index (n_1) pillars, immersed in a material with higher index $n_2 > n_1$. This is the typical configuration of a PQC patterned in a THz QCL active region, by opening air holes on the upper part of the system (figure 17.a). Numerical studies indicate that the opening of an interval of prohibited frequencies for TM modes is possible only for $FF > 40\%$. This means that an extended portion of the active region should be removed to produce high-Q modes around the gap. Unfortunately, the resulting increase in waveguide losses and the worse mode confinement in the semiconductor heterostructure would be detrimental for light amplification. As a consequence, milder values of FF (usually, $FF = 0.25 \div 0.35$) are used [23].
However, lasing can be still achieved if the quasicrystal feedback mechanism is designed to enhance the gain for some modes. The process can be analysed in terms of the reciprocal vectors and the structure factor: when a wave is produced, it will undergo multiple scattering by the lattice, so that it can be expressed as a combination of plane waves diffracted by all the reciprocal lattice points [24]. It can be shown that standing waves form if

$$\sum_j (\mathbf{k}_P - \mathbf{G}_j) = 0 \tag{130}$$

where $\mathbf{k}_P$ is the optical mode wavevector and $\mathbf{G}_j$ are all the reciprocal vectors identified by the Bragg peaks in the structure factor. As in periodic crystals, standing waves strongly interact with the gain medium, so that their amplification is very efficient. We will now refer to the representative example of a 5-fold Penrose quasicrystal. The Bragg peaks responsible for the feedback can be found by the intrsections of the circumferences with radius $m|\mathbf{k}_P|$ with the reciprocal vectors (figure 17.b). The vector $m\mathbf{k}_P$ satisfies the condition 130 for a small finite number of diffraction. For example, the simplest two-wave ($m = 2$) interaction case is $\mathbf{k}_P - \mathbf{G}_j = -\mathbf{k}_P$ for a given reciprocal vector $\mathbf{G}_j$.
In [23], THZ emission in the vertical direction from a QCL having a patterned Penrose PQC on the top surface was reported. Using the explained method, the main radiating mode is attributed to a complex five wave diffractions, characterised by $m = (1 + \sqrt{5})/2$, while simpler wavevector interactions are absent. The emission spectrum also showed a

relevant dependence on the filling factor FF. This type of device represents an important reference with respect to the present work, whose aim is the development of new two-dimensional THz resonators.

2.5 RANDOM LASERS

2.5.1 Light in random materials

Although the diffusion of light by random materials is a well-known phenomenon in every day life, the behaviour of photons in such disordered systems presents a lot of interesting aspects. In fact, light is multiply scattered in an elastic way, so no optical information is lost. Due to reciprocity, the process is, in principle, fully reversible, even if in real life it is still impossible to look through a marble wall, for example. As pointed out in [25], this happens because the interference between several randomly scattered waves produces a complex intensity pattern, often referred to as a "speckle-pattern". So the information about the shape of an object behind a wall is still present, but it is scrambled and thus unrecognizable.
The fundamental concept of reciprocity is also at the heart of the phenomenon named "coherent backscattering" or "weak localization". Let us consider a light pulse from a broadband source, impinging on a cube of material with a random structure. If a detector collects the light in the backscattered radiation, there will be a huge number of optical paths from the source to the detector, each following random trajectories inside the object and then being expelled back. Each trajectory can be followed back and forth, so two counter-propagating waves exist and interfere constructively in the backscattering direction. Moving away from this direction, the effect of the accumulated phase difference gradually makes disappear the interference. This results into a cone of light intensity, whose width measures the scattering strength of the material.
This regime is often seen as a precursor of the so-called "strong localization" or "Anderson localization", by analogy with the famous electron transport effect in solid state physics, where disorder can completely stop electrical conduction. In the photonic strong localization, a highly disordered medium can trap light, producing modes with a high spatial confinement for a long time. If the counter-propagating waves seen in the backscattering are costrained to follow closed loops in the random material, there would be a standing wave mode with a random intensity profile. This confinement of light is more likely to happen in one- or two-dimensional systems. In fact, the odds of coming back to the same region of a 1D or 2D material and form a closed path, are higher than in a three-dimensional structure.
A random photonic structure is characterised by a random spatial profile of the dielectric function $\varepsilon(\mathbf{r})$. Its spatial variation can be characterised statistically by the correlator [26]

$$K(\Delta\mathbf{r}) \equiv \langle \varepsilon(\mathbf{r})\varepsilon(\mathbf{r}+\Delta\mathbf{r}) \rangle \tag{131}$$

where $\langle \ldots \rangle$ is the ensemble average. When the random medium is isotropic, the width of $K(\Delta\mathbf{r})$ defines a correlation radius R_c. It represents the typical scale of spatial fluctuation of the dielectric constant, which can be compared to the light wavelength λ. When $R_c >> \lambda$, light propagation is governed by long-range disorder, while for $R_c \leq \lambda$, short-range disorder has a dominant effect. In order to characterise the behaviour of light in random structures, some important length scales are introduced.

- Scattering mean free path l_s: it indicates the average distance between two consecutive scattering events.

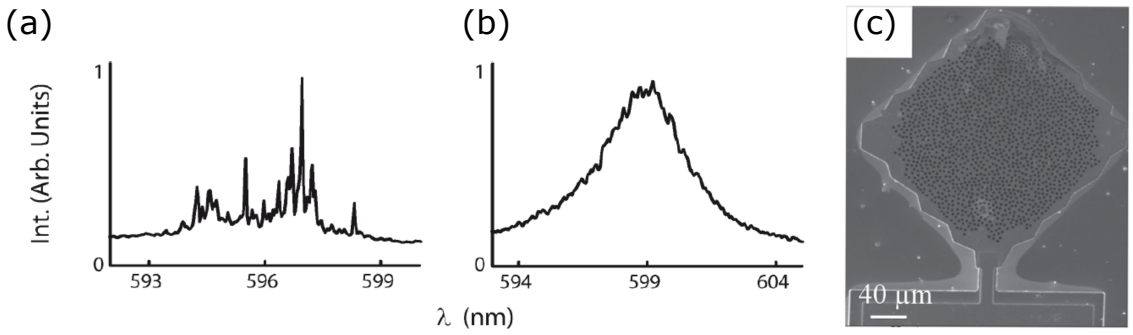

Figure 18: Examples of spectra in the RFRL (a) and IFRL (b) regimes for a random laser in the region of visible light, measured in [27]. The mid-IR quantum cascade laser patterned with a two-dimensional random photonic structure [28] is shown in (c).

- Transport mean free path l_t: it is defined as the average distance before the direction of light propagation is randomized. The two quantities are related via the equation:

$$l_t = \frac{l_s}{1 - \langle \cos\theta \rangle}$$

  whre θ is the scattering angle.

The appearence of Anderson localization is possible only in the strong scattering limit, in which severe interference can halt light in the material. The Ioffe-Regel criterion then states that Anderson localization can take place if

$$l_s < \frac{\lambda}{2\pi} \iff |\mathbf{k}| l_s < 1 \tag{132}$$

for a mode of wavelength $\lambda = 2\pi/|\mathbf{k}|$. Instead, when the typical linear size of the random medium is $L \approx l_t$, the interaction between the light and the material is negligible. So photons are unperturbed and propagate in a ballistic regime.

2.5.2 Laser action in random photonic structures

The electromagnetic modes that can exist in a random photonic structure do fulfill the general eigenvalue equation 105. Similarly to quasicrystals, the absence of a regular profile of the refractive index makes the computation quite difficult. The allowed eigenmodes that hardly couple to the environment, having nonzero amplitude in a small region of the resonator, so they are named "closed" or "localised" modes. Instead, the modes that couple to the environment, extending over the whole structure, are called "open". A random laser is an active region combined with a disordered pattern of scatterers, so that gain can be achieved for open or closed modes. Usually, the coherent emission of a random laser is broader than that of more regular photonic resonators and has a complex spatial profile, determined by the speckle of scattered light.
The role of the spatial distribution of the fields inside the random medium is still under debate. Coherent emission can be indeed determined by localised as well as by open modes. However, the greater spatial overlap of extended fields triggers a higher mode competition in achieving gain. As reported in [27], two different lasing regimes are possible in a random laser:

- the "incoherent feedback random lasing" (IFRL) was the first observed lasing emission from a completely disordered material. It is characterised by a smooth,

single-peak spectrum (figure 18.a) and can be explained by the diffusion approximation, treating light rays as the trajectories of random walking particles. In this case, many spatially overlapping modes are activated and cluster around a central frequency. This can, in principle, also trigger a spontaneous mode-locking, with many close frequencies with a regular spacing.

- the "resonant feedback random lasing" (RFRL) features few sharp, uncorrelated peaks (figure 18.b) in the emission spectrum, due to distinct localised modes with low interaction and high quality factors;

Both physical regimes were recently unveiled in the mid-infrared region [28], using a 2D random resonator made up by air holes imprinted on the top surface of a QCL heterostructure, as shown in 18.c. The filling factor FF controls the intensity of the scattering of TM electromagnetic fields in the system. When the scattering is weak (low $FF < 20\%$), the resonant feedback is active and emission on well separated wavelengths is measured. Instead for higher FFs, the IRFL regime is produced, with an evident clustering of peaks around a central frequency.
Being random behaviour quite difficult to be "engineered" at longer wavelengths, the investigation of random patterns and their possible exploration for THz QCL "random emission" is a very demanding but highly intriguing goal.

3 METHODS

As seen in the previous chapter, aperiodic photonic structures are characterised by a rich variety of physical phenomena, which can be used to improve the optical and electrical performance of a laser. In particular, we will investigate the use of quasi-crystal and random resonators for the generation of THz emission in a QCL heterostructure, with high efficiency and multimode operation on a wide gain bandwidth. The designed QCL devices were fabricated and characterized, following the methods illustrated in the next sections.

3.1 MODELLING

3.1.1 Generation algorithm and physical parameters of quasicrystals

In order to define the geometry of the quasicrystal pattern, we used the generalised dual method (GDM) illustrated in reference [29]. This powerful method can be used to generate all the structures obtained by the other techniques, but it is also capable of constructing a much wider class of of patterns, for any orientational symmetry. The resulting new geometries are quasiperiodic and orientationally ordered, though they are not self-similar in general. The main advantage is that the orientational symmetry can be chosen in an arbitrary way, so that many different patterns can be produced with one procedure. Working in two dimensions, the GDM consists of the following steps, which were implemented in a MATLAB code to have computer-generated quasicrystals.

1. A set (or "star") of $\mathcal{N}$ two-dimensional vectors is chosen: $\{\mathbf{v}_0, \ldots, \mathbf{v}_{\mathcal{N}-1}\}$ to determine the orientational symmetry. To have a $\mathcal{N}$-fold rotational symmetry, we can for example chose the vectors:
$$\mathbf{v}_n = \cos(2\pi n/\mathcal{N})\,\hat{\mathbf{x}} + \sin(2\pi n/\mathcal{N})\,\hat{\mathbf{y}} \tag{133}$$
for $n = 0, \ldots, \mathcal{N}-1$ which are oriented at angles $\phi_n = 2\pi n/\mathcal{N}$.

2. For each $\mathbf{v}_n$, we consider an infinite set of perpendicular straight lines ("grid") in a cartesian coordinate system, with a periodic or quasiperiodic spacing. Thus a total of $\mathcal{N}$ line sets is needed, and their collection is called $\mathcal{N}$-grid. Due to the finite computational resources, we are forced to consider a limited number R of lines per grid. All the lines in the n-th grid are progressively labeled by an integer $r_n = 0, \ldots, R-1$, representing their ordinal position along $\mathbf{v}_n$. There are many degrees of freedom in the prescription for a $\mathcal{N}$-grid, such as the length scale and the separation between consecutive lines. We chose to set the separation between the lines of a grid with slope $\tan\phi_n$ by fixing a number of regularly spaced points $\mathbf{P}_r^{(n)}$, each of them belonging to the line r_n of the n-th grid. Every $\mathbf{P}_r^{(n)}$ has the following coordinates:
$$\begin{cases} y(r_n) = \alpha n \sin\phi_n - \left(r_n - \left\lfloor \dfrac{R}{2} \right\rfloor\right)\cos\phi_n \\ x(r_n) = \beta n \cos\phi_n + \left(r_n - \left\lfloor \dfrac{R}{2} \right\rfloor\right)\sin\phi_n \end{cases} \tag{134}$$

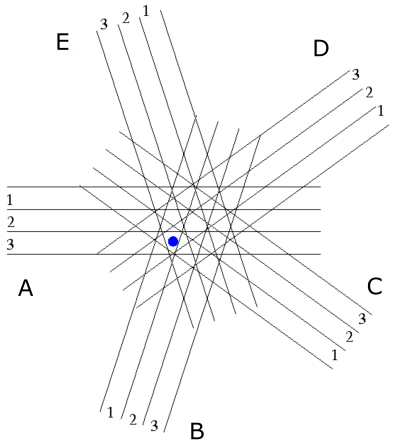

Figure 19: In the case of a star of $\mathcal{N} = 5$ initial vectors, the five grids (A, B, C, D, E) of parallel lines are shown. In every grid, lines are labeled progressively by their position. The spot indicates a point $\mathbf{Q}$ in a polygon formed by the intersections of the grids.

that determine a periodic separation between the parallel lines of grid. $\lfloor\rfloor$ is the floor function. As we will see, the parameters α and β are introduced to produce different quasicrystal patterns.

3. The intersection between lines divides the plane into polygons, which can be arbitrarily small. Consider a point $\mathbf{Q}$ located inside one of these polygons (see figure 19): with respect to a single grid, the point lies within a strip between two lines, say r_n and $r_n + 1$ in our notation. This holds for all $\mathcal{N}$ grids, so the polygon is uniquely specified by $\mathcal{N}$ integer indices $(r_0, \ldots, r_{\mathcal{N}-1})$.

4. Every polygon is mapped to a two-dimensional plane, the so-called cell space, by the transformation

$$\mathbf{t} = \sum_{i=0}^{\mathcal{N}-1} r_i \mathbf{v}_i \tag{135}$$

which gives a vertex of a quasicrystal. By iterating the procedure over all the closed regions, a finite subset of points of an ideal quasicrystal can be generated.

Let us consider an intersection point between two straight lines in figure 19. It is surrounded by four polygons having very similar sets of indices $(r_0, \ldots, r_{\mathcal{N}-1})$, because they are neighboours. Then there are four near quasicrystal sites, which correspond to the vertices of a tile of the aperiodic systems. It should be noted that the more R lines per grid are considered, the more intersections will appear. This means that large quasicrystal regions are obtained for rather high R. In this work, 50 lines per grid proved a good choice, so that thousands of vertices could be computed in a reasonable time.
The parameters α, β allow us to control the degree of disorder of the whole structure. In fact, they affect the y-intercept of the straight lines which contains a term $\sim (\alpha - \beta)n$. When $\alpha = \beta = 0$, this dependence disappears and all the grids are perfectly invariant under a rotation of angle ϕ_n around the origin. This gives a high degree of symmetry to the resulting quasicrystal. If $\alpha - \beta \neq 0$, due to a change in the relative positions of the grids, more disordered patterns are generated. In particular, some points are removed from the regular distribution and displaced at new coordinates, introducing point defects. In our case, we decided to analyse geometries with a 7-fold rotational symmetry, based on the characteristic angle $2\pi/7$ ($\approx 51.4°$). Such systems possess a more complex structure than the already existing 5-fold Penrose THz resonators, which were conversely targeting

the goal of a single-mode, high-Q emission. In order to explore the interplay between the 7-fold symmetry and the point defects, we generated highly symmetric ($\alpha = \beta = 0$) and lowly symmetric ($\alpha = 1, \beta = 0$) quasicrystals. We will also refer to such geometries as "type-A" and "type-B" from here on. The two-dimensional discrete Fourier transform of the quasilattices was also performed, so that the underlying symmetries could be revealed (see figure 20).
In order to translate the mathematical quasilattice into a two-dimensional photonic resonator, we restrict to a circular region containing $N \approx 500 \div 600$ points. The whole region is then rescaled to set the value of the surface area A and thus the quasilattice parameter $a = \sqrt{A/N}$. The two values used for the area are: $A = 0.53mm^2$ and $A = 0.64mm^2$.
The dielectric scatterers are drawn by superimposing circles of radius r on the quasicrystal vertices. This last choice specifies the system's filling factor $FF = r/a$, which strongly affects the behaviour of light in the system. So resontators with different size are studied, varying the scatterers' radius r. The typical values are $FF = 19\% \div 30\%$, which are quite similar to those used in the Penrose THz resonator [23].

3.1.2 Random patterns

Two-dimensional random patterns are generated using the rand() function of MATLAB. It extracts a pair of pseudo-random coordinates (x, y) from a uniform distribution of probability in the finite square domain $[-L/2, L/2] \times [-L/2, L/2]$. L is the desired length of the side in μm, set to $L = 670\mu m$ and $L = 770\mu m$ corresponding to surface areas $A = 0.45mm^2$ and $A = 0.59mm^2$ respectively.
The only added costraint is a minimum distance of $20\mu m$ between pseudo-random points. This prevents any overlaps between the circles representing the dielectric scatterers, having a diameter $2r < 20\mu m$. As seen with our quasicrystals, the circles are placed at the drawn random coordinates. In this work, two different patterns were produced with $N = 395$ and $N = 580$ points and the scatterer radius was varied to explore the interval $FF = 16\% \div 23\%$ and $FF = 24\% \div 32\%$ respectively. We will name the tested random patterns as "type-C" geometries.
Thanks to the DXFLib library for MATLAB, the selected geometries could be transformed into CAD files, to be imported in the simulation software and used to produce an optical lithography mask, as illustrated in the next sections.

3.1.3 Effective index approximation

The devices that were studied and fabricated consist of a $10\mu m$-thick THz QCL active region, which is sandwiched between two Au layers forming a double metal waveguide. Voltage is applied between these two highly conductive layers, inducing the electronic band alignment required for device operation. The top metallization is patterned by air holes to produce vertical emission from the quasicrystal and random patterns seen before.
To understand which Terahertz modes are favored in such disordered two-dimensional photonic structures, we need to calculate their quality factor Q. As seen, high-Q modes decay slowly in time, so that they can be strongly amplified in the gain medium and produce laser action.
The evaluation of the quality factors requires the numerical solution of the eigenvalue problem 105 in the whole volume of the resonator, but it would be an extremely difficult and time-consuming task. A well-known technique to simplify the computation is the effective index approximation (EIA). This approach replaces the actual three-dimensional

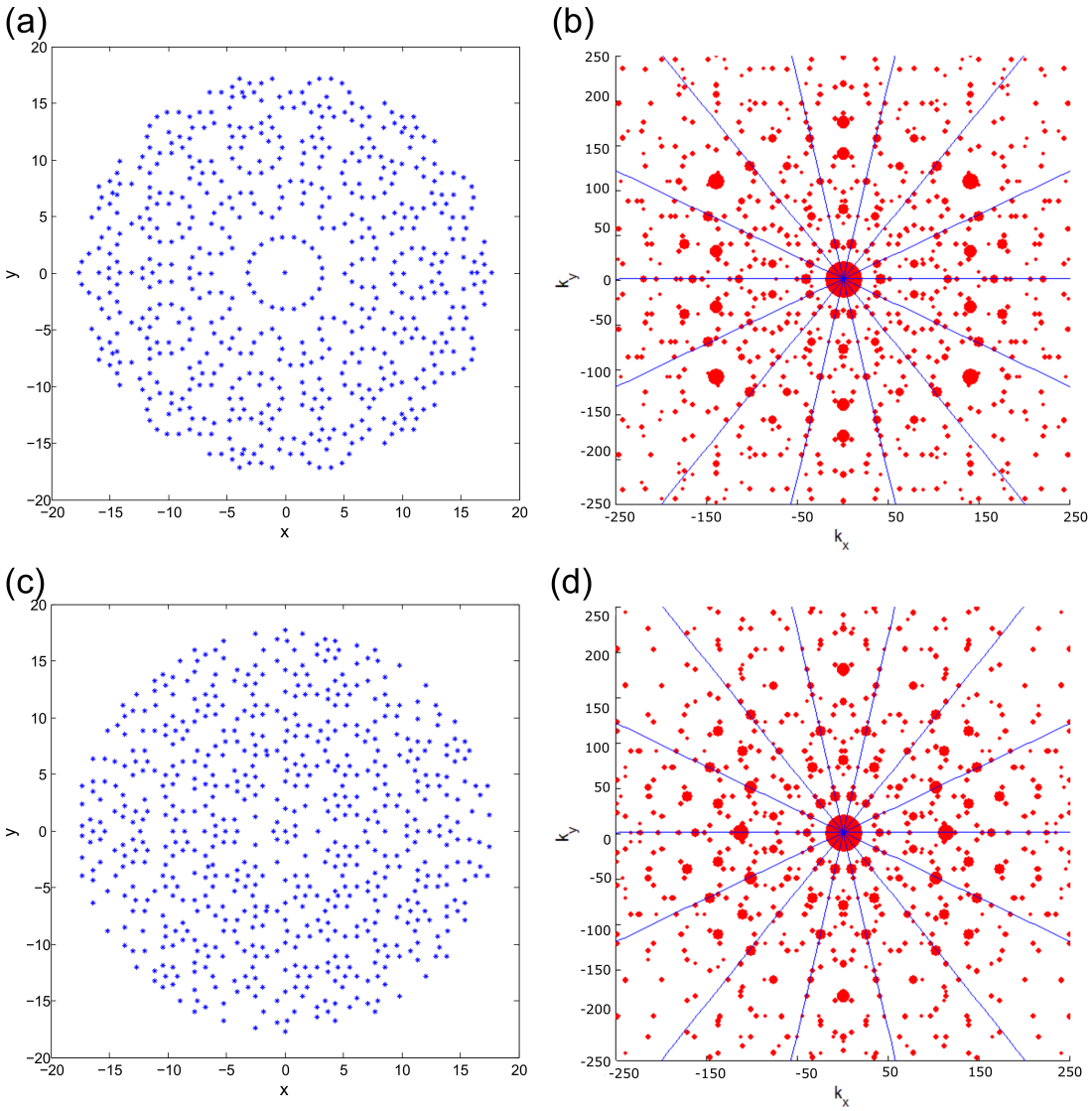

Figure 20: The geometrical points forming the highly symmetric (a) and lowly symmetric (c) 7-fold quasicrystals are generated using 50 lines per grid, setting $\alpha = \beta = 0$ (type-A) and $\alpha = 1, \beta = 0$ (type-B) respectively. Their discrete Fourier transforms are in (b) and (d) respectively, with the size of the red spots proportional to the amplitude of the Fourier coefficients. The blue lines have a slope $\tan(2\pi n/7)$, with $n = 0, 1, \ldots, 6$. The reported (x, y) and (k_x, k_y) coordinates are in dimensionless units.

structure by an effective, two-dimensional refractive index profile, neglecting the device thickness along the growth axis $\hat{\mathbf{z}}$ and solving the eigenproblem only in the perpendicular $x-y$ plane. Interesting insights can be found in references [30], [31]. The method is based on the fact that the radiation wavelegth in GaAs is $\lambda_{THz} \approx 30\mu m$ (at $3THz$), which is larger than the thickness of the heterostructure and the the size of the scatterers. This means that:

- in the spectral region of interest (around $3THz$), the heterostructure layers can be treated as one effective layer with a refractive index n_b. The small air holes in the metallization can be seen as columns extending across the whole device, so that a refractive index n_s can be used for them too;
- since THz radiation is TM-polarized ($\mathbf{E} \parallel \hat{\mathbf{z}}$), the electric field varies slowly over the thickness of the active region. In fact, it is nearly constant, apart from a small deflection of the field lines near the air holes. The vertical losses can be taken into account using a value $n_s < n_b$.

Thus, the layers of the active region can be treated as one effective layer with refractive index n_b. The small air holes in the metallization can be seen as columns extending across the whole device, so that a refractive index $n_s < n_b$ can be used to take into account the vertical losses.
The choice of the effective refractive indices is crucial, since high quality factors are generally associated with a large contrast $n_b - n_s$. These parameters can be estimated studying the transverse propagation of THz radiation in a slab of GaAs. A slab with bottom metallization only is a rough model for the semiconductor regions under the air holes in our photonic structures. Instead, if a top gold layer is added to form a double metal waveguide, this configuration is similar to the unpatterned portions of the quasicrystal and random resonators. The simulations indicate that the refractive indices are $n_s = 2.8$ and $n_b = 3.6$ respectively, for the first two modes around $3THz$. These values were also used to predict the modes in the 5-fold two-dimensional THz resonator of [23], showing a good agreement with the experiments.
The limit of this two-dimensional approximation is that it cannot fully reproduce the vertical extraction of radiation, so we cannot evaluate the vertical quality factor Q_r. Anyway, the calculated Q_w describe the in-plane confinement inside the resonator, indicating which eigenmodes are best coupled to the active region for a good amplification.
In our computation tool, we insert a thin border of chromium all around the whole resonator, with the specific purpoe tosuppress unwanted Fabry-Perot or whispering-gallery modes. In fact, Cr is a partially lossy material which can be described with a complex refractive index ($n_c = 3.6 + i$) in the spectral range of interest. In the 7-fold resonators, the Cr border has been designed in the shape of a 14-sided polygon of width $20\mu m$, not to perturb the symmetry of the quasicrystals. Instead, random patterns are enclosed in simple square, whose regularity may somehow introduce undesired elements of order. By analogy with the solution used in [28] for a mid-infrared random laser, we design a highly disordered Cr border with protrusions of the order of λ_{THz} and an average width of $25\mu m$.

3.1.4 Simulations based on the finite elements method

In the field of computational photonics, a lot of numerical methods for partial differential equations are exploited. A widely used approach is based on discretization schemes. This is the case of the variuos finite elements methods (FEM), in which space is divided into a set (or "mesh") of finite geometric elements, i.e. irregular triangles or tetrahedra (see

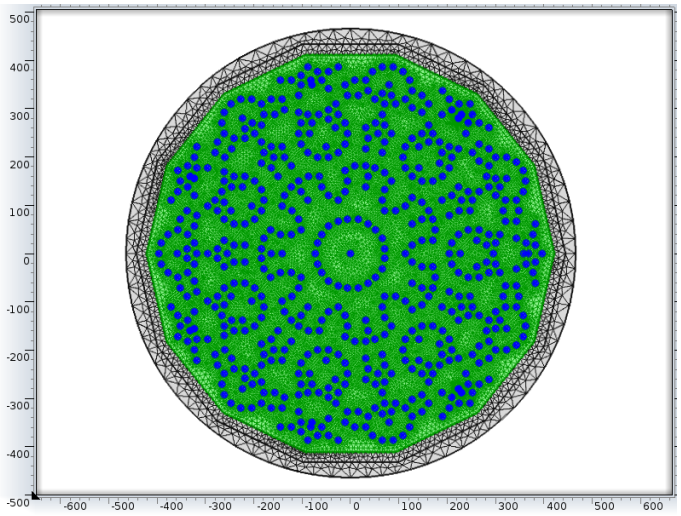

Figure 21: An example of 2D mesh in one representative highly symmetric 7-fold resonator. The green region represents the semiconductor heterostructure (n_b), the blue circles are the air holes (n_s). The external grey area is made up by the Cr borders (n_c) and the surrounding air region.

figure 21). The unknown functions are represented by simple approximations on each element, using low-degree polynomials [15]. This method is at the heart of the simulation software COMSOL Multiphysics, which is used to perform the EIA calculation of the eigenmodes and their quality factors in our photonic structures. The CAD file containing the designed 2D geometries can be directly imported to this software. The effective index approximation can be implemented by assigning the refractive indices n_s, n_b, n_c to the different materials, assuming they are constant over the frequency interval of interest.
Finite elements methods offer the ability to use a variable spatial resolution in different regions, so that complex geometries with very different length scales can be studied. This powerful flexibility comes at the price of computational complexity, so a fine tuning of the mesh parameters is essential to find a tradeoff. COMSOL allows controlling the following parameters:

- maximum and minimum element size:
  the minimum element size is kept between $5 \div 7\mu m \approx \lambda_{THz}/5$ to have a good sampling of the modes around $3THz$. The maximum element size is $60\mu m$, though it is never reached, since no such large homogeneous regions exist in our simulation domains;

- maximum element growth rate:
  when we pass from a zone with rapidly varying structures to a more ordered region, less resolution is needed so the grid elements get bigger. To avoid losing too many details of this transition, we can set a maximum growth factor between neighbouring mesh triangles;

- curvature factor:
  as all shapes are always approximated using segments, this factor limits how big a mesh element can be along a curved boundary. A lower value means a finer mesh. In our case, a critical point is represented by the dielectric scatterers. Since they are already smaller than λ_{THz}, it is enough to mesh each of these circles with a small cluster of triangles forming an octagonal region;

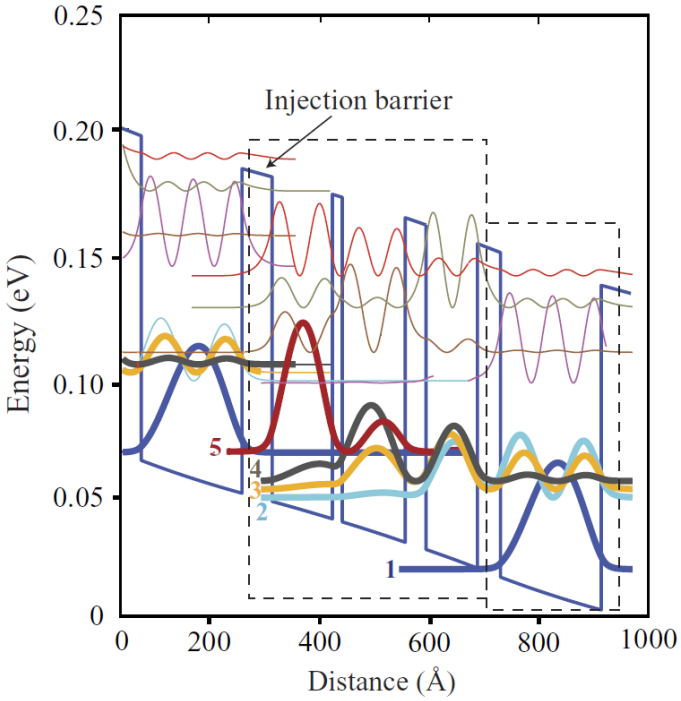

Figure 22: The conduction band diagram of one stage of the structure is reported for an applied electric field $7.6 \cdot 10^6 V/cm$, with the plot of moduli squared of the relevant wavefunctions [32]. The two boxes contain the active stage made up of three quantum wells (on the left) and the extraction region (on the right), respectively.

- resolution of narrow regions:
  when dealing with objects with a scale comparable to minimum element size, this parameter controls locally how fine the grid must be.

Another important point of the simulation setup is the use of the appropriate boundary conditions for the differential problem. In a photonic resonators, light can propagate in the free space, but it is impossible to represent such a realistic configuration with the limited memory of a computer. So a finite surrounding air environment is introduced in the simulation, adding the so-called scattering boundary conditions. Free space is mimicked by a line (in 2D) or a surface (in 3D) enclosing the air region, for which all perpendicularly incident radiation is completely absorbed, without any reflections. When the propagation direction is not orthogonal to the scattering boundaries, the absorption is less efficient. In spite of this problem, scattering boundary conditions are often used because they rarely overload the computer memory.

3.2 FABRICATION TECHNIQUES

3.2.1 Active region

To achieve multimode THz emission over a large spectral range, a bound-to-continumm THz QCL with a single-quantum-well phonon extraction stage, characterized by a wide gain bandwidth ($2.7 \div 3.4 THz$) [32] was selected. The material was grown by molecular beam epitaxy (MBE). The conduction band diagram of a single stage of the heterostructure is shown in figure 22. The layer sequence of one period of the heterostructure is, in nanometers: **5.5**/11.0/**1.8**/11.5/**3.8**/9.4/**4.2**/18.4 from left to right, where $Al_{0.15}Ga_{0.85}As$

barrier layers are in bold, $GaAs$ wells in roman and the underlined number indicates the silicon-doped layer. The donor density is $N_d = 2 \cdot 10^{16} cm^{-3}$. The active stage consists of three quantum wells and is based on a bound-to-continuum transition, while the miniband is coupled to a single extractor quantum well. This is shorter than the typical architecture of five quantum wells and takes advantage of its shorter period to reduce dissipation and improve the maximum operating temperature. The oscillator strength is concentrated mainly on the transition between levels $n = 5$ and $n = 4$ of the active region, whose wavefunctions have little spatial overlap, resulting in an oscillator strength $f \approx 5$.

3.2.2 Fabrication procedure

The nanofabrication procedure for a QCL with a double-metal waveguide configuration and a patterned photonic structures includes the following steps.

1. A layer of gold is deposited on top of the MBE-grown heterostructure and on a substrate of highly doped GaAs ("carrier wafer"). These two structures are then surface-mounted with the gold layers in direct contact, and wafer-bonded with a specific technique called "thermocompression bonding". The two gold surfaces are brought in atomic contact, so that diffusion processes driven by heat and pressure join them in a single crystal. The process temperature is $320°C$, while a pressure of $4.5 MPa$ is applied for 30 minutes.

2. The initial GaAs sample substrate on which the heterostructure was grown by MBE has to be removed, using a combination of mechanical and chemical processes. First, the lapping method is applied, using a fine abrasive powder to leave only a $50 - 100 \mu m$-thick sample substrate. Then, this last part is removed by a chemical etching, via a solution of citric acid and water (1:1), with the addition of 1/3 volume of H_2O_2. The advantage of this chemical method is that it is highly selective, since the reaction ceases when the protective "etch-stop layer" of $Al_{0.5}Ga_{0.5}As$ is reached, without damaging the active region beneath.

3. Finally, the etch-stop layer is removed using a solution of fluoridric acid (HF) with a concentration of 48%. The active region is then directly exposed.

4. Optical lithography is used to define the shape of the absorbing metallic border that surrounds all the designed geometries of type-A,B,C.

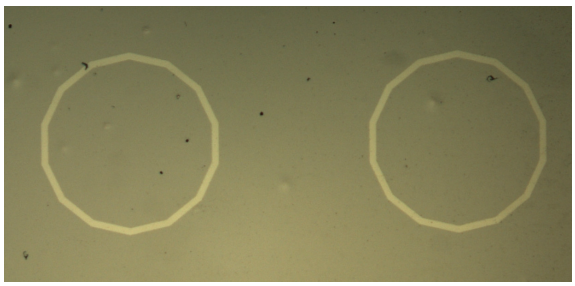

Figure 23: This image, captured at the optical microscope, shows the results of the deposition of $7nm$ of chromium on the sample in the case of a 7-fold resonator.

5. A chromium layer of $7nm$ is deposited on the sample surface in a high-vacuum thermal evaporator (at a pressure of $10^{-6} \div 10^{-5} mbar$). Lift-off procedures were

then followed using acetone to remove the metal from all the sample, apart from the UV-exposed regions which form the absorbing boundary (see figure 23).

6. A successive UV lithography allows reproducing the 7-fold or random geometries, with a careful alignment of the patterns with the outer chromium border.

7. The top metallization of the devices is realized by metal deposition of Cr/Au ($5nm/150nm$). In this case, the presence of chromium is necessary for a good adhesion of the gold layer, whose thickness must be larger than the penetration depth of THz radiation ($\approx 30nm$ typically). This minimizes the losses in the metal layer and helps the confinement of the field.

8. After the Cr/Au deposition, lift-off with acetone is required to remove the gold from the holes of the disordered patterns.

9. The upper contact layer of the sample has to be etched under the holes, so a plasma-assisted dry etching is performed using a ICP-RIE process. The Cr and Au layers already provide a protective mask for the active region, so that the etching takes place in the open holes only.

10. The sample undergoes a final ICP-RIE dry-etching, which defines the mesa of each device, with a typical thickness of $10\mu m$. In this case, a final litography of an etching mask is used to preserve the fabricated structures, as seen in figure 24.

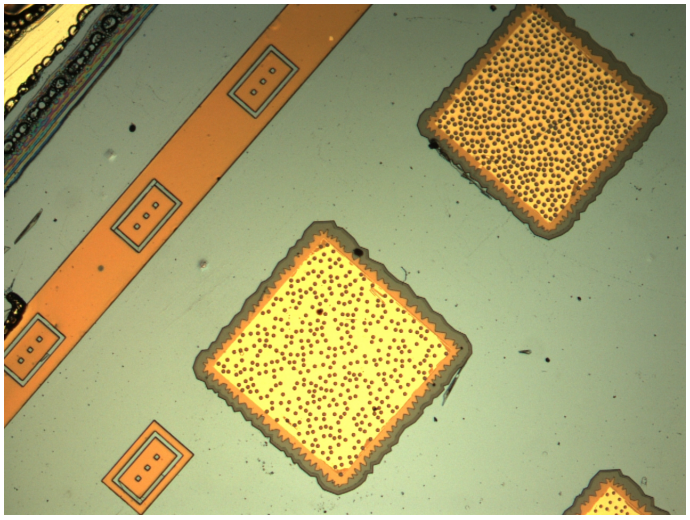

Figure 24: These random patterns are covered with the etching mask lithography, so that a protective film of resist preserves them during the ICP-RIE process. Therefore, the dry-etching excavates all around the patterns and defines the mesa of each laser.

11. The back metallization is realised with the deposition of Cr/Au ($10nm/110nm$), which is fundamental for the correct electrical contact of the device.

12. Finally, the wafer has to be cleaved to separate the fabricated devices, which are then indium-soldered on a copper submount with gold contact pads. Electric contact between the gold pads and the lasers is provided by gold wires with a diameter of $25\mu m$, connected using ultrasonic wire bonding.

Highly controlled conditions of the sample and the environment (low level of contaminating particles, specific temperature and pressure, air cleanliness, etc.) are required in most of the fabrication steps, which were performed into the cleanroom facility (ISO 7) of

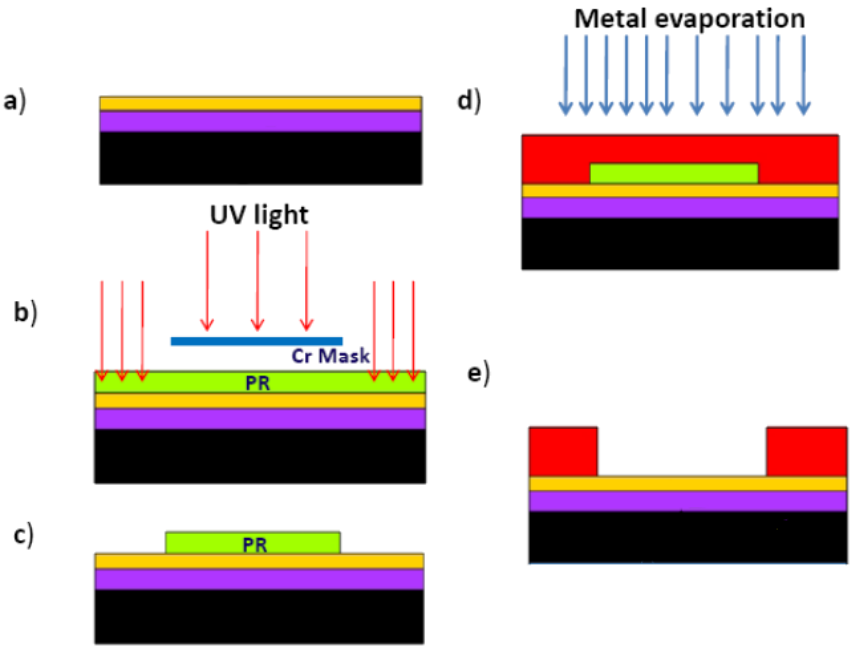

Figure 25: The bare substrate (a) is first spin-coated with a positive photoresist (PR), soft-baked and pre-developed. Then, it is UV-illuminated through a photomask as in (b), and after hard-baking and developing, only the non-exposed region of resist are left (c). A film of metal is deposited via thermal evaporation (d). After lift-off process, the designed metal region is finally defined on the substrate (e). The image is adapted from [33].

the NEST (National Enterprise for nanoScience and nanoTechnology) Laboratory in Pisa. Some of the steps of the fabrication process are shown in figure 25 and will be analyzed in detail in the following sections.

3.2.3 Optical lithography

Optical or UV ithography consists of patterning substrate by employing the interaction of beams of photons with materials [33]. This technique allows reproducing complex structures, such us photonic patterns, on a sample substrate. A photolithography system consists of a light source (typically, a Hg lamp), a mask, and an optical projection system. After preparing a photomask with the desired geometries, a uniform thin film of a a light-sensitive chemical ("photoresist") is opportunely spread on top of the active region, with a procedure called spin coating. By selectively illuminating some regions of the film with UV radiation thanks to the photomask, the designed geometries can be transfered to a "positive" resist, i.e. a type of photoresist which becomes soluble to a specific developer in the exposed zones. The used UV lithography procedure is described below.

- Spin coating: a droplet of photoresist *s*1818 is deposited on the sample, which undergoes a rotation at 4000 RPM for 1 minute to have an approximately 18μm-thick film. Unfortunately, the distribution of the resist is often not uniform at the corners, where mechanical removal of the exceeding resist is often used. This is crucial for the successive accurate alignment of the sample with the photomask.
- Soft-baking: the photoresist must be heated to ensure a good adhesion to the sample, but a prolonged baking may alter the photo-sensitivity of the resist. The typical recipe uses a soft baking at 90°C for 60s.

- Pre-development: before UV exposure, the resist-coated sample is immersed in the developer ($MF319$) for $20s$ and then in water to stop the reaction.

- UV exposure: the sample is loaded in the high-precision MJB3 mask aligner, equipped with an optical microscope. The photomask is placed between the sample and the mirrors conveying the UV radiation, so that it can pass through the transparent regions of the mask and illuminate the photoresist. The photomask and the sample should be as in contact as possible, to minimize the diffraction of light at the borders of the dark regions and reduce the undesired exposure of the masked parts. The two crucial parameters are the UV lamp intensity ($\approx 10 mW/cm^2$) and the exposure time (set to $\approx 20.5s$).

- Hard-baking: immediately after the exposure, the resist is heated at $120°C$ for $20s$. In order not to damage the pattern tranfered to the film, a very careful control of the baking time is needed.

- Final development: typically, the sample is immersed in the developer for nearly $25s$ and then in water again, for a similar time.

In each fabrication process, this protocol is applied first for the chromium border of each device, then it is repeated for the top metallization pattern and finally for the etching mask, to define the laser's mesa in the dry-etching procedure. For each of these successive exposure, the specific patterns are reproduced in dedicated fields of the photomask (see figure 26). A very tight control of the alignment of the already impressed geometries with the next photomask design is required, since even a shift of few μm or a small relative angle between them are crucial. To help optimize the alignment, a large number of reference markers were added to the inital CAD file of the photomask fields. These are clearly visible in 27.

3.2.4 Metal deposition and lift-off

The thermal evaporator allows thin-film deposition with the evaporation of a source material in a high-vacuum chamber. The sample and the metal to be deposited are placed in the chamber in an initial condition of very low pressure ($10^{-5} \div 10^{-6} mbar$), so that, after a sufficient heating of the source material, particles evaporate and travel directly to the target sample, without any collisions with the background gas. In order to have a uniform deposition, the target surface has to be as flat as possible and the pressure needs to be very low to avoid undesired reactions with other gases, which may alter the flow of vapour to the substrate. The thickness of the material deposited on the substrate is measured by a quartz crystal microbalance, which detects the change of the frequency of a quartz crystal resonator associated to a mass variation per unit area. At the end of the process, the sample surface is completely coated. However, if a previuosly exposed photoresist film is between the substrate and the metal layer, it is possible to reproduce the exposed pattern on the metal by a procedure called "lift-off". It consist in immersing the sample in a solvent like acetone, so that the soluble regions of resist are removed and the corresponding metal areas are cleared too. This process depends critically on the quality of the UV exposure, determined by the undercut profile, and the correct development of the resist. Sometimes the use of hot acetone and ultra-sonication was necessary for a complete lift-off, especially for the aperiodic air hole patterns in the top metallization of the devices.

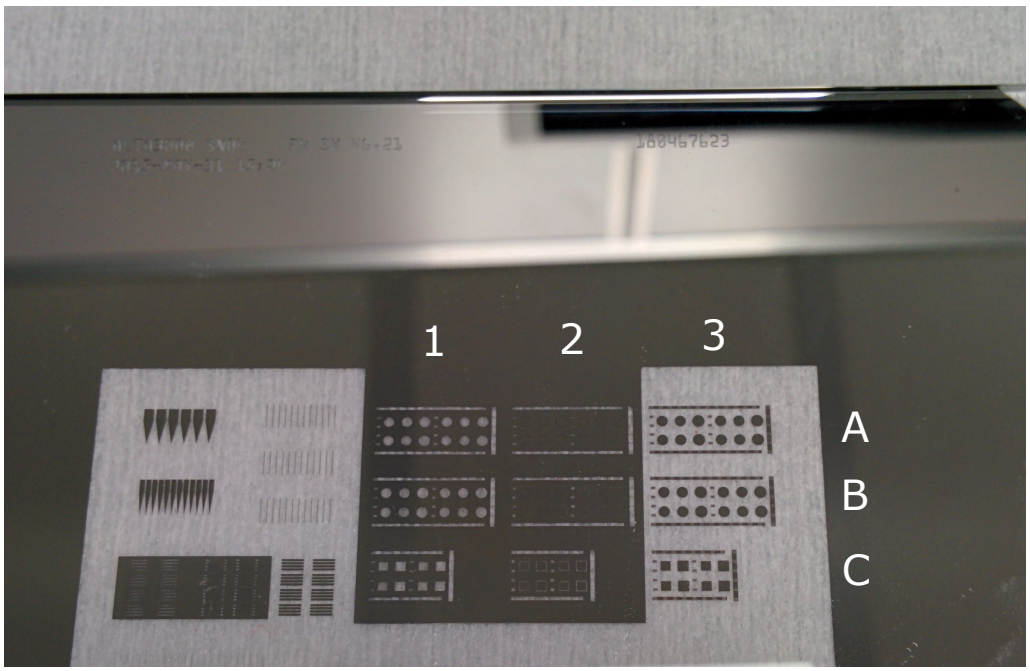

Figure 26: The part of the photomask with the designed quasicrystal and random geometries is shown in picture. The highly symmetric 7-fold devices (type-A) are in row A, the low symmetry 7-fold devices (type-B) in row B and the random geometries (type-C) in row C. Column 1 contains the hole patterns for the top metallization, column 2 hosts the shape for the external absorbing Cr border and column 3 features the larger etching masks. The geometries on the left are not used in this thesis work.

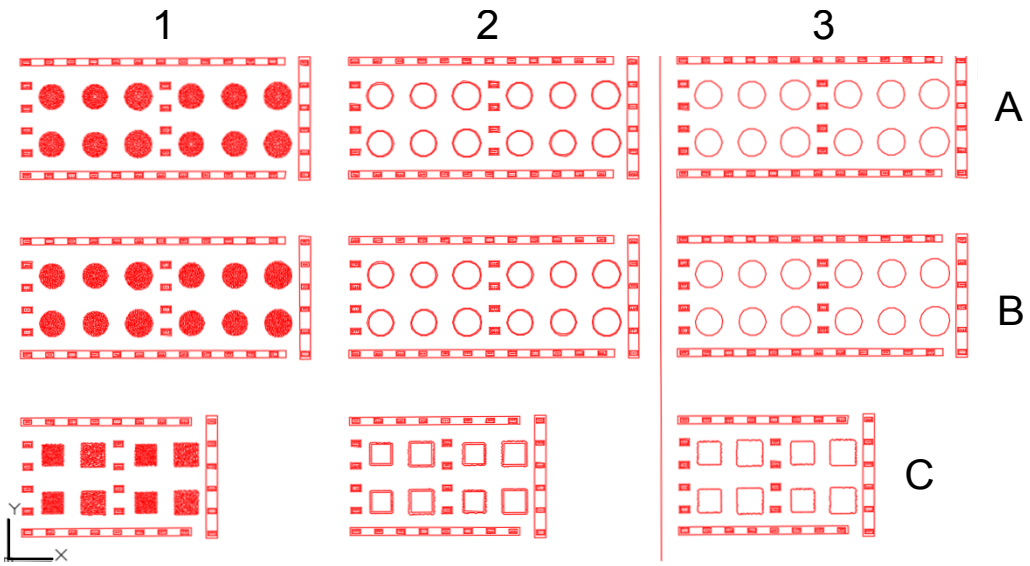

Figure 27: This scheme reports all the designed fields of the photomask. For the 7-fold resonators (1st row from top), six different devices having distinct filling factor $FF = 23.7\%, 24.4\%, 27.0\%, 27.4\%, 28.0\%, 28.4\%$ are present for type-A, while for type-B (2nd row) the chosen geometries have $FF = 23.3\%, 24.6\%, 25.0\%, 26.0\%, 27.1\%, 28.5\%$. Four random structures (3rd row) with $FF = 16.8\%, 20.2\%, 27.2\%, 29.8\%$ are in the lower part of the image. They are surrounded by a set of markers in a rectangular shape. Every set of six or four patterns is repeated to side, so that, when possible, multiple copies of the devices can be fabricated.

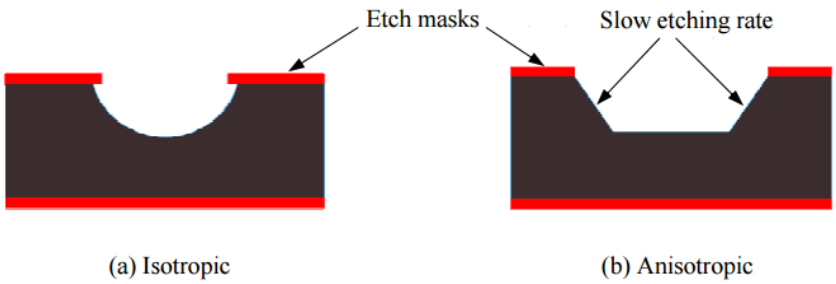

Figure 28: A scheme of the isotropic (a) and anisotropic (b) wet etching (adapted from [33]).

3.2.5 Wet etching

In wet ecthing processes, the sample is immersed in liquid-phase etchants to remove materials from its surface. In such processes, two properties are fundamental:

- selectivity: when etching a layered substrate, a poorly selective process not only removes the top layer, but also attacks the underlying material. A highly selective etchant has a rapid etching rate for the top material, while it has a much slower corrosion rate for the bottom materials. So it is possibile to complete the required etching without damaging the rest of the structure;
- isotropy: when the material is attacked, most reactions tend to erode equally in all directions and form sloping sidewalls. Typically, this effect has to be minimized to form well-defined, vertical structures. For some etchants, the etching rate depends on the crystallographic orientation of the substrate, so that a high anisotropy is achieved (see figure 28).

In the fabrication procedure, wet etching was used twice. As mentioned, the sample's GaAs substrate was removed by a solution of citric acid and water (1 : 1), with the addition of 1/3 volume of H_2O_2. This etching is highly selective, since the etching rate diminishes abruptly when the $Al_{0.5}Ga_{0.5}Al$ etch stop layer is exposed. Then, this last protective layer is removed by a rapid etching in fluoridric acid (HF) with a concentration of 48%.

3.2.6 Plasma-assisted dry etching

Plasma-assisted dry etching uses the ICP-RIE technology, i.e. the "inductively coupled plasma for reactive-ion etching", characterized by a well controlled etching rate and vertical sidewalls. The sample is loaded in the high-vacuum ($\approx 10^{-6}$) chamber of the machine, where different type of gases are pumped (BCl_3, Cl_2 and Ar) at specific concentration and used to produce a plasma. The plasma is generated by a high frequency ($2.4GHz$) source field, while the ion acceleration is separately driven by a radiofrequency field at a lower frequency ($13.56MHz$), so that the concentration of the chemicals in the plasma and the ion energy of impact on the sample are independent parameters. The resulting advantage of this technique with respect to the conventional wet etching is the tighter control of the undercut and the etching depth. In fact, the process recipe can be accurately calibrated to tune the two involved etching mechanisms:

- physical etching: it is associated to impact of the accelerated particles and is mainly determined by the Argon concentration and the applied acceleration field;

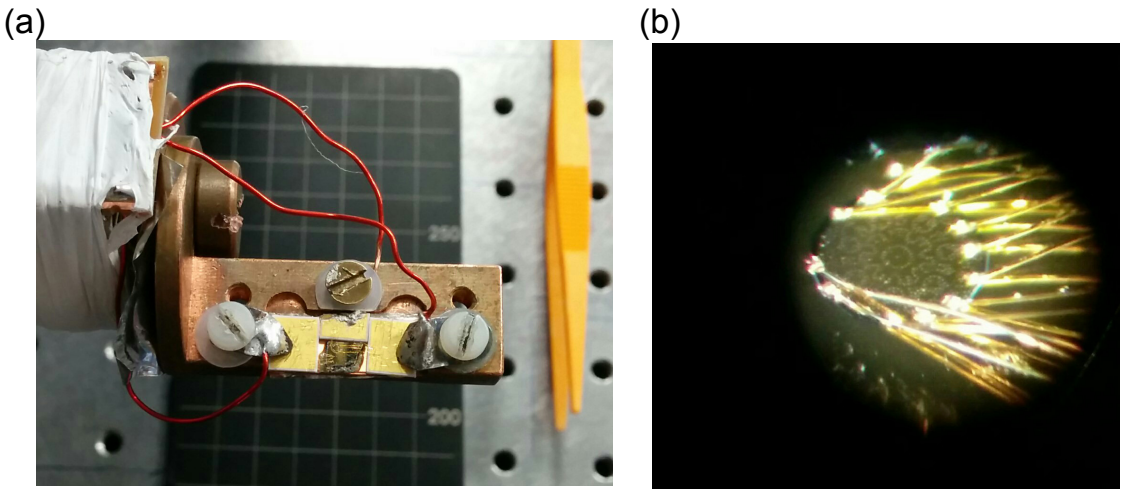

Figure 29: In (a), the gold-coated ceramic pads are connected to both the cryostat contacts and the devices. In the latter case, gold wires with a diameter of $25\mu m$ are wedge bonded to the lasers, as shown in the optical microscope image in (b).

- chemical etching: it is controlled by the concentration of chlorine gases, since Cl is strong oxidizing agent.

In this thesis work, dry-etching was used for both the etching of the contact layer in corrispodence of the holes of the top metallization, and the definition of the mesa of the devices. In the first case, the used recipe featured a concentration of $BCl_3 : Cl_2 : Ar$ $(6 : 1 : 10)$, a pressure of $0.2Pa$, a source power of $100W$ for plasma generation and $25W$ of power for the plasma acceleration. The etching rate is roughly $1.8nm/s$. In the second case, the composition is $BCl_3 : Cl_2 : Ar$ $(5 : 5 : 5)$, with a pressure $0.2Pa$, source power $500W$ and acceleration RF power $30W$. The etching rate of the heterostructure is $\approx 10nm/s$.

3.2.7 Final mounting

After all these fabrication steps, the wafer containing the devices is cleaved and they are mounted on a rectangular copper submount with a thickness of few millimeters. The submount surface is large enough to host the gold-coated ceramic pads for the electrical contact and the fabricated QCL, which has a surface of $\approx 0.5 \div 0.7mm^2$, as explained in the next chapter. The ceramic components provide the electrical isolation of the gold coating from the copper submount, while the cryostat contacts are connected to these conductive gold layers to drive the device (see figure 29.a). This is achieved through the use of a ultrasonic wedge-bonding technique, which allows inteconnecting the gold pads and the devices with gold wires with a diameter of $25\mu m$. The two ends of such wires are attached to the target surfaces by the ultrasonic vibration of a bonding wedge, which pins the wire against the surface (figure 29.b). The bottom of the samples is indium soldered at a temperature of $160°$ C, in order to ensure a good thermal contact between the devices and the submount, which is crucial for the control of the operating temperature of the laser. Usually, each submount hosts two devices, each having a dedicated contact pad to allow a separate electrical control.

3.3 TRANSPORT CHARACTERIZATION

3.3.1 Pulser

The fabricated QCLs are electrically driven by a pulser, which is a voltage generator providing short, periodic voltage pulses. The main parameters of a pulser are the applied voltage, the repetition rate of the pulse (i.e. the frequency ν) and its temporal duration or "pulse width" PW. A commonly used quantity is the duty cycle DC, i.e. the percentage of one period in which the signal is active, obtained by the formula

$$DC = PW \cdot \nu \tag{136}$$

The used pulser by Avtech Electrosystems Ltd. has a maximum voltage of $250V$ and a maximum current of $7A$, while the pulse width can be varied in the range $\nu = 100ns \div 100\mu s$. The maximum pulse frequency is $\nu = 100kHz$ and the DC can be set up to a value of 4%.

3.3.2 Cryostat

During the transport characterization of the devices, they were cooled into a closed-cycle helium cryostat. It consists of a chamber through which cold helium vapour is pumped and then recycled. The devices are cooled inside a vacuum chamber by attaching their submount to a holder ("cold finger") at the end of a metallic cylinder, which is in thermal contact with the helium chamber. The vacuum chamber is at a low pressure (usually, $\approx 10^{-5}mbar$) and the typical temperature of the sample is $10K$, as monitored via a temperature sensor. If necessary, it can also be varied thanks to a heater, as done when characterizing the thermal beahaviour of some lasers (see chapter 5).
The electrical contact is provided by a system of micro-coaxial cables which allows driving up to two devices per submount at the same time, while a system of resistors provides the required impedence matching for the lasers.

3.4 OPTICAL CHARACTERIZATION AND FTIR

3.4.1 Pyroelectric detector

The used pyroelectric detector is a sensor which exploits a temporary voltage induced by a temperature variation of a crystal, due to the incident THz radiation of the tested laser. When the THz radiation is collected by the sensitive area of $\approx 7mm^2$ of the detector, it produces a voltage signal which is correlated to the intensity of the beam at the position of the sensor. The signal is also filtered by a lock-in amplifier, sensitive to both frequency and phase, reducing the noise thanks to a square wave modulation with a frequency of $33Hz$ and a peak-to-peak voltage of $5V$. The sensitivity of the detector is measured by the noise-equivalent power (NEP), which is the signal power giving a signal-to-noise ratio equal to 1, in an integration time of $0.5s$. In this case, the sensor has $NEP = 0.5nW/\sqrt{Hz}$.
During the combined measurements of the current-voltage characteristics, the pyroelectric sensor was placed in front of the device, at a fixed distance of $1.5cm$, to collect the radiation emitted by the laser and transmitted through the thermoplastic cyclic olefin cryostat window, with a transmission coefficient of 78%.
The scheme of the whole system is reported in figure 30.

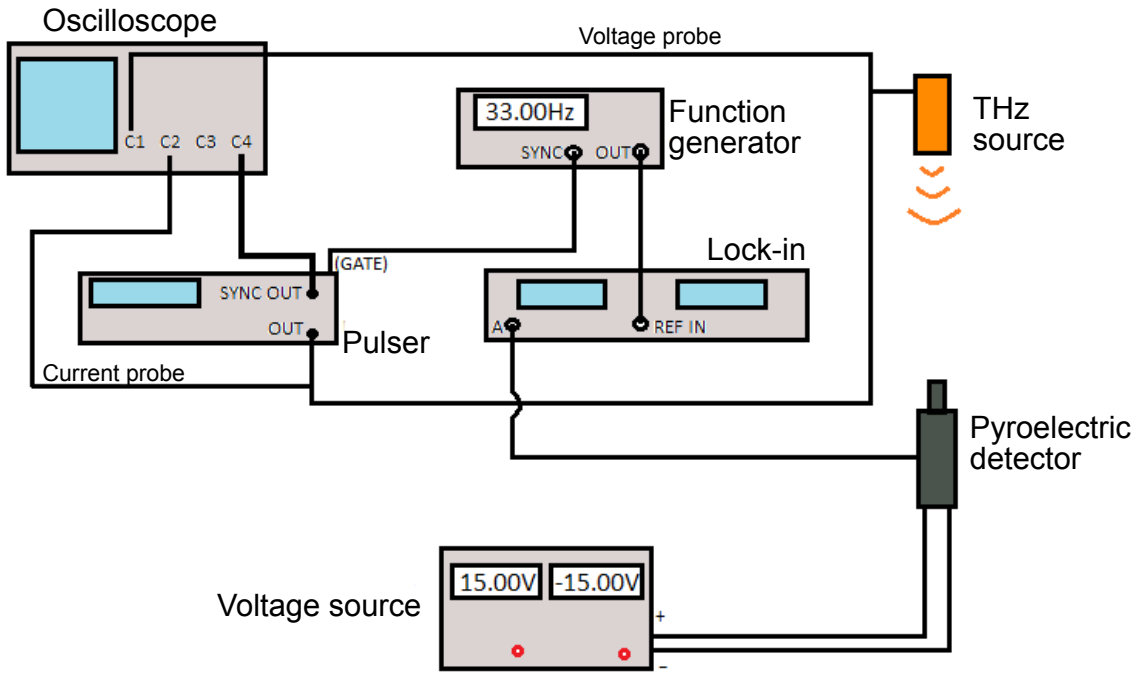

Figure 30: The scheme represents the system used for the electrical and optical characterization of the fabricated QCLs.

3.4.2 Far field measurements

The far field profile of a laser is the pattern of its intensity measured at a distance L much larger than its typical wavelength $\lambda << L$. In fact, the far field is experimentally measured some centimeters away from the laser, so the radiation distribution can be calculated by the Stratton-Chu approximation [34]. In order to measure the far field profile of the vertically emitted intensity of a QCL, the pyroelectric sensor was mounted on a holder at a fixed distance of $\Delta z = 4.5cm$ from the surface of the laser, which was in turn placed on the frontal cold finger of the cryostat. The position of the detector in the perpendicular $x - y$ plane was varied by two computer-controlled, motorized linear stages. This allowed scanning the intensity distribution in a rectangular region with sides $\Delta x = 9 \div 12cm$ and $\Delta y = 9 \div 12cm$ for the different devices. The resolution of the measurement is determined by the detector displacement at every acquisition ($3mm$). Another important condition is the integration time ($300ms$), which is more than twice the lock-in characteristic time.

3.4.3 FT-IR spectroscopy

The Fourier transform infrared (FT-IR) spectroscopy is a technique which allows detecting the emission frequencies of the fabricated lasers with a sensitivity highly dependent on the selected resolution step.. Unlike a dispersive instrument, for example a grating monochromator, an FT-IR spectrometer collect all wavelengths simultaneously.
The instrument is based on a Michelson interferometer, consisting of a fixed mirror, a beam splitter and a mirror that translates back and forth, very precisely. In the performed experiments, the source of radiation is a fabricated THz QCL. The beamsplitter (BS) separates the incoming radiation (which may consists of multiple wavelengths) in two beams: the first one is transmitted through the BS to the fixed mirror, while the second beam is reflected off the BS to the moving mirror. The fixed and moving mirrors reflect

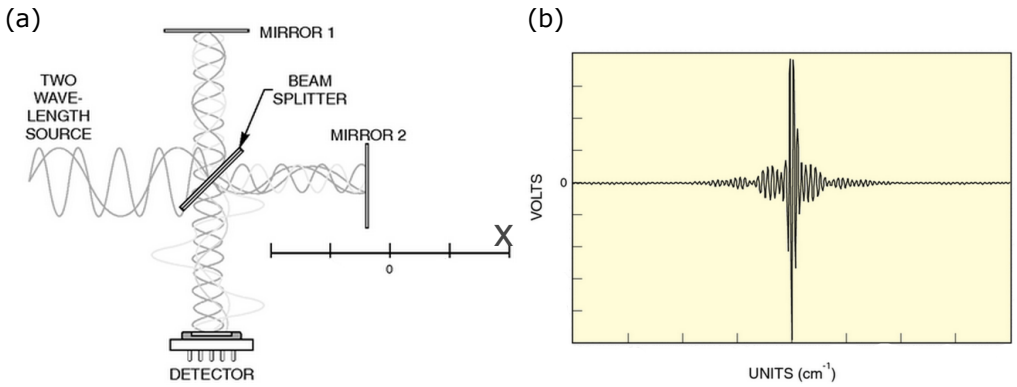

Figure 31: Schematic representation of the propagation of two waves with different wavelengths in the two arms of the interferometer in (a). A skecth of the typical profile of an interferogram is shown in (b).

the radiation back to the BS, and this results in one beam passing to the detector and the second back to the source (see figure 31.a). The optical path difference between the beams travelling through the two arms of the interferometer is determined by the position of the moving mirror, which is initially at the same distance from the BS as the fixed mirror. For a mirror displacement Δ, the corresponding optical path difference is $OPD = 2n\Delta$, where n is the refractive index of the medium filling the interferometer arms.

By changing the position of the moving mirror with discrete steps, the intensity of radiation is measured by a detector, producing a profile called interferogram. As the optical path difference grows, different wavelengths create peak signals at distinct points, though the plot shows a centerburst for $\Delta = 0$, when the optical path difference is zero and all the wavelengths are in-phase, so they constructively interfere giving a huge intensity (figure 31.b). The interferogram is often plotted as a function of the OPD or of the radiation wavenumber (in cm^{-1}) and its resolution depends only on the maximum optical path difference. In this thesis work, a FTIR spectrometer by Thermo Fisher Scientific Inc. was used, having interferometer arms with $n = 1$ and a maximum resolution of $0.125cm^{-1}$, corrisponding to $OPD = 8cm$. The measurements were performed using a DTGS-KBr detector, so that the noise equivalent power was $NEP = 0.5nW/\sqrt{Hz}$.
From the Fast Fourier Transform of the interferogram, the emission spectra of the source is finally obtained.

4 DESIGN OF 7-FOLD QUASI-CRYSTAL AND RANDOM THZ LASERS

In this chapter, the results of the two-dimensional simulations of the designed patterns are reported. Calculations are performed by meshing the whole surface and using the effective refractive index approximation introduced in chapter 3. The effective indices are $n_s = 2.8$ for the dielectric scatterers, $n_b = 3.6$ for the semiconductor heterostructure and $n_c = 3.6 + i$ for the partially absorbing chromium border. A region of air ($n_a = 1$) surrounds the system, as a proper configuration to apply the scattering boundary conditions. These input data are used to study the TM-polarized eigenmodes (useful for gain in a THz QCL) and their quality factors in the broad spectral range $2.7 \div 3.8 THz$, which is divided into discrete intervals of $80 GHz$. All approximations involving the frequency are then made locally, so that calculations are better refined.
For each type of disordered pattern and size of the device, the scatterer radius is varied by discrete steps of $1 \mu m$, keeping the filling factor in the range $\approx 0.2 \div 0.3$ where a sufficient degree of scattering and outcoupling can be achieved, without overly increasing the waveguide losses and worsening the optical confinement.

4.1 TYPE-A: DESIGN OF THE HIGHLY SYMMETRIC 7-FOLD DEVICES

4.1.1 Type-A: devices with area A=0.53mm^2

The first highly symmetric 7-fold photonic quasicrystal is generated by setting the GDM code parameters to $\mathcal{N} = 50$, $\alpha = 0$ and $\beta = 0$. The structure has the following fixed geometrical properties:

- outer radius $R = 411 \mu m$ and area of $A = 0.53 mm^2$
- number of scatterers (air holes) in corrispondence of the quasicrystal vertices $N = 589$
- quasilattice parameter $a = \sqrt{A/N} \approx 29.9 \mu m$
- a $20 \mu m$-wide chromium border is all around, with a 14-sided polygon shape

A set of 31 simulation runs was performed, varying the scatterer radius between $r = 5.8 \mu m \div 8.9 \mu m$ with discrete steps of $1 \mu m$. Therefore, the filling factor is in the range $FF = 0.19 \div 0.30$. For every simulation, the most favoured (high-Q) modes are identified, as they emerge from the background of low-Q modes.
By visually comparing the spatial distribution of the electric fields E_z with similar frequencies for different FF, it is possible to trace the evolution of the mode frequency with the change of the geometrical parameters (see figure 32.a), until their quality factor diminishes and makes them disappear in the low-Q region. It can be notice that all modes undergo a frequency shift of the order of $50 GHz$ at every radius increment of $1 \mu m$. This can be roughly explained in the framework of the plane wave model: at every increase of r, the distance between scatterers is reduced by $2\Delta r$, so that a plane wave readapts and shortens its wavelength λ, resulting in a higher frequency ν. This geometry provides a few high-Q modes between $2.8 THz$ and $3.2 THz$, while all the others are concentrated

around $3.5THz$. In general these high-frequency modes also show the highest quality factors. As shown in figure 32.b, the general trend is an increasing Q with higher FF in the explored range, up to a maximum of $Q \approx 155$. Apparently, intermediate values of FF ($0.23 \div 0.26$) can produce a large number of coexisting modes with relatively high quality factors, ranging from $Q \approx 110$ for mode B to $Q \approx 150$ for mode P. Some examples of the spatial profile of the fields are shown in figure 33.

4.1.2 Type-A: devices with area A=0.64mm^2

Photonic strutures of type-A were then studied by varying the resonator area. This allows reducing the diffraction effect due to the long wavelength of THz radiation. Unfortunately, a larger surface also implies a higher current threshold and more self-heating, which are extremely negative for the operation thermal behaviour of a THz QCL. In this case, the geometry is exactly the same pattern seen in the previous section, just rescaled by a factor 1.09. Therefore the structure is characterised by:

- outer radius $R = 450\mu m$
- area $A = 0.64mm^2$
- number of quasicrystal vertices/dielectric scatterers $N = 589$
- quasilattice parameter $a = 32.7\mu m$
- a 14-sided Cr border with a width of $20\mu m$ is all around the quasicrystal structure

The filling factor range is left unchanged: $FF = 0.19 \div 0.30$. The plot of the high-Q mode frequencies and quality factors are reported in 32.a and 32.b, respectively. A large number of degenerate modes is present, with almost complementary spatial profiles and a frequencies differing by less than $1GHz$. An example is reported in figure 34 (plots c and d). In this configuration, no modes with significantly high quality factors are reported for $\nu < 3.1THz$. Few, excellent Q factors ($\approx 150 \div 175$) appear for extreme values of the filling factor, especially for $FF < 0.21$ and $FF > 0.27$, in contrast with the behavior found for the smaller device with $A = 0.53mm^2$. Instead, a common feature is the presence of more modes, with smaller Q, in the intermediate region $FF \approx 0.23 \div 0.25$.

4.2 TYPE-B: DESIGN OF THE LOWLY SYMMETRIC 7-FOLD DEVICES

4.2.1 Type-B: devices with area A=0.53mm^2

The lowly symmetric 7-fold quasicrystal is produced by using the parameters $\mathcal{N} = 50$, $\alpha = 1$ and $\beta = 0$ in our MATLAB code. The structure has the following characteristics:

- outer radius $R = 411\mu m$
- area $A = 0.53mm^2$
- number of quasicrystal vertices/dielectric scatterers $N = 637$
- quasilattice parameter $a = 28.9\mu m$
- a $20\mu m$-wide Cr border, always in a regular 14-sided shape

The plots for the frequencies of the eigenmodes and their quality factor are shown in 36.a and 36.b, as functions of the filling factor. The presence of defect points reduces the degree of symmetry with respect to type-A devices, so that the spatial profile of the electric field E_z is, in general quite, irregular (figure 37) and the mode degeneracy (common in type-A) is lifted almost completely. Generally, Q factors are lower in this case than in the highly symmetric devices (with a peak of $Q \approx 130$ for mode A), though high-Q modes are again mostly concentrated above $3.1THz$. In this case, the central region $FF \approx 0.22 \div 0.28$ features three modes clearly emerging at $Q > 120$, while some less favoured ones still exists over a larger interval.

4.2.2 Type-B: devices with area A=0.64mm^2

Unlike the larger type-A geometry, this structure is not a rescaled version of the small type-B pattern. In this case, the larger size of the device is obtained by taking a larger number of points of the lowly symmetric 7-fold quasicrystal. Hence, the explored filling factors are not exactly the same as in the laser with $A = 0.53mm^2$. The main features of this structure are:

- outer radius $R = 450\mu m$
- area $A = 0.64mm^2$
- number of quasicrystal vertices/dielectric scatterers: $N = 759$
- quasilattice parameter $a = 29\mu m$
- a $20\mu m$-wide Cr border, always in a regular 14-sided shape

The dependence of the frequencies and the quality factors of the eigenmodes on the filling factor are clearly reproduced in the plots of figure 38.a and 38.b. The structure privileges modes with in the high-frequency region $\nu > 3.1THz$, whose spatial profile shows only a slight reminiscence of the 7-fold symmetry, due to the increase of disorder by the addition of the outer points (see 39).

4.3 TYPE-C: DESIGN OF RANDOM DEVICES

4.3.1 Type-C: devices with area $A = 0.45mm^2$

This first random geometry is produced by the pseudo-random number generator of MATLAB, extracting the position of the scatterers from a uniform distribution of probability over a square region, as explained in chapter 3. The main characteristics of this structure are:

- square side $L = 670\mu m$
- area $A = 0.45mm^2$
- number of dielectric scatterers $N = 580$
- average intersite distance $a = 27.9\mu m$
- an approximately $25\mu m$-wide Cr border with a highly irregular shape. This is beneficial to suppress feedback effects provided by resonator size.

These random photonic structures were studied for a scatterer radius equal to $r = 7.0 \div 8.9\mu m$, i.e. for filling factors $FF = 0.24 \div 0.32$. The plots in 40.a and 40.b indicate that the quality factors are much lower than in all the 7-fold structures, since even the most favored modes have $Q < 90$ for all the examined FF. It can be noticed that for $FF < 0.29$ most modes are concentrated in the spectral interval $2.9 \div 3.3THz$, while for larger filling factors new modes at higher Q appear in the higher frequency region $3.2 \div 3.6THz$. The simulated profiles E_z of the eigenmodes are quite extended over the entire structure, as visible in the plots 41.

4.3.2 Type-C: devices with area $A = 0.59mm^2$

This other random geometry consists of a different computer-generated distribution of the scatterers with respect to the previous disordered pattern of type-C. In this case, a larger square and a lower number of scatterers allowed studying the behaviour of light in a weakly scattering photonic structure, whose parameters are:

- square side $L = 770\mu m$
- area $A = 0.59mm^2$
- number of dielectric scatterers $N = 395$
- average intersite distance $a = 38.6\mu m$
- an approximately $25\mu m$-wide Cr border with a highly irregular shape.

This means the filling factor lie in the interval $FF = 0.16 \div 0.23$, i.e. the scatterer radius is varied in $r = 6.0\mu m \div 8.9\mu m$. The resulting eigenmodes' frequencies and qualiy factors are indicated for different FF in figures 42.a and 42.b, respectively. In this case, the quality factors are so uniform that it is difficult to clearly recognize the modes emerging from the low-Q background. Differently from the random geometry with smaller area, the high-Q modes are well distributed in the whole computed spectral range. Some of the spatial distribution of the field component E_z are reported in 43.

4.4 GEOMETRIES SELECTED FOR FABRICATION

After studying the modes' frequencies and quality factors for the mentioned geometries with a total of ≈ 200 simulation runs, sixteen patterns were chosen to be reproduced on a photomask and then fabricated. The selected photonic structures are listed below.

- *Type-A*: 7-fold highly symmetric quasi-crystal
  area $A = 0.53mm^2 : FF = 23.7\%,\ 24.4\%,\ 27.4\%,\ 28.4\%$
  area $A = 0.64mm^2 : FF = 27.0\%, 28.0\%$

- *Type-B*: 7-fold lowly symmetric quasi-crystal
  area $A = 0.53mm^2 : FF = 24.6\%,\ 26.0\%,\ 27.1\%,\ 28.5\%$
  area $A = 0.64mm^2 : FF = 23.3\%, 25.0\%$

- *Type-C*: random patterns
  area $A = 0.45mm^2 : FF = 27.2\%, 29.8\%$
  area $A = 0.59mm^2 : FF = 16.8\%, 20.2\%$

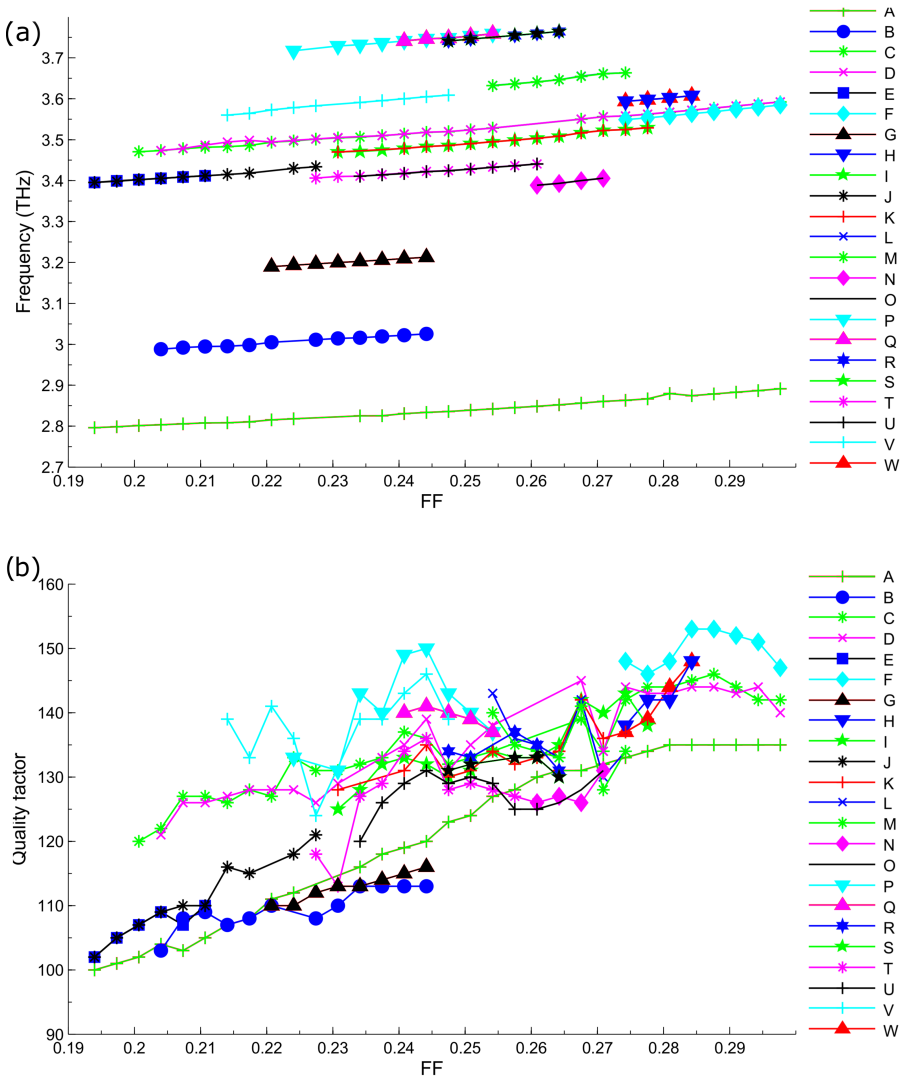

Figure 32: The plots in (a) and (b) show the frequencies and the associated quality factors of most of the high-Q eigenmodes as functions of FF, for type-A resonators ($0.53mm^2$).

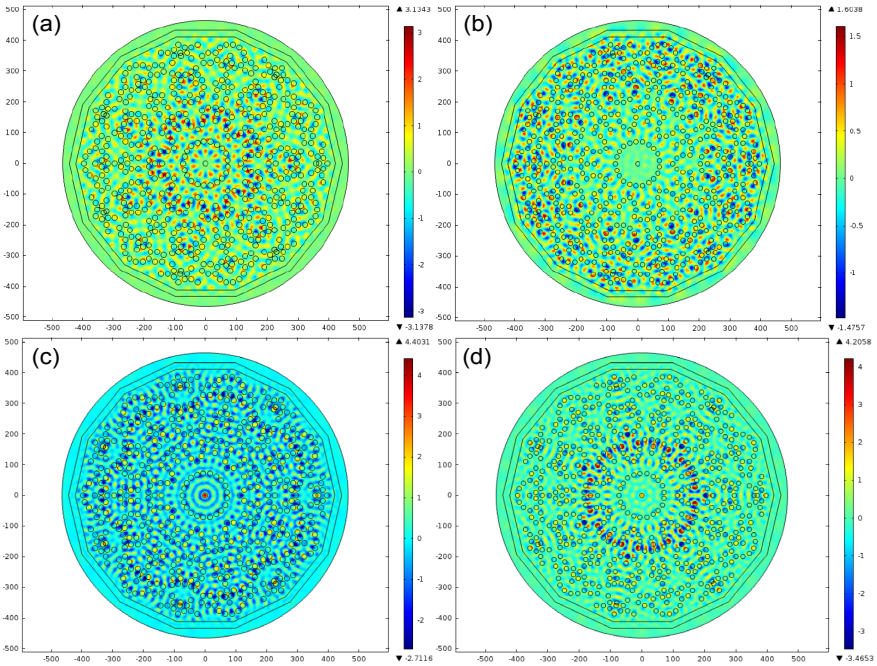

Figure 33: The computed field E_z is shown for the modes A ($\nu_A = 2.80 \div 2.89 THz$) in (a), B ($\nu_B = 2.99 \div 3.03 THz$ for varying FF) in (b), F ($\nu_F = 3.56 \div 3.59 THz$) in (c) and V ($\nu_V = 3.56 \div 3.61 THz$) in (d). The color scale indicates the value of the field in V/m in these plots, as well as in all the following ones. [Type-A resonators, $0.53mm^2$]

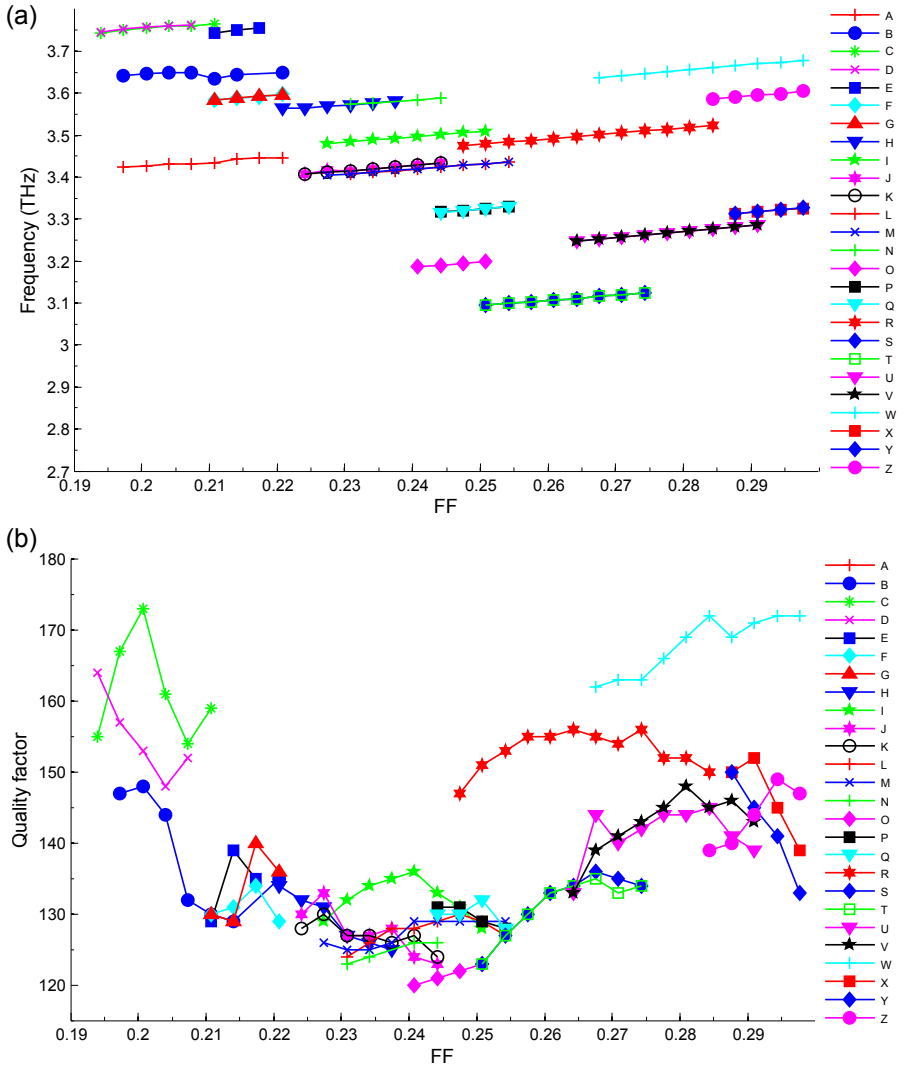

Figure 34: The plots in (a) and (b) show the frequencies and the associated quality factors of most of the high-Q eigenmodes as functions of FF, for type-A resonators ($0.64mm^2$).

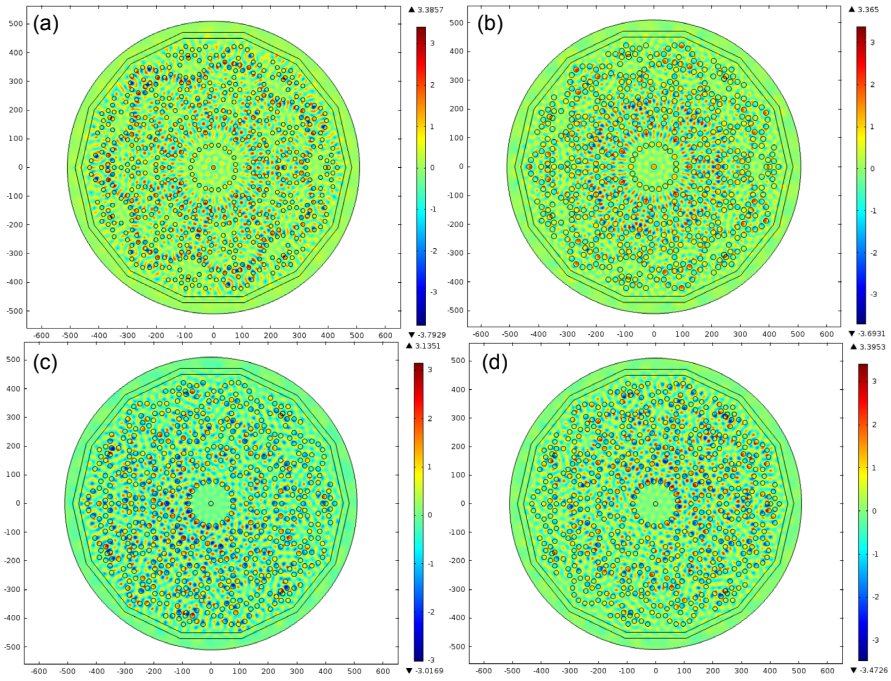

Figure 35: The field E_z (in V/m) is shown for the modes A ($\nu_A \approx 3.43THz$) in (a), R ($\nu_R \approx 3.48 \div 3.52THz$ for varying FF) in (b). The computed modes P ($\nu_P \approx 3.33THz$) in (c) and Q ($\nu_Q \approx 3.33THz$) in (d) are examples of degenerate modes, having the same frequency and complementary spatial profiles. [Type-A resonators, $0.64mm^2$]

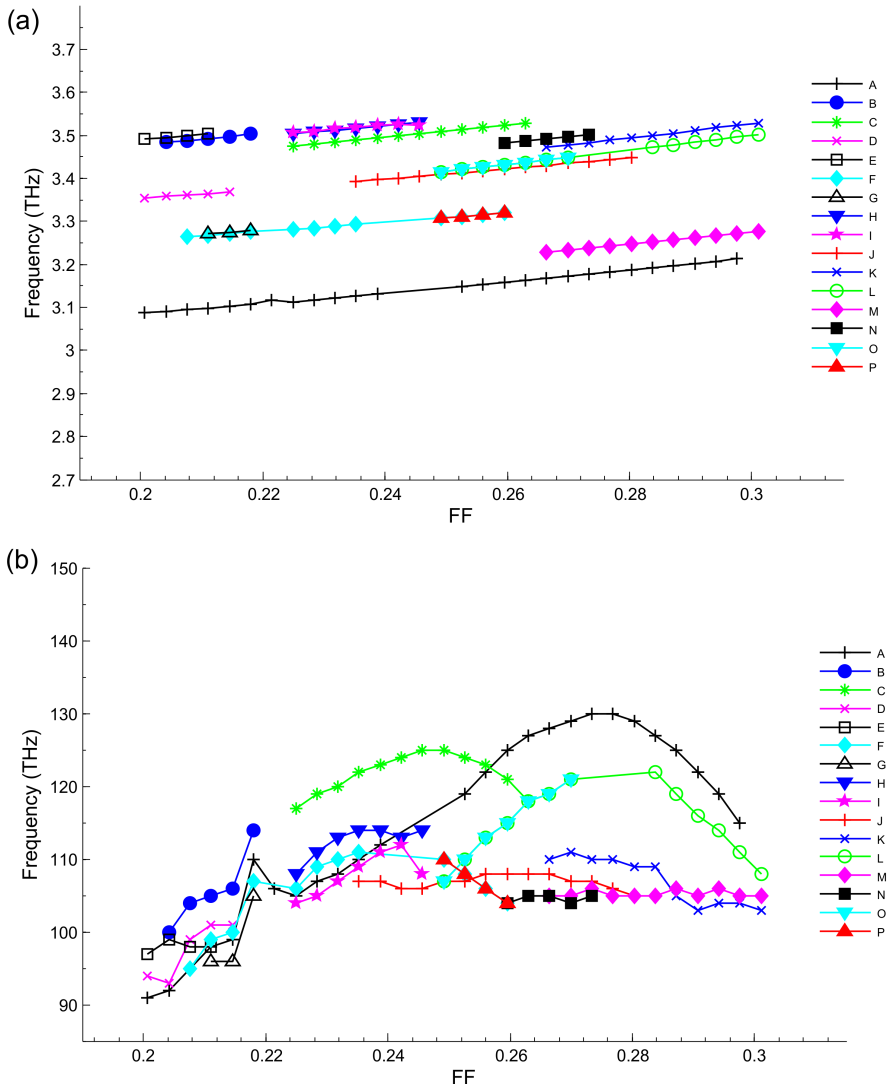

Figure 36: The plots in (a) and (b) show the frequencies and the associated quality factors of most of the high-Q eigenmodes as functions of FF, for type-B resonators ($0.53mm^2$).

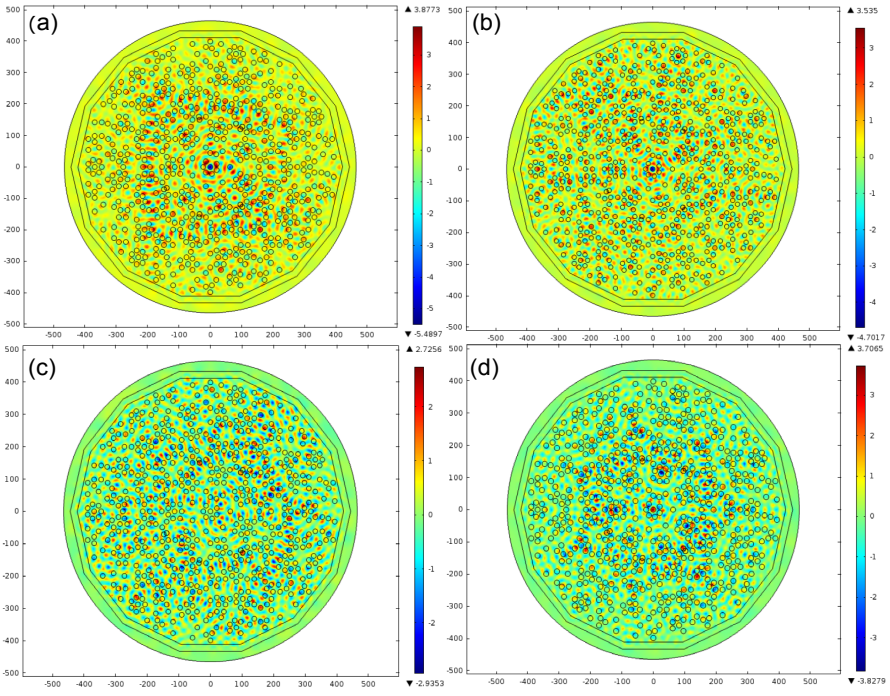

Figure 37: The field E_z (in V/m) is shown for the modes A ($\nu_A = 3.09 \div 3.21 THz$ for varying FF) in (a), C ($\nu_C \approx 3.48 \div 3.53 THz$) in (b), J ($\nu_J = 3.39 \div 3.45 THz$) in (c) and L ($\nu_G = 3.42 \div 3.50 THz$) in (d). [Type-B resonators, $0.53mm^2$]

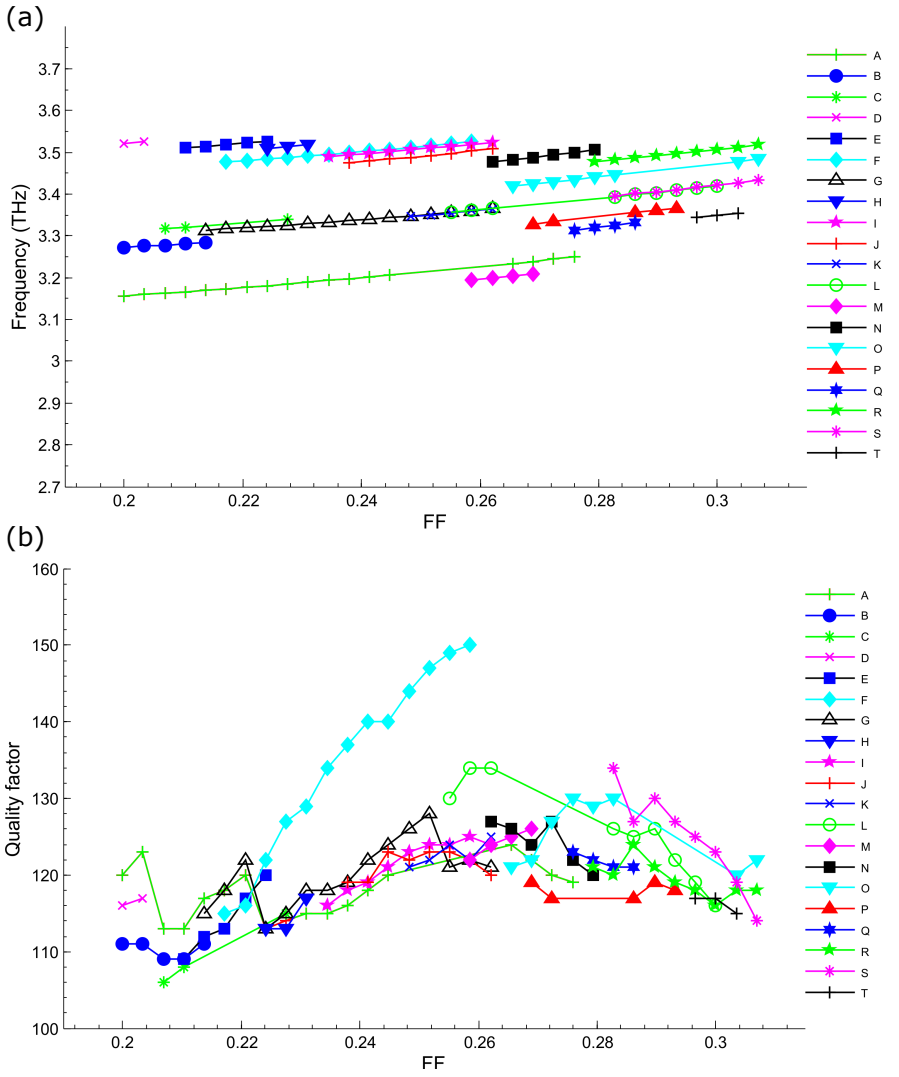

Figure 38: The plots in (a) and (b) show the frequencies and the associated quality factors of most of the high-Q eigenmodes as functions of FF, for type-B resonators ($0.64mm^2$).

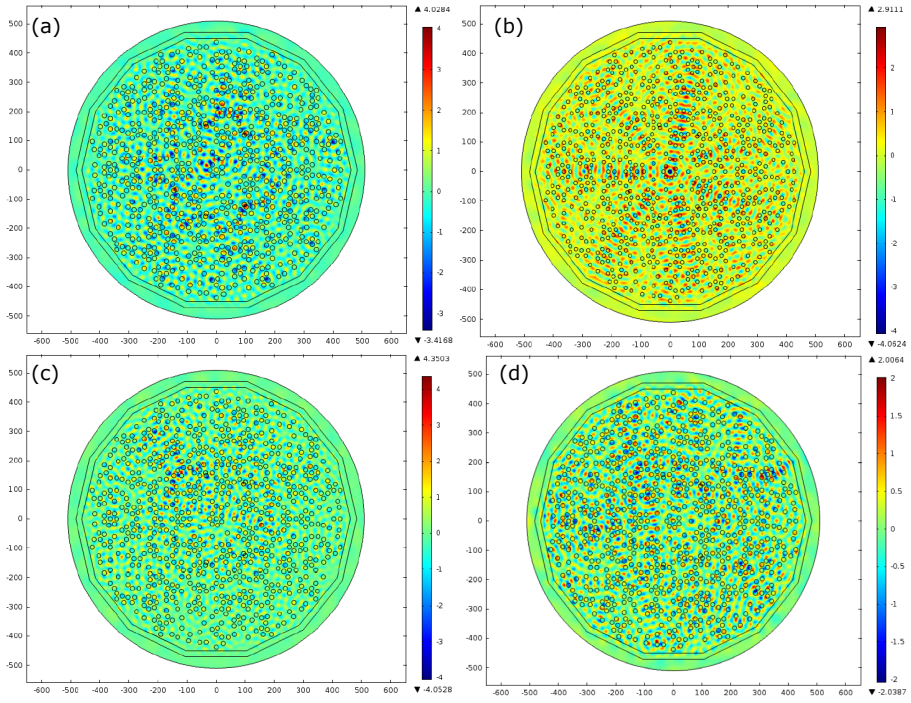

Figure 39: The field E_z (in V/m) is shown for the modes A ($\nu_A = 3.16 \div 3.25THz$ for varying FF) in (a), B ($\nu_B \approx 3.27THz$) in (b), F ($\nu_F = 3.48 \div 3.53THz$) in (c) and G ($\nu_G = 3.31 \div 3.37THz$) in (d). [Type-B resonators, $0.64mm^2$]

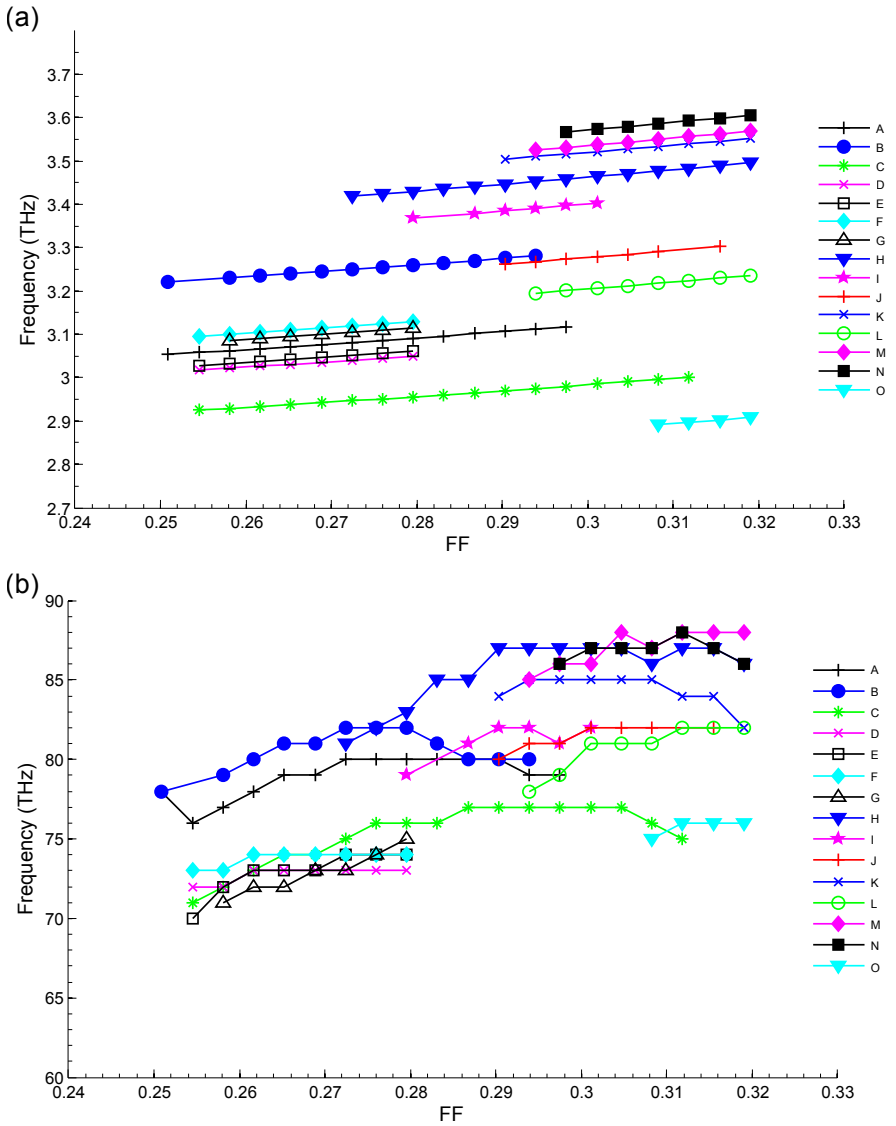

Figure 40: The plots in (a) and (b) show the frequencies and the associated quality factors of most of the high-Q eigenmodes as functions of FF, for type-C resonators ($0.45mm^2$).

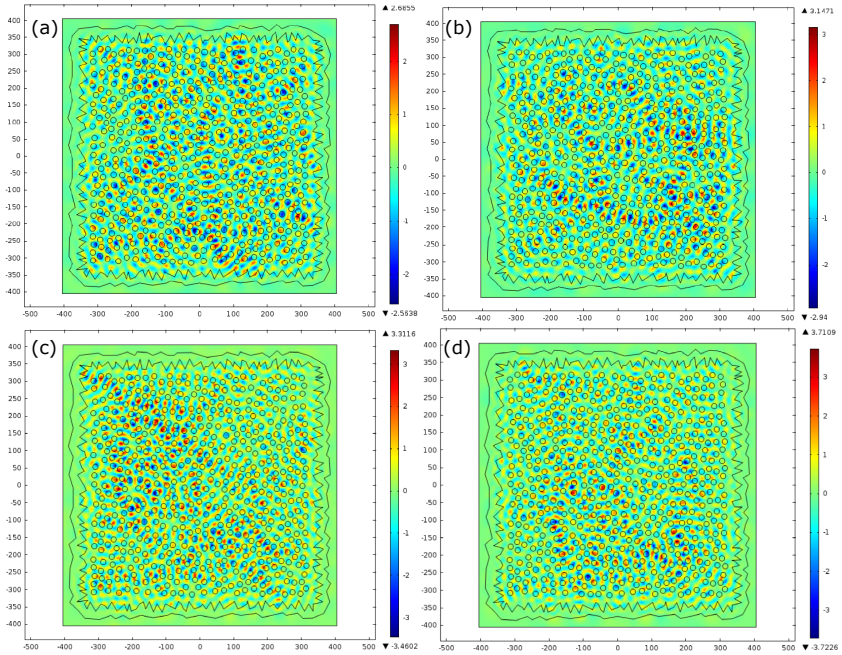

Figure 41: The field E_z (in V/m) is shown for the modes A ($\nu_A = 3.06 \div 3.12 THz$ for varying FF) in (a), C ($\nu_C = 2.92 \div 3.00 THz$) in (b), H ($\nu_H = 3.42 \div 3.50 THz$) in (c) and I ($\nu_I \approx 3.38 THz$) in (d). [Type-C resonators, $0.45mm^2$]

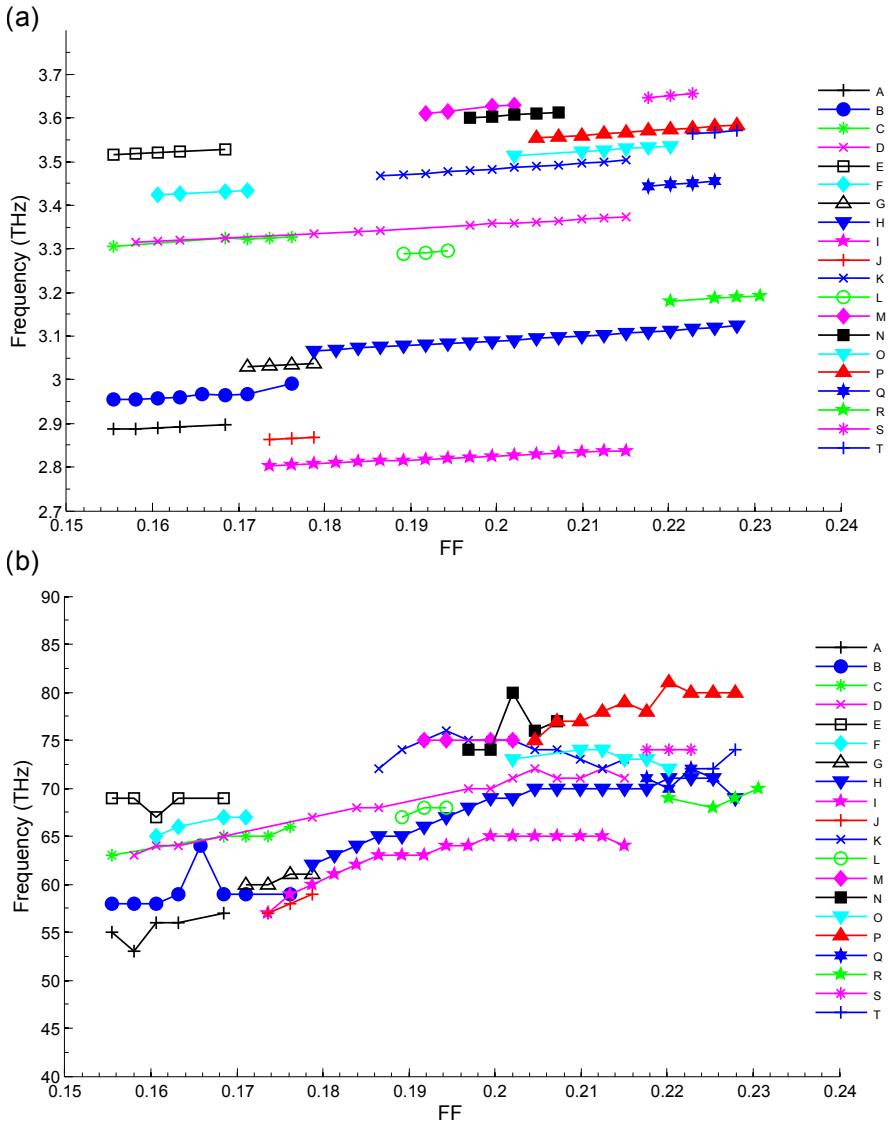

Figure 42: The plots in (a) and (b) show the frequencies and the associated quality factors of most of the high-Q eigenmodes as functions of FF, for type-C resonators ($0.59mm^2$).

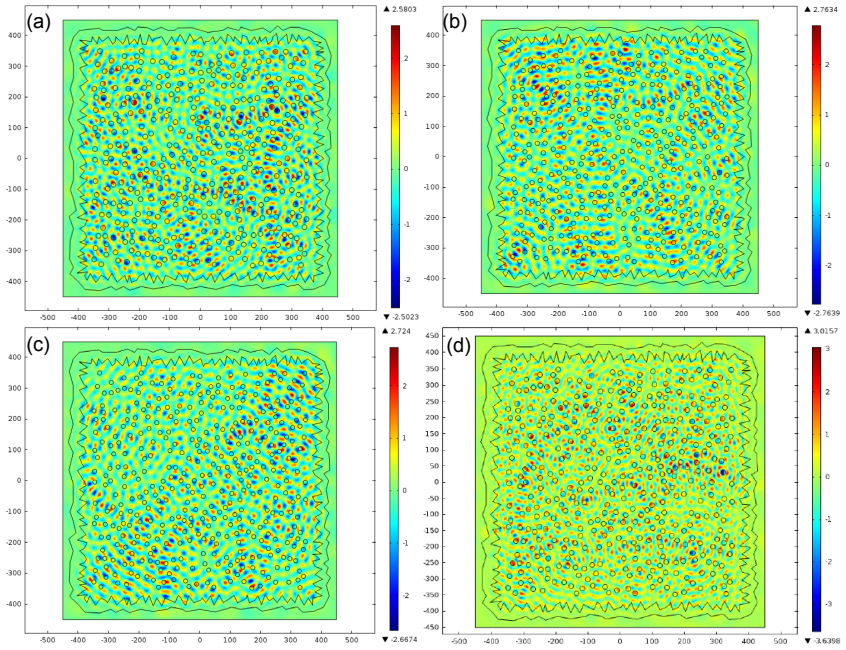

Figure 43: The figures show the spatial distribution of E_z (measured in in V/m) of the modes H ($\nu_H = 3.07 \div 3.10THz$ for varying FF) in (a), I ($\nu_I = 2.80 \div 2.84THz$) in (b), L ($\nu_L \approx 2.86THz$) in (c) and M ($\nu_M \approx 3.62THz$) in (d). [Type-C resonators, $0.59mm^2$]

5 RESULTS AND DISCUSSION

5.1 TRANSPORT AND OPTICAL MEASUREMENTS

All the fabricated devices were tested electrically and optically to evaluate how the different physical and geometrical parameters affect the lasing threshold, the emitted power and the slope efficiency.
The transport characterization allows correlating the applied bias V and the injected current density J (plotted in the IV curve), while the optical power measured by a pyroelectric sensor is reported as a function of the injected J in the LI curve. Usually, they are shown together in the LIV plot to highlight the change of the electrical response at some critical points, such as the lasing threshold and the negative differential resistance (NDR) regime after the peak of optical power. Some important information can be derived form these data:

- the threshold current density J_{th}, i.e. the current per unit area at which the device starts lasing;
- the maximum peak optical power P_{max}, i.e. the maximum emitted power;
- the corresponding current density J_{max} where light emission is more intense;
- the slope efficiency dP/dI which indicates how fast the emitted power grows with the injected current and is in turn a clear feature of the device effiency;
- the wall-plug efficiency η_{wp}.

Some prototypical LIV characteristics for the different designed geometries A, B, C are reported in figures 44, 45 and 46 with detailed data analysis in captions.

All the measurements were taken while driving the QCLs in pulsed operation, with a pulse train frequency $\nu = 50kHz$ and pulse width $PW = 200ns$, resulting in a duty cycle $DC = \nu \cdot PW = 1\%$. The only exception is the device of type-A, $FF = 27.0\%$ which was operated at a lower duty cycle ($\nu = 35kHz$ and $DC = 0.7\%$) due to its very intense optical power. As described in Methods, the optical power has been measured with a pyroelectric detector connected to a a lock-in amplifier, sensitive to both frequency and phase, while additively modulating the collection signal at a frequency of $33Hz$. The cryostat temperature was always kept at $T = 10K$.

5.1.1 Type-A

The threshold current densities and slope effiencies of the lasers patterned with the highly symmetric 7-fold geometry (type-A)are reported for $FF = 23\% \div 29\%$ in figure 47. The value of J_{th} exhibits a peak of $(510 \pm 10) A/cm^2$ at $FF = 27\%$ but it is in general lower, between $470 \div 480 A/cm^2$ (47.a). The high threshold for $FF = 27\%$ may be explained by a non-optimal thermal contact, which may produce a relevant self-heating hindering the condition of threshold. Moreover, a non-negligible Schottky resistance may exist between the bottom of the heterostructure and the submount, creating a parasitic conduction channel, so that the operation voltage is higher than that of the other type-A devices.

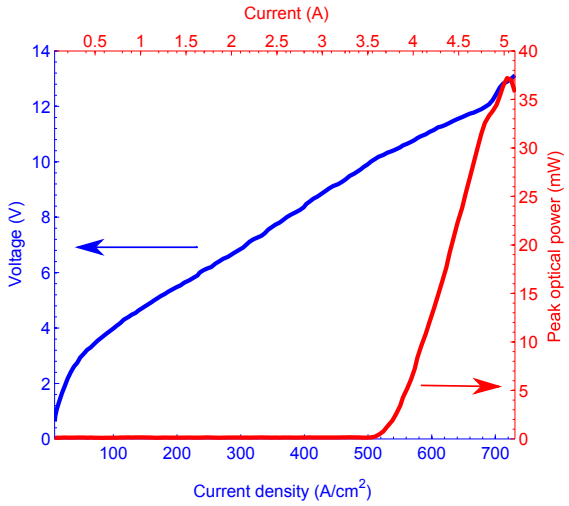

Figure 44: Device of type-A, $FF = 27.0\%$ showed $J_{th} = (510 \pm 10) A/cm^2$, $P_{max} = (37.2 \pm 0.2) mW$, $J_{max} = (718 \pm 6) A/cm^2$ and $dP/dI = (22.7 \pm 0.3) mW/A$ at $T = 10K$. The IV plot refers to the blue vertical axis, while the LI plot refers to the red one, as indicated by the arrows.

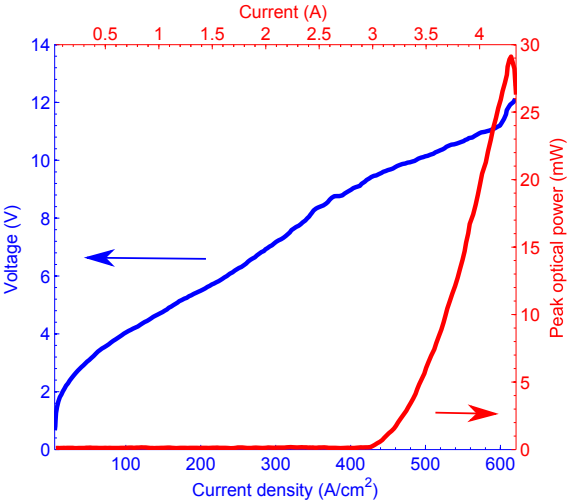

Figure 45: Device of type-B, $FF = 25.0\%$ showed $J_{th} = (430 \pm 10) A/cm^2$, $P_{max} = (29.1 \pm 0.2) mW$, $J_{max} = (613 \pm 7) A/cm^2$ and $dP/dI = (34 \pm 1) mW/A$ at $T = 10K$.

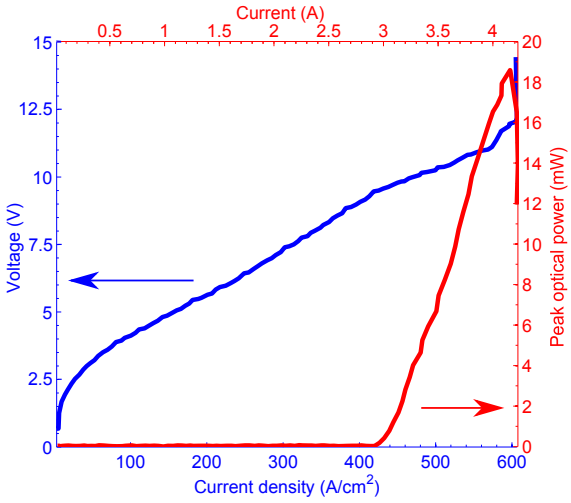

Figure 46: Device of type-C, $FF = 20.2\%$ showed $J_{th} = (425 \pm 10) A/cm^2$, $P_{max} = (19.2 \pm 0.2) mW$, $J_{max} = (600 \pm 10) A/cm^2$ and $dP/dI = (17.6 \pm 0.4) mW/A$ at $T = 10K$.

In figure 47.b the slope efficiency is reported, with a maximum value of $(26.6 \pm 0.7) mW/A$ for $FF = 28.4\%$. The device with $FF = 28.0\%$ instead has the poorest slope efficiency $dP/dI = (12.6 \pm 0.3) mW/A$, due to a peak optical power as low as $(10.3 \pm 0.1) mW$. As can be seen from table 3, one device with $FF = 27.0\%$ reached a maximum emission of $\approx 37.2 mW$ which makes it the most powerful laser among all the fabricated ones.

FF	P_{max} (mW)	η_{wp} (10^{-3})
23.7%	16.7 ± 0.1	0.31 ± 0.01
24.4%	21.1 ± 0.2	0.291 ± 0.008
27.0%	37.2 ± 0.1	0.61 ± 0.02
27.4%	23.1 ± 0.1	0.39 ± 0.01
28.0%	10.3 ± 0.1	0.202 ± 0.007
28.4%	21.8 ± 0.1	0.49 ± 0.02

Table 3: Maximum peak optical power and wall-plug efficiency η_{wp} of the highly symmetric 7-fold lasers (type-A) at $T = 10K$.

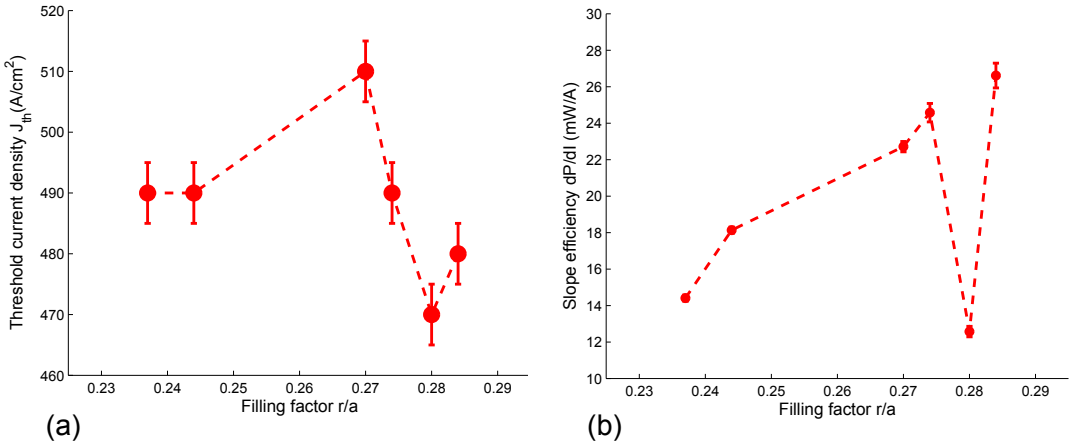

Figure 47: Plot of the measured threshold current density (a) and of the slope efficiency (b) as functions of the filling factor of the lasers of type-A at $T = 10K$.

5.1.2 Type-B

Figure 48 shows how J_{th} and dP/dI vary with the filling factor for $FF = 23\% \div 29\%$, in the case of the low symmetry 7-fold devices. It should be noted that the devices with $FF = 26.0\%$ and $FF = 28.5\%$, showing the highest $J_{th} = 490 \div 510 A/cm^2$, were partially contaminated by indium impurities during the fabrication process. As expected, although preserving laser action, the waveguide losses are visibly perturbed, leading to a larger J_{th} than the rest of type-B devices. In fact, these other disordered samples show $J_{th} \approx 430 \div 460 A/cm^2$, therefore having a lower threshold than their more symmetric counterparts of type-A.
In this geometry, the lowest threshold current densities $(430 \div 435 A/cm^2)$ and highest slope efficiencies (up to $(39 \pm 2) A/cm^2$) are reported for $FF \leq 25.0\%$, outdoing the measured values for type-A samples. The emitted power of these devices with low FF is the highest among the low symmetry set (see table 4).

FF	P_{max} (mW)	η_{wp} (10^{-3})
23.3%	24.2 ± 0.2	0.48 ± 0.02
24.6%	34.7 ± 0.2	0.63 ± 0.02
25.0%	29.1 ± 0.2	0.57 ± 0.02
26.0%	15.8 ± 0.1	0.32 ± 0.01
27.1%	10.14 ± 0.05	0.192 ± 0.005
28.5%	8.3 ± 0.1	0.155 ± 0.007

Table 4: Maximum peak optical power and η_{wp} of the low symmetry 7-fold lasers (type-B) at $T = 10K$.

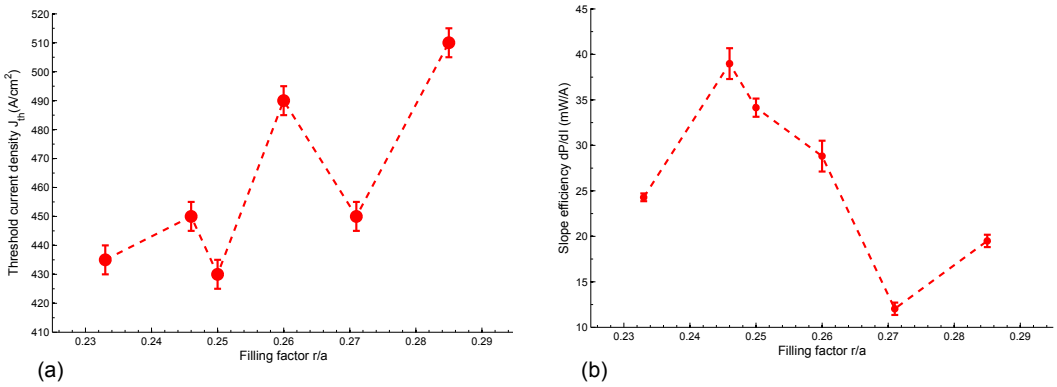

Figure 48: Plot of the measured threshold current density (a) and of the slope efficiency (b) as functions of the filling factor of the lasers of type-B at $T = 10K$.

5.1.3 Type-C

In the case of random lasers (type-C), not all the chosen geometries could be tested, due to a difficult liftoff. In particular, in two of the four tested devices, a small fraction of holes ($\approx$ 10%) on the device top metallizzation could not be opened. This resulted in a filling factor lower than expected for these two lasers. In figure 49, J_{th} and dP/dI are illustrated for different filling factors. One of the devices with incomplete liftoff ($FF \approx 24.5\%$) showed the best electrical performance, with a threshold current density as low as $410A/cm^2$ and a slope efficiency of $\approx 23mW/A$. If compared to the quasicrystal resonators, these random laser have a lower threshold ($J_{th} < 430A/cm^2$ in all devices), but the slope efficiency is a bit worse, comparable to that of the less performing devices of type-A and B. This is mainly due to the poor maximum emitted optical power, which gets worser for growing FF, as reported in table 5.
The three examined classes of aperiodic photonic resonators exhibit quite different electrical and optical behaviors, correlated with their different degrees of disorder. Concerning the threshold current density, a well defined trend appears: in general, there is a diminution of J_{th} in increasingly irregular structures, starting from type-A ($J_{th} \approx 470 \div 510A/cm^2$), to type-B ($J_{th} \approx 430 \div 450A/cm^2$) and type-C ($Jth \approx 410 \div 430A/cm^2$). Instead, a less remarkable difference appears for dP/dI, since only some devices of type-A and B exhibit a slope efficiency larger than $25mW/A$.

FF	P_{max} (mW)	η_{wp} (10^{-3})
20.2%	19.7 ± 0.2	0.39 ± 0.02
$\approx$ 24.5%	10.6 ± 0.2	0.23 ± 0.01
$\approx$ 26.8%	9.6 ± 0.2	0.33 ± 0.02
27.2%	7.8 ± 0.2	0.26 ± 0.01

Table 5: Maximum peak optical power and η_{wp} of the fabricated random lasers (type-C) at $T = 10K$.

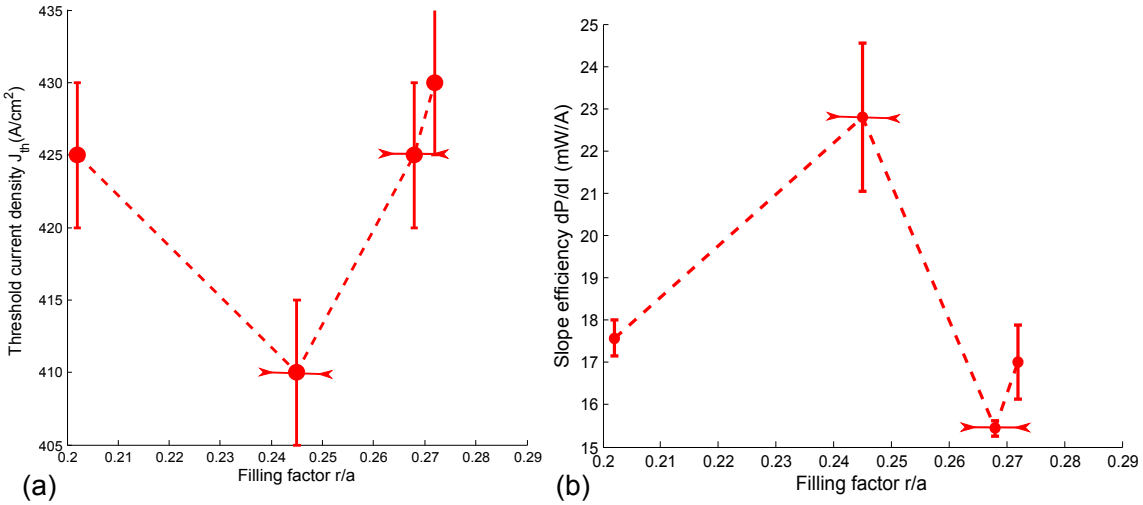

Figure 49: Plot of the measured threshold current density (a) and of the slope efficiency (b) as functions of the filling factor of the random lasers (type-C) at $T = 10K$.

5.2 EMISSION SPECTRA

To achieve multimode emission, an active region with large gain bandwidth was chosen. Such heterostructure allows gain in the huge range $2.7 \div 3.4THz$ (see [32]), making it very promising for the realization of multimode emission in the THz region. In fact, lasing at the frequencies permitted by the engineered photonic structures was observed and the related frequencies of the emitted photons determined by using the Fourier Transform Infrared Spectroscopy (FTIR). The lasers' emission was probed at the cryogenic temperature of $22 \div 30K$ for different injected current densities. In all these measurements, the devices were driven in pulsed mode, with a frequency of $50kHz$ and a pulse width of $200ns$ (duty cycle $DC = 1\%$). The FTIR resolution was set at $0.125cm^{-1}$, corresponding to approximately $4GHz$ and determining the error $\pm 2GHz$ on all the following spectral data. Every spectrum was averaged on four data acquisitions, to ensure a very low background noise.

Figure 50 can give an interesting insight of the spectral properties of some representative resonators. Let us consider the device with $FF = 27.0\%$ of type-A, whose LIV curve is in figure 44. As soon as the current density exceeds the threshold value, the main mode appears at $2.932THz$, followed by a couple of slightly less intense emissions at $3.066THz$ and $3.095THz$. When the injected current approaches to J_{max}, this photonic resonator supports up to ten modes. The other emission frequencies are: $3.106THz$, $3.149THz$, $3.192THz$, $3.227THz$, $3.236THz$, $3.263THz$ and $3.346THz$.

In the case of type-B, an example is given for $FF = 25.0\%$. The first emitted frequencies that appears at low current densities are $2.907THz$, $2.938THz$ and $3.062THz$. As the

electrical pumping is increased, these modes show a lower intensity while new ones emerge at higher frequencies, such as $3.091THz$, $3.173THz$ and $3.270THz$ which becomes the main emission line. Thus six modes are emitted together.
Finally, the random laser (type-C) with $FF \approx 26.8\%$ emits at six frequencies too. Besides the most intense line at $3.203THz$ appearing at the lasing threshold, new emission modes are brought about by a further raise of the injected current density. These other lines lie at $3.111THz$, $3.142THz$, $3.221THz$, $3.257THz$ and $3.324THz$. As the current density exceeds $J_{max} \approx 560A/cm^2$ the smaller modes show a reduced intensity, due to the onset of the NDR.
This device emits in the resonant feedback random lasing (RFRL) regime, showing distinct spectral lines with a very irregular frequency spacing between adjacent peaks. It is possible to rule the presence of Fabry-Perot modes out, related to the cavity round trip time. Since the air holes are enclosed in a square with a side of length $L = 670mm$, the associated free spectral range can be estimated to be $\Delta\nu_{FSR} = c/(2nL) \approx 62GHz$, assuming $n = 3.6$ in the semiconductor heterostructure, while the frequency separation in this spectrum ranges from $18GHz$ to $77GHz$. This means that the designed jagged profile of the absorbing chromium border have sufficiently irregular shape to hinder the formation Fabry-Perot-like modes.
Some general trends can be outlined, before introducing the effects of the size and the arrangement of the scatterrers one the spectral behaviour of each photonic structure, for different filling factors. In every tested device, all the spectral lines do not show appreciable variations when changing the current pumping within the electrically stable regime. In this respect, the only exception happens when the negative differential resistance region is reached. In fact, the band structure is titled so much by the applied bias that many trasitions cannot take place any more, while new modes are activated. Moreover, no regular spacing between the emission frequencies is found, thus excluding the existence of Fabry-Perot-like effects.

5.2.1 Type-A

The FTIR measurements of the highly symmetric 7-fold devices showed that the emission takes place over the broad spectral range $2.93 \div 3.45THz$, as shown in figure 51. The lasers characterized by intermediate filling factors (i.e. $FF = 24.4\%, 27.0\%, 27.4\%, 28.0\%$) demonstrate from 5 to 10 different frequencies. Though some spectral lines are detected for a particular value of the filling factor only, some of them can be recognised in spite of the change of FF. The most persistent modes are:

- $\nu_1 \approx 3.15THz$:
  it appears at $3.156THz$ for $FF = 23.7\%$ and 24.4%, but it slightly diminishes at $3.149THz$ for 27.0% and 28.0%

- $\nu_2 \approx 3.11THz$:
  a very weak line exists at $3.106THz$ for $FF = 24.4\%$, but then it clearly emerges for $FF = 27.0\%$ and 27.4% at $3.113THz$

Other common emission modes can be identified among the different spectra in 51, for example the samples with $FF = 27.0\%$ and $FF = 28.0\%$ share the frequencies $3.07THz$, $3.09THz$, $3.15THz$, $3.19THz$.
The plot also indicate that emission between 3.15 and $3.40THz$ is privileged for low filling factors ($FF < 25\%$), while for higher FFs other lower frequencies down to $2.93THz$ can be detected.

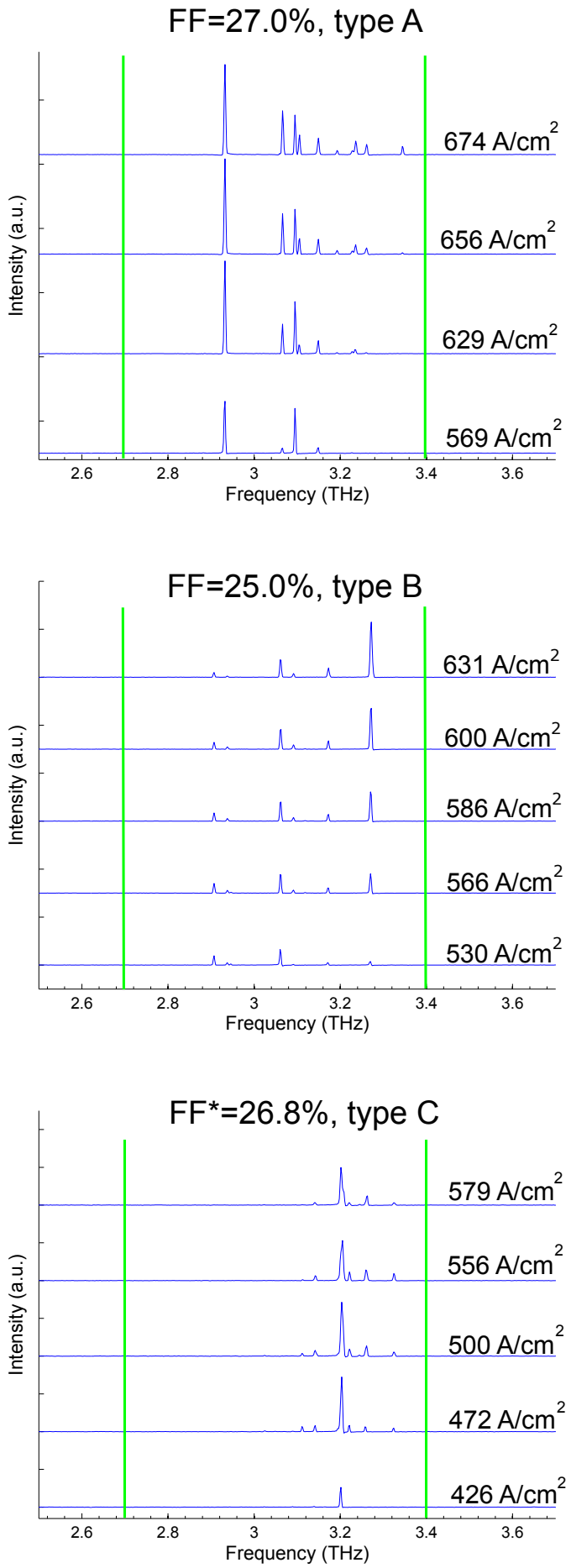

Figure 50: Emission spectra of the resonators with $FF = 27.0\%$ (type-A), $FF = 25.0\%$ (type-B) and $FF \approx 26.8\%$ (type-C) for different current densities. An error of $\pm 6 A/cm^2$ should be added to the current densities. The green lines indicate the gain bandwidth of the used active region.

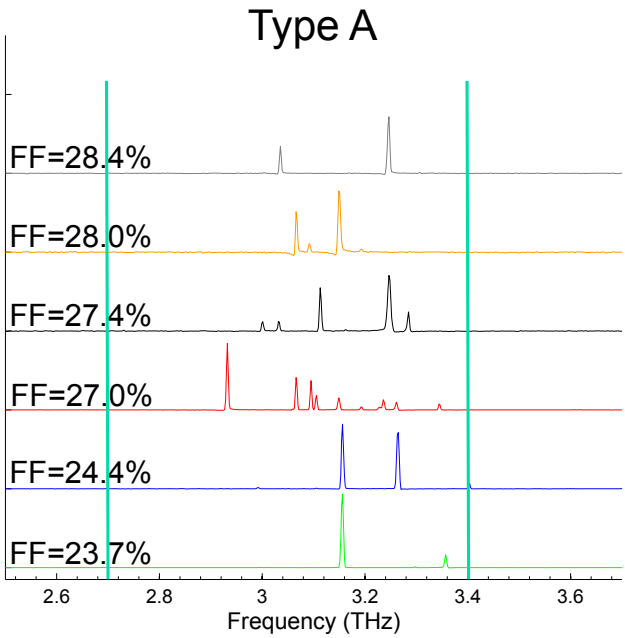

Figure 51: Representative spectra of the highly symmetric 7-fold resonators, measured in the electrically stable regime. Relative intensities are not to scale and an error of $\pm 6A/cm^2$ should be added to the current densities. The spectra are taken at current densities corresponding to the condition of maximum optical emission. The vertical cyan lines indicate the gain bandwidth of the active region.

5.2.2 Type-B

The spectra of the low symmetry 7-fold lasers (type-B) were probed with the FTIR, showing emission in the interval $2.90 \div 3.37 THz$ (see figure 52), which is comparable to that of type-A. As in the latter, even in type-B samples with low filling factors ($FF < 25\%$) are characterised by prevailing emission above $3.1 THz$. A small number of less intense lines appear at lower frequencies only for larger filling factors.
The most persistent modes for this geometry are quite close in frequency:

- $\nu_1 \approx 3.24 THz$ for $FF = 23.3\%, 24.6\%$ and 27.1%
- $\nu_2 \approx 3.25 THz$ for $FF = 23.3\%, 26.0\%$ and 27.1%

All these devices show at least four modes emitted togheter, with the best multimode emission made up by six spectral lines for $FF = 23.3\%, 25.0\%$.
It should be noted that one of these lasers (with $FF = 28.5\%$) was burnt at the beginning of the FTIR measurements, so no spectra are available for it.

5.2.3 Type-C

The FTIR spectra of the emission of the four tested random resonators are reported in figure 53. With respect to the two 7-fold geometries, the spectral lines are concentrated in a smaller interval $\approx 3.0 \div 3.3 THz$. This is a clear feature of the gain competition mechanism in a random laser, which determines the dominant role of high-Q modes and the suppresion of low-Q, spatially separated modes. The device with $FF = 27.2\%$ was probed at low currents due to issues of excessive heating and only three modes are detected, at irregularly spaced frequencies ($\Delta\nu_{12} \approx 42 GHz$ and $\Delta\nu_{23} \approx 58 GHz$). All the random

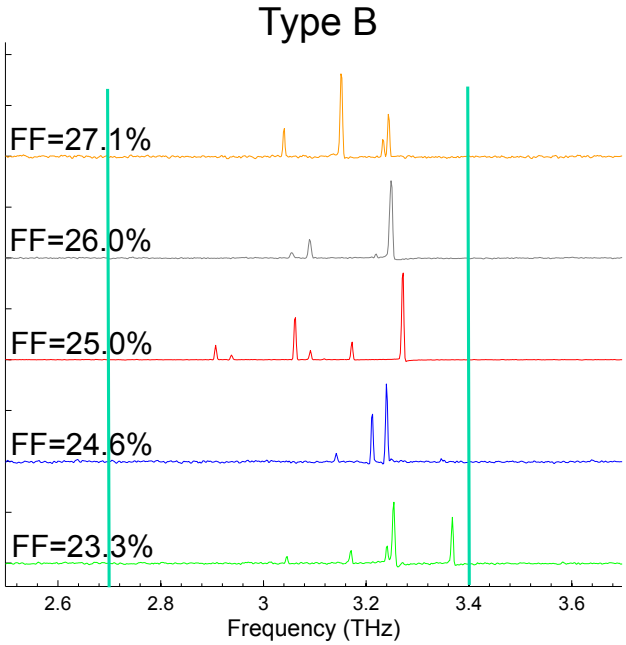

Figure 52: Representative spectra of the low symmetry 7-fold resonators, measured in the electrically stable regime. Relative intensities are not to scale and an error of $\pm 6 A/cm^2$ should be added to the current densities. The spectra are taken at current densities corresponding to the condition of maximum optical emission. The vertical cyan lines indicate the gain bandwidth of the active region.

devices are characterised by strongly variable frequency separation between adjacent spectral lines, varying from a minimum of $10 \div 20 GHz$ to a maximum of $\approx 60 \div 90 GHz$ in the different lasers. Instead, the free spectral range Δ_{FSR} is approximately $50 GHz$ for the larger geometry and $60 GHz$ for the smaller one.

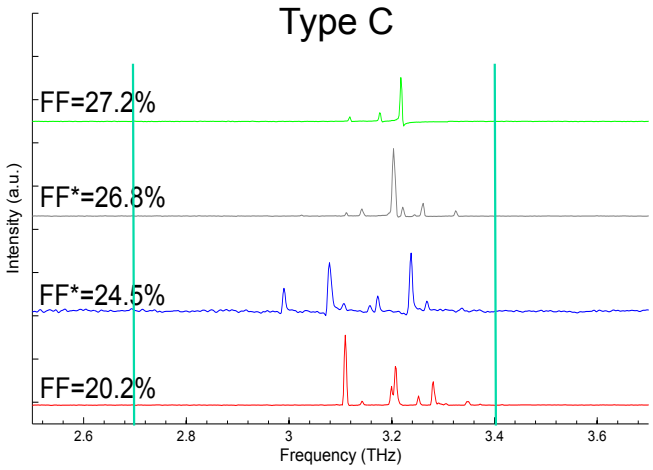

Figure 53: Representative spectra of the random resonators, measured in the electrically stable regime. Relative intensities are not to scale and an error of $\pm 6 A/cm^2$ should be added to the current densities. $FF*$ indicates the device with incomplete liftoff. The spectra are taken at current densities corresponding to the condition of maximum optical emission. The vertical cyan lines indicate the gain bandwidth of the active region.

5.3 CORRELATION WITH SIMULATIONS

As shown in chapter 4, the choice of the fabricated photonic structures was based on the results of a large amount of two-dimensional simulations. The eigenmodes in the designed resonators were numerically calculated to find their quality factors and identify the most likely frequencies for laser action.
The emission spectra reported so far indicate a good agreement between simulations and experimental measurements. For example, calculations showed that the highly symmetric 7-fold resonators have a larger number of high-Q modes in the QCL gain bandwidth than the low symmetry ones. This is reflected in experimental data, since one of the device of type-A ($FF = 27.0\%$) exhibits the largest number of spectral peaks. Nonetheless, type-B devices have very intense spectral lines concentrated in the high-frequency region $\nu > 3.1THz$, as predicted by the simulated eigenmodes reported in 36 and 38. Concerning the random lasers, their low emitted optical power can be correlated with their generally low computed Q.
It is useful to compare the experimental emission spectra with the expected high-Q frequencies for at least some of the measured lasers.

- In the case of the highly symmetric 7-fold device, with $FF = 27.0\%$ and area $0.64mm^2$, FT-IR spectra show up to ten peaks (figure 50.a). In the Q plot of figure 54, the simulated high-Q eigenmodes circled in red ($2.86THz$, $3.05THz$, $3.09THz$, $3.12THz$, $3.25THz$ and $3.35THz$ in the QCL gain bandwidth) are well correlated with most of the emission frequencies, such as $2.932THz$, $3.066THz$, $3.095THz$, $3.106THz$, $3.23THz$ and $3.346THz$. The difference between computed and measured frequencies is, at worst, few tens of GHz.

- For the device of type-B, $FF = 25.0\%$ and $A = 0.64mm^2$, the simulation indicates high-Q eigenmodes at $2.88THz$, $2.93THz$, $3.02THz$, $3.10THz$. $3.20THz$, $3.28THz$ and $3.36THz$ within the gain bandwidth (see 55). These values are comparable with most measured frequencies $2.907THz$, $2.938THz$, $3.062THz$, $3.091THz$, $3.173THz$ and $3.27THz$ within $30 \div 40GHz$ or even less.

- For the random laser (type-C) with $FF = 20.2\%$ and area $A = 0.59mm^2$, the predicted high-Q modes have frequencies $2.77THz$, $2.83THz$, $3.09THz$, $3.16THz$, $3.36THz$ (figure 56), while the experimental spectral lines correspond to $3.109THz$, $3.142THz$, $3.198Thz$, $3.207THz$, $3.252THz$, $3.281THz$, $3.346THz$.

5.4 THERMAL CHARACTERIZATION

Due to the small energy of THz-frequency transitions (typically few tens of meV), THz QCLs are extremely sensitive to the phononic activation associated with heating. So they require a strict control over the operating temperature T. In fact, an increase of temperature has two main effects:

- electrons lying in non radiative levels gain enough energy ($\approx k_B T$) to reach the lower level of the lasing transition, hindering the population inversion necessary for lasing;

- also the electronic in-plane momentum $\mathbf{k}_{||}$ grows, enhancing the emission of LO-phonon. Thus, the non-radiative channels compete with the radiative decay, diminishing the lifetime of the level

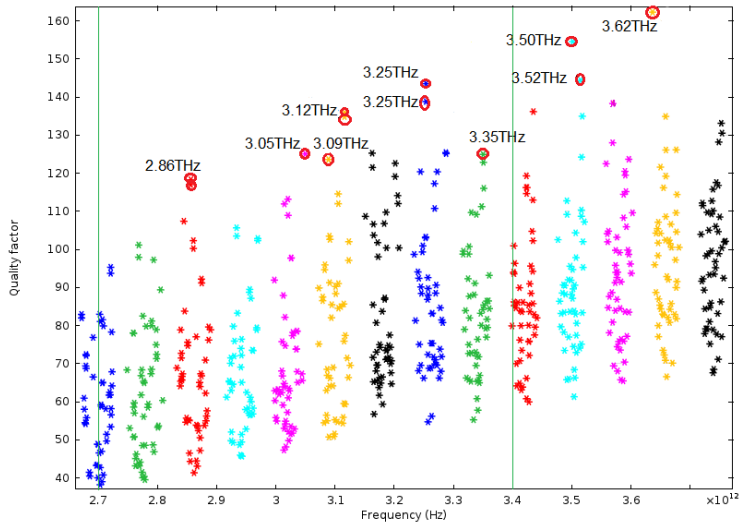

Figure 54: Results of the simulation of the eigenmodes' Q factors in the device with $FF = 27.0\%$, $A = 0.64mm^2$, type-A. The gain bandwidth is $2.7 \div 3.4THz$ (green vertical lines).

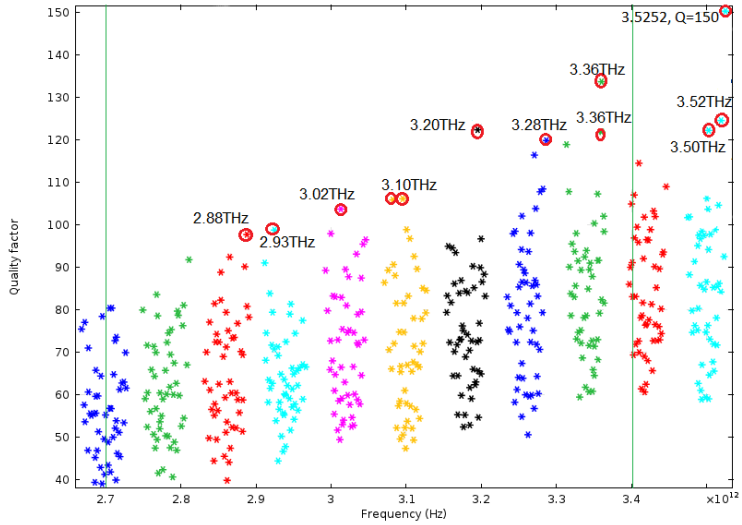

Figure 55: Results of the simulation of the eigenmodes' Q factors in the device with $FF = 25.0\%$, $A = 0.64mm^2$, type-B. The gain bandwidth is $2.7 \div 3.4THz$ (green vertical lines).

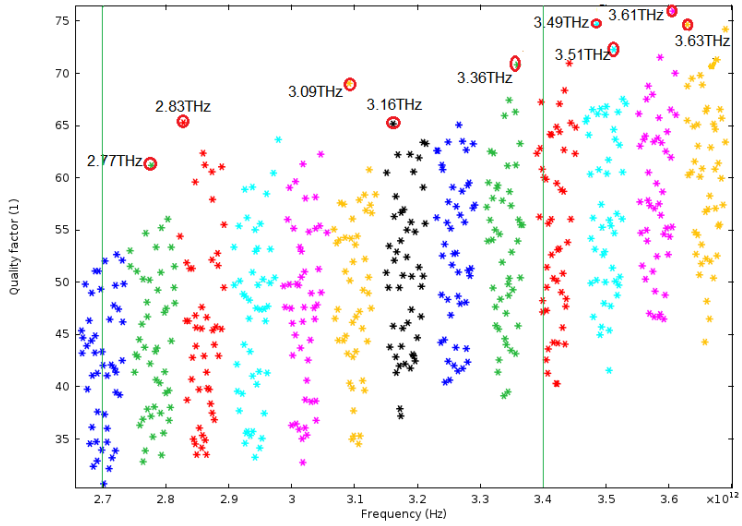

Figure 56: Results of the simulation of the eigenmodes' Q factors in the device with $FF = 20.2\%$, $A = 0.59mm^2$, type-C. The gain bandwidth is $2.7 \div 3.4THz$ (green vertical lines).

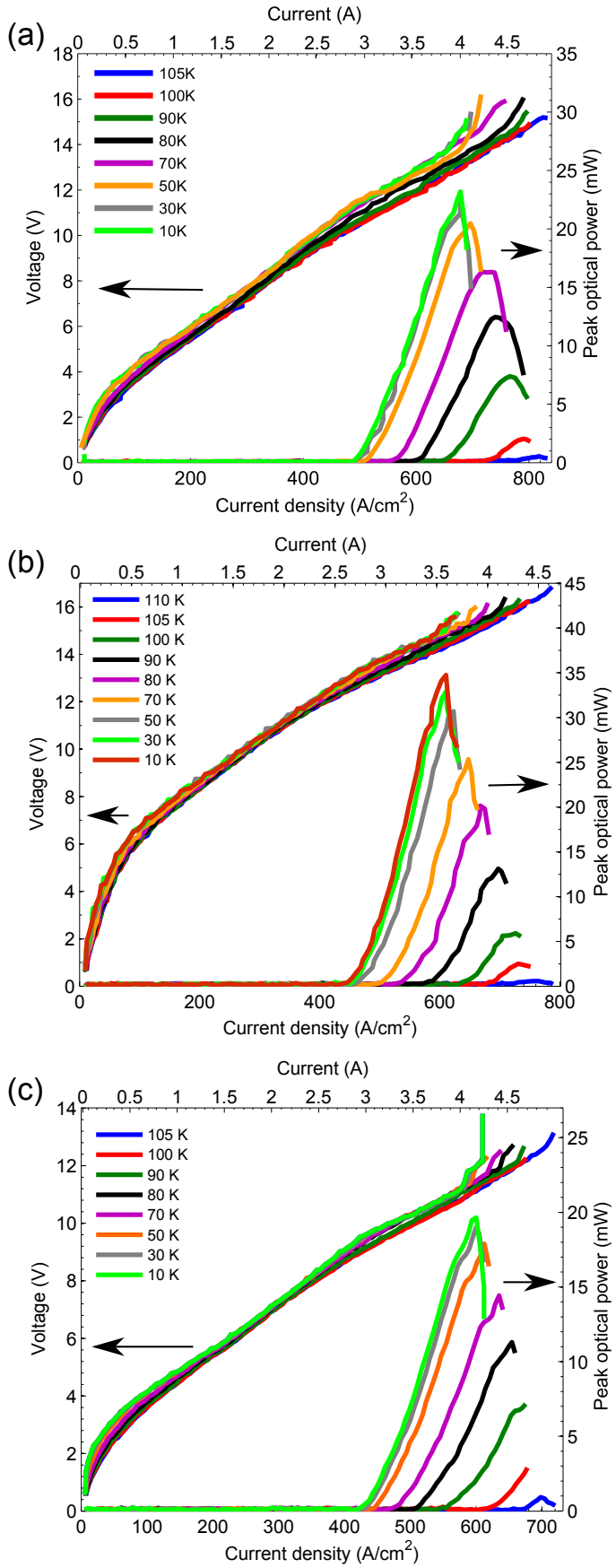

Figure 57: The LIV characteristics of the samples with $FF = 27.4\%$, type-A in (a), $FF = 24.6\%$, type-B in (b) and $FF = 20.2\%$, type-C in (c) are plotted for different operating temperatures. As previously reported, the different voltage at which the devices start lasing can be partially attributed to both non-optimal thermal contact with the cryostat finger, causing self-heating, and the presence of a parasitic conductive channel between the device and the submount, inducing a non-negligible current leakage.

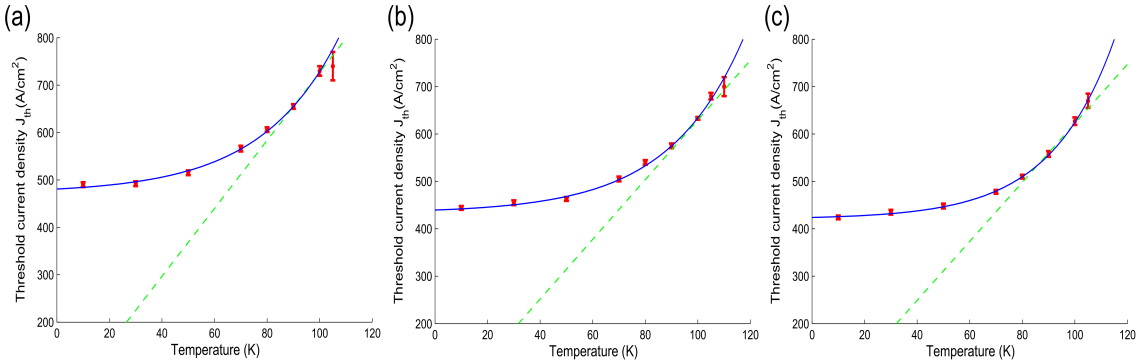

Figure 58: The measured threshold current at different temperature (up to $105 \div 110K$) are shown for the lasers with $FF = 27.4\%$, type-A in (a), $FF = 24.6\%$, type-B in (b) and $FF = 20.2\%$, type-C in (c). The blue curve is the fit obtained with equation 137, while the green line is the linearization of the formula 138 for high temperatures.

This results in higher electrical pumping needed to overcome these processes and achieve gain, with a general worsening of device performance in terms of threshold current density, optical power and slope effciency. When a critical temperature T_{max} is exceeded, the signal of the laser becomes indistinguishable from the noise. In order to characterize the thermal response of our photonic resonators, one sample for each geometry was tested in the temperature range $10 \div 110K$, using a heating system. In this case, the duty cyle was reduced to $DC = 0.3\%$ using a pulse frequency of $15kHz$, so that the self-heating due to Joule effect was limited. The typical dependance of the LIV curves on the temperature is clearly visible in figure 57. The evolution of J_{th} at different temperatures can be described with the phenomenological formula:

$$J_{th}(T) = J_1 + J_2 \exp\left(\frac{T}{T_2}\right) \tag{137}$$

which can be approximated in the form

$$J_{th}(T) \approx J_0 \exp\left(\frac{T}{T_0}\right) \tag{138}$$

and conveniently linearized in the region of high temperature, as can be seen in figure 58. The following results were obtained:

- type-A, $FF = 27.4\%$, $A = 0.53mm^2$
  the maximum temperature at which this sample emitted a detectable signal was $T_{max} = 105K$, while the fitted parameters are $T_0 = (113 \pm 9)K$ and $T_2 = (30 \pm 2)K$
- type-B, $FF = 24.6\%$, $A = 0.53mm^2$
  its thermal parameters are $T_{max} = 110K$, $T_0 = (114 \pm 10)K$ and $T_2 = (29 \pm 2)K$
- type-C, $FF = 20.2\%$, $A = 0.59mm^2$
  its emission cannot be measured for $T > T_{max} = 105K$, while the fit gives $T_0 = (107 \pm 9)K$ and $T_2 = (24.2 \pm 0.7)K$

The device was also fabricated in a standard double metal configuration, showing laser action up to $140K$ and having $T_0 = 110K$. The good thermal performances demonstrate that the disordered patterning of the top metallization does not undermine the thermal behaviour of the samples, with respect to a traditional ridge geometry.
It is interesting to estimate the sevice self-heating by Joule effect, calculating the peak

lattice temperature T_L from the heat sink temperature T_H of the cold finger of the helium cryostat:

$$T_L = T_H + R_t IV \cdot DC \tag{139}$$

I and V are the current and the voltage at maximum emission, DC is the duty cycle indicating how long the laser is switched on in one second (in this case, 0.3%) and $R_t \approx 28K/W$ is the thermal resistance [35]. Therefore, we can estimate the maximum lattice temperature to be $T_L \approx 111K$ for the device of type-A, $T_L \approx 116K$ for the device of type-B and $T_L \approx 110K$ for the device of type-C.

5.5 FAR FIELD INTENSITY PROFILES

The far field profile of the emitted intensity of some lasers was collected, following the procedure illustrated in chapter Methods. All samples were measured at a temperature of $10K$, driving them with a pulse train of frequency $50kHz$ and duty cycle $DC = 1\%$. The pyroelectric sensor, having a sensitive area of $\approx 7mm^2$, was connected to the lock-in system and always placed at the fixed distance of $\Delta z = 4.5cm$ from the laser surface. Two computer-controlled motorized linear stages could move the sensor in the orthogonal plane $x - y$, scanning the light intensity at different positions. The device is placed on the frontal cold finger of the cryostat, so that its vertical emission can be collected. These data were then elaborated to convert the reference system to spherical coordinates $\phi - \theta$ and highlight the angular divergence of the beams. One representative far-field pattern is shown for each type of fabricated photonic structures in figures 59, 60 and 61.
The highly symmetric 7-fold laser in 59 has a well collimated emission profile, characterised by two narrow and close peaks of emission. The intensity of light rapidly decays outside a central region characterised by $\Delta\phi$, $\Delta\theta$ both smaller than $\approx 20°$.
The low symmetry 7-fold device in 60 has a much broader shape, showing an irregular, intense spot at the center, surrounded by other bright peaks. The divergence can be estimated at $\Delta\phi \approx 40°$ and $\Delta\theta \approx 30°$.
Finally, the random laser in 61 shows a main spot with an approximately rectangular shape, extending for $\Delta\phi \approx 20°$ and $\Delta\theta \approx 20°$. A sudden diminution of light intensity takes place in the outer region.

Theoretically the far field profile is determined by the fields at the surface of the laser only, but actually it is also perturbed by the presence of the gold wires used to feed current in the device. One copper submount normally hosts two devices, each having a dedicated contact pad to allow a separate electrical control. So every sample is wedge bonded to one side only and the resulting arrangement of its wires is not homogenouos. Instead in the case of figure 59, the device was soldered alone on its submount, allowing the wires to be wedge bonded on both lateral pads. Such higher symmetry minimized the perturbation of the emitted fields, contributing to the narrow divergence of this laser. In the case of random devices, the wedge bonding was performed at the corners of the their irregular, nearly square top metallization.

At the end of the chapter, Scanning Electron Microscope (SEM) images of some representative devices of the three different geometries are shown in 62, 63 and 64.

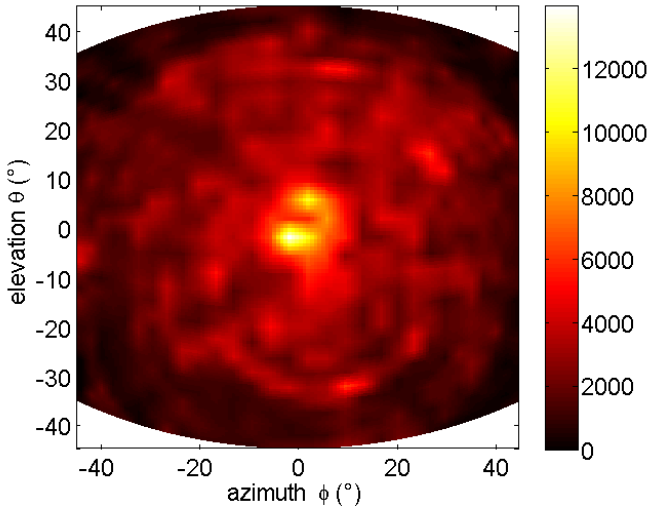

Figure 59: Far-field profile of the light intensity of the device with $FF = 27.4\%$ (type-A). The scanned region is comprised in $x = [-4.5cm, 4.5cm]$ and $y = [-4.5cm, 4.5cm]$. The color scale shows the power over the solid angle, in $mW/steradian$, as in the plots below.

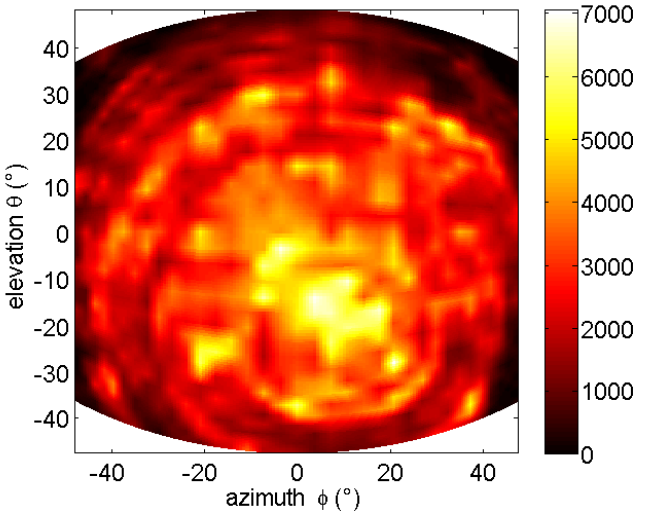

Figure 60: Far-field profile of the light intensity of the device with $FF = 25.0\%$ (type-B).The scanned region is comprised in $x = [-5.0cm, 5.0cm]$ and $y = [-5.0cm, 5.0cm]$.

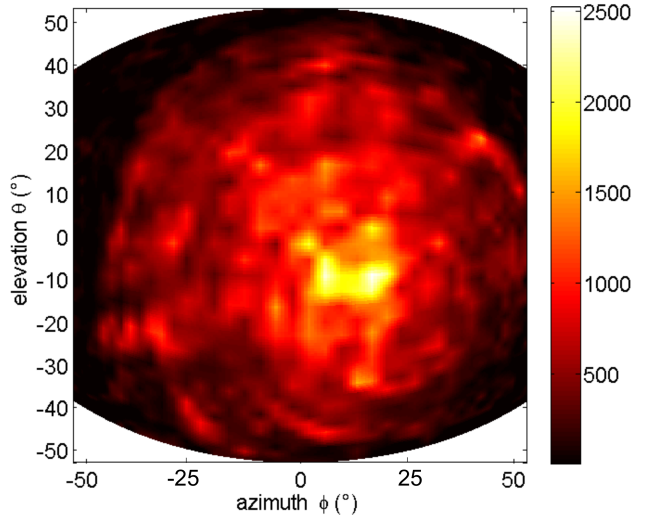

Figure 61: Far-field profile of the light intensity of the device with $FF = 27.2\%$ (type-C). The scanned region is comprised in $x = [-6.0cm, 6.0cm]$ and $y = [-6.0cm, 6.0cm]$.

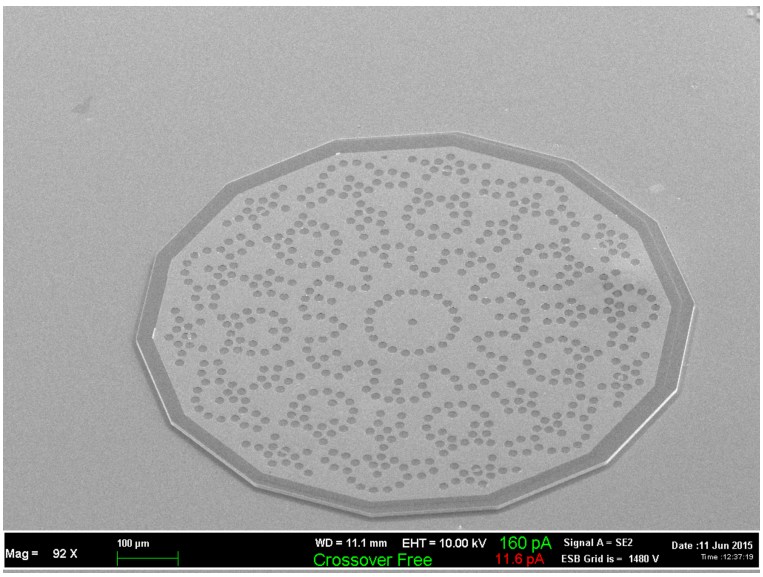

Figure 62: A Scanning Electron Microscopy (SEM) image of one of the fabricated highly symmetric 7-fold resonators (type-A). The SEM holder was tilted with respect to the electron beam direction, so this scansion is not vertical, unlike the next pictures.

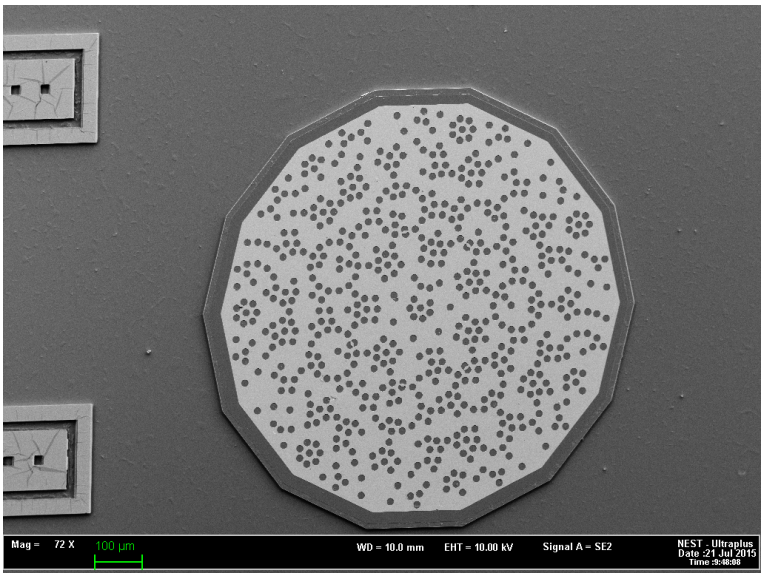

Figure 63: A SEM image of a fabricated low symmetry 7-fold resonator (type-B).

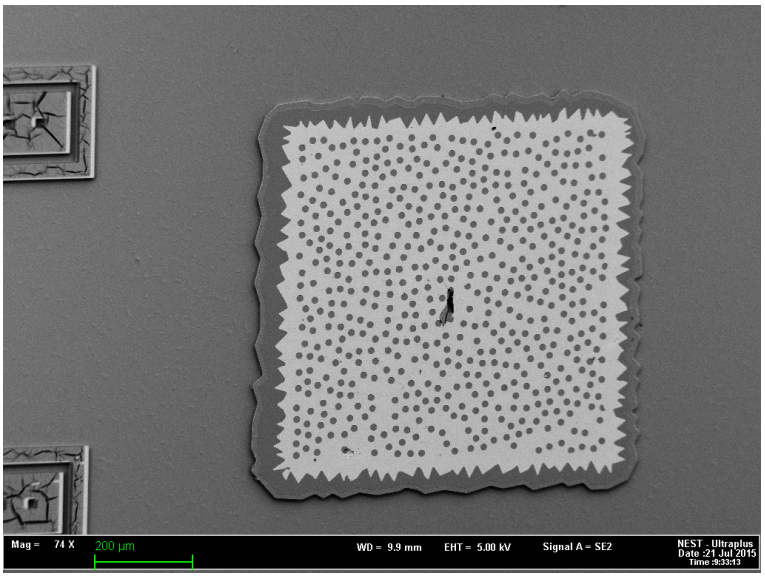

Figure 64: A SEM image of one of the fabricated random lasers (type-C).

6 THZ SATURABLE ABSORPTION IN GRAPHENE

6.1 THEORY

To this point, we have demonstrated multimode surface emission from THz QCLs coupled to specially designed photonic structures. This result is interesting in the perspective of creating a novel "mode-locked" photonic resonator at THz frequencies. Mode-locking is an optical technique which enables the generation of ultra short laser pulses, based on the creation of a fixed phase difference between many modes, so that they can periodically interfere constructively and produce an intense outburst of light at a high rate repetition. Such process requires an external modulation (optical or electrical excitations, etc.) which gives active mode-locking or the use of non linear, passive elements such as saturable absorbers. Saturable absorbers are systems exhibitting a trasmission depending on the intensity of the incident radiation: when it is below a certain threshold intensity I_s, light is well absorbed, while it is transmitted above threshold.
Due to the usually strong electron-phonon interaction in a QCL, the relaxation time of the population inversion is as short as few picoseconds, so saturable absorbers with ultrafast dynamics are needed. In this respect, an interesting system is graphene, a new class of single-atom-thick material which has been extensively studied in recent years. It is characterised by a smooth-sided conical band structure (see figure 65.a). In fact, its conduction and valence bands converge to a single Dirac point in the K point of its first Brillouin zone. In this low energy region, energy dispersion is linear in the two-dimensional momentum $\mathbf{k} = (k_x, k_y)$: $E = \hbar v_F |\mathbf{k}|$ where $v_F = 10^6 m/s$ is the Fermi velocity. Near the Dirac point the band has no curvature, so the carriers' effective mass is zero: therefore, they are often referred to as "massless Dirac particles". Not only this gives unique transport properties to graphene, but it also produces peculiar optical properties, such as a universal linear absorption for low-intensity fields and ultrafast saturable absorption for high intensities.
These behaviours can be described as in the model of non-interacting fermions [36]. Let us conder a laser pulse with photons of energy $\hbar\omega$. When a single photon is absorbed, it excites an electron from the valence band to the conduction band. Then, non-equilibrium carrier populations are created at energies $E = -\hbar\omega/2$ and $E = \hbar\omega/2$, respectively, with momentum conservation. In the case of low optical excitations, perturbation theory applies and the Fermi golden rule gives the instantaneous density of absorbed power:

$$W^a(t) = \frac{2\pi}{\hbar}|M(t)|^2 D\left(\frac{\hbar\omega}{2}\right)\left[f_t\left(-\frac{\hbar\omega}{2}\right) - f_t\left(\frac{\hbar\omega}{2}\right)\right] \tag{140}$$

The density of states is the same for both energies: $D(\pm\hbar\omega/2) = (\hbar\omega)/(\pi\hbar^2 v_F^2)$, while $f_t(\pm\hbar\omega/2)$ is the corresponding electron occupation at time t. It is reasonable to assume $f_t(-\hbar\omega/2) \approx 1$ and $f_t(\hbar\omega/2) \approx 0$ since, in this regime, fast interband decay prevails. The matrix element of the transition between the initial and final states separated by $\hbar\omega$ can be calculated as:

$$|M(t)|^2 = \frac{1}{8\omega^2} e^2 v_F^2 I(t) \tag{141}$$

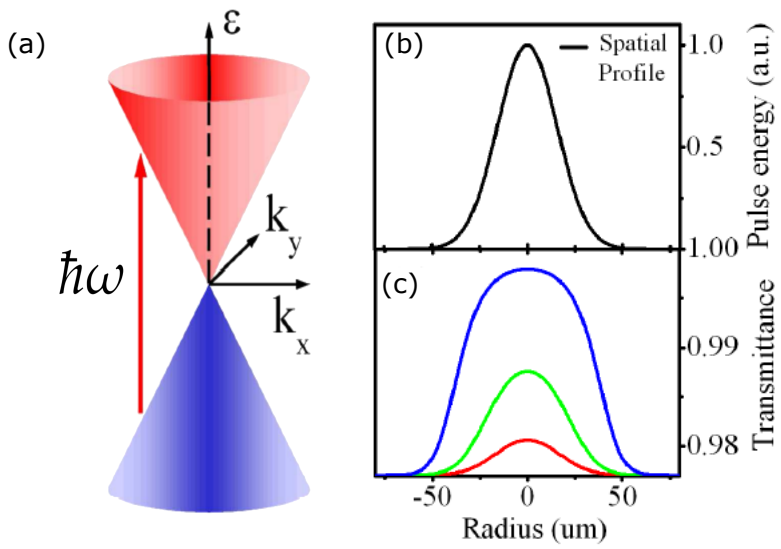

Figure 65: Band structure of graphene near the Dirac point (a). The red cone represents the conduction band, the blue one is the valence band. The red arrow indicates a momentum-conserving absorption of a photon with energy $\hbar\omega$. In (b), the calculated trasmittance of graphene for a gaussian beam (b) at $z = 0$ is shown in (c) for peak intensities of $1GW/cm^2$ (red line), $5GW/cm^2$ (green) and $80GW/cm^2$ (blue). The intraband relaxation time was set to $\tau_1 = 7fs$ and the incident radiation has wavelength $800nm$. Both images are adapted from [36].

under an incident intensity of light $I(t)$ which varies in time. The density of incident power is $W^i(t) = cI(t)$, so the linear optical transmittance is

$$T(t) = 1 - \frac{W^a(t)}{W^i(t)} = 1 - \pi\frac{e^2}{\hbar c} = 1 - \pi\alpha \tag{142}$$

α is the fine structure constant. This shows that in the perturbative regime the linear absorption of a single layer of graphene is $\alpha_0 \equiv \pi\alpha \approx 2.3\%$, irrespective of the light frequency or the temporal shape of the pulse.
Conversely, excitations with high intensity trigger two concurrent mechanisms which can realise saturable absorption.

- When large non-equilibrium population of carriers in the upper and lower bands are produced, further absorption of incoming photons at the same energy is reduced. This is particularly relevant at Terahertz frequencies, whose low-energy photons produce transitions near the Dirac point, where the density of state is quite low for intrinsic graphene. This means that the filling of the available states is easy and the Pauli blocking conditions can be reached [37]. More light is then allowed to pass, resulting in an increase of the transmission.

- The non-equilibrium carrier distributions also undergo intraband relaxation processes, which are dominated by the elastic carrier-carrier scattering, with a typical time scale τ_1 of few picoseconds. The population dynamics of two states at energies $\pm E$ can then be described by the equations:

$$\text{lower state (holes):} \quad \frac{\partial f_t(-E)}{\partial t} = \frac{\pi\alpha I(t)}{D(E)\hbar\omega}\left[f(E) - f(-E)\right] + \frac{1 - f(-E)}{\tau_1}$$

$$\text{upper state (electrons):} \quad \frac{\partial f_t(E)}{\partial t} = \frac{\pi\alpha I(t)}{D(E)\hbar\omega}\left[f(-E) - f(E)\right] - \frac{f(-E)}{\tau_1} \tag{143}$$

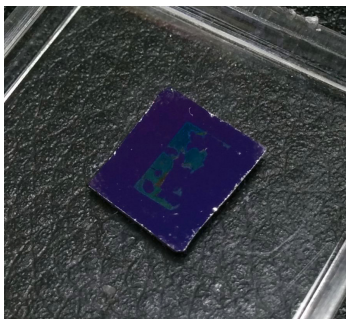

Figure 66: The few-layer graphene sample -the irregular greenish region- on an intrinsic silicon/silicon oxide substrate.

in which the right hand side takes into account the occupation probability balance induced by the photon absorption (first term) and the hole and electron relaxation in their respective bands (second term). The initial conditions are $f(-E)|_{-\infty} = 1$ (full valence band) and $f(E)|_{\infty} = 0$ (empty conduction band).
If we consider a light pulse with a gaussian temporal profile $I(t) = I_0 e^{-t^2/\tau^2}$, the solution to the system is

$$f_t(-\hbar\omega/2) - f_t(\hbar\omega/2) = 1 - 2\frac{\pi\alpha I_0}{D(\hbar\omega/2)}G(t) \tag{144}$$

where $G(t)$ is a complicate expression containing the gaussian error function Erf

$$G(t) = \int_{-\infty}^{t} e^{-x^2/\tau^2 + (x-t)/\tau_1} \exp\left\{\frac{\pi\alpha I_0\sqrt{\pi}\tau}{D(\hbar\omega/2)\hbar\omega}[Erf(x/\tau) - Erf(\tau/x)]\right\} dx \tag{145}$$

This process adds a contribution to the absorbed power per unit area, that is $W^a(t) = [f_t(-\hbar\omega/2) - f_t(\hbar\omega/2)]\pi\alpha I_0 e^{-t^2/\tau^2}$. Thus the overall transimittance has a temporal distortion due to the variable incident intensity of light:

$$T(t) = 1 - \pi\alpha + \frac{2(\pi\alpha)^2 I_0}{D(\hbar\omega/2)\hbar\omega}G(t) \tag{146}$$

The new term adds a positive contribution to the transmittance, in corrispondence with the high-intensity part of the pulse. Analogously, if we take into account the spatial distribution of the beam I_0 (for example, a gaussian profile), a bleaching in the transmitted light can be found in the region of maximum intensity (see figure 65.b). A complete mathematical treatment can be found in [36].

In general, in a simple two-level saturable absorption scheme, the relation between the incident intensity I_{in} and the transmitted one I_T is:

$$I_T = I_{in} - \left[\alpha_{NS} + \frac{\alpha_S}{1 + I_{in}/I_s}\right] I_{in} \tag{147}$$

α_{NS} is the non-saturable absorption coefficient, α_S is the non-linear saturable absorption coefficient and I_s indicates the saturation intensity.

6.2 MEASUREMENTS

In order to study the saturable absorption properties of graphene in the Terahertz spectral range, the transmission of the THz radiation emitted from a THz QCL through a few

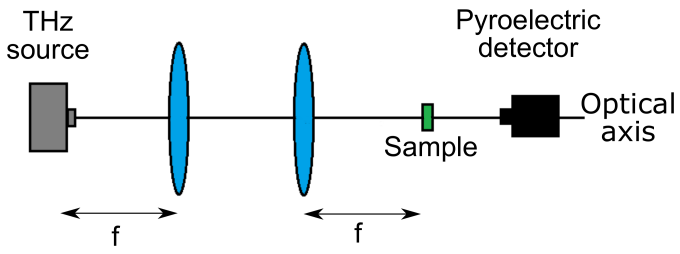

Figure 67: The configuration of the optical system for the open-aperture z-scan measurement is schematically reported. The two convergent lenses have identical focal length $f = 3cm$, and the sample can be translated along the optical axis to vary the incident light intensity.

layers of graphene film, transferred to an intrinsic silicon/silicon oxide substrate thanks to a nitrocellulose membrane prepared at the Graphene Lab of Cambridge University (see figure 66), was measured.
The open-aperture z-scan method was applied to characterize the pump-intensity dependance at room temperature. The experimental setup (figure 67) consisted of a THz QCL, two identical convergent lenses with focal length $f = 3cm$ which were accurately aligned, and a fixed pyroelectric sensor with a sensitive area of $\approx 7mm^2$. The laser beam of frequency $3.4THz$ was operated with pulse width of $500ns$ and duty cycle $DC = 2.5\%$, corresponding to a $50KHz$ frequency. A further modulation at $33Hz$ was added by a square function with 50% duty cycle for the lock-in system. The sample was placed on a holder which could be translated along the optical axis z using a micrometric system. This allowed for incident laser intensity to be varied. The beam intensity along the optical axis $I_0(z)$ is assumed gaussian:

$$I_0(z) = \frac{I_0}{1 + z^2/z_R^2} \tag{148}$$

where I_0 is the on-axis intensity and z_R is the Rayleigh distance. A knife-edge measurement was performed to characterize the beam profile, indicating a waist of size $w_0 = (95 \pm 6)\mu m$ (see figure 68). Then, the estimated beam intensity at the focal spot was $I_0 \approx 3.3W/cm^2$.
The signal transmitted through the graphene film is also attenuated by the silicon subtrate, since the total transmission is $I_T = T_{graph} T_{sub} I_{in}$. To isolate the graphene contribution, the transmission through a region of silicon only was measured to find T_{sub}. To highlight the non linear absorption, the transmitted signal is also normalized to the known non-saturable transmittance $1 - \alpha_{NS}$, obtained thanks to the FTIR measurements which gave $\alpha_{NS} \approx 0.75$ in the spectral region of interest. Therefore, the resulting normalised saturable transmittance T_S at the different positions along the z-axis can be expressed as:

$$T_S(z) = \left[1 - \alpha_{NS} + \alpha_S - \frac{\alpha_S}{1 + I_0(z)/I_s}\right] \frac{1}{1 - \alpha_{NS}} \tag{149}$$

The measurement shows a relevant transmission increase when the sample is in the region of highest beam intensity, indicating a strong saturable absorption in graphene at the frequency $3.4THz$. The collected data give the values of $\alpha_S = 0.6 \pm 0.1$ for the saturable absorption coefficient and $I_S = (4.1 \pm 1.1)W/cm^2$ for the saturation intensity of graphene (see figure 69).

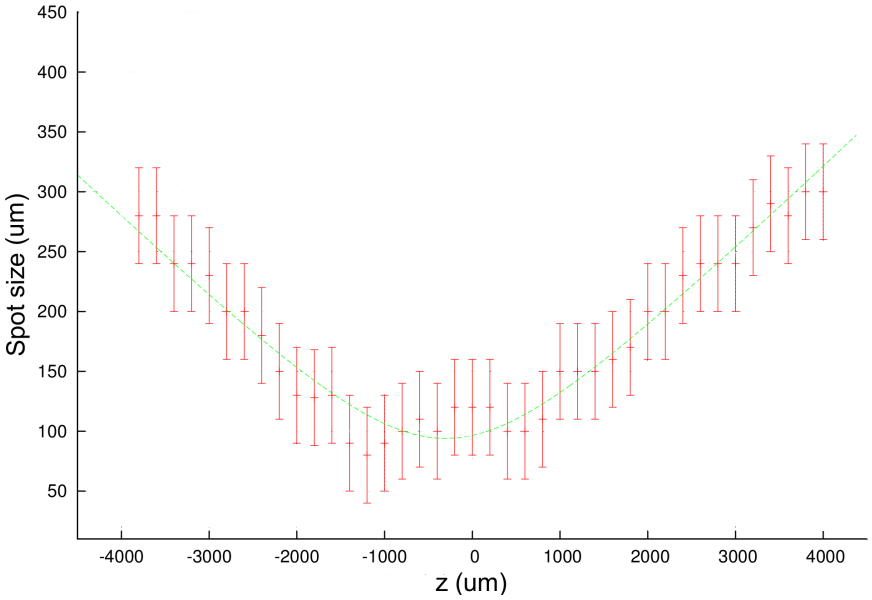

Figure 68: The plot shows the beam spot size at different position along the optical axis z, measured with a knife-edge method. The green line is the fit obtained for $w(z) = w_0\sqrt{1+z^2/z_R^2}$.

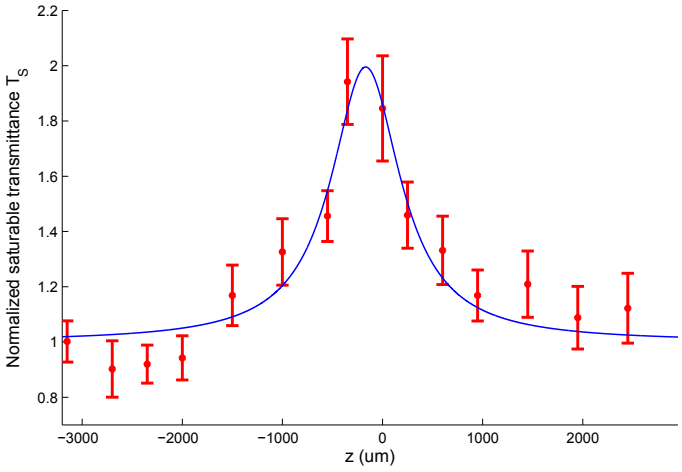

Figure 69: Saturable transmittance T_S in the graphene sample (normalized to both the substrate transmission and the graphene non-saturable transmission) at the different positions z along the beam profile. The blue line is the fitted transmittance $T_S(z)$.

7 CONCLUSIONS AND PERSPECTIVES

The objective of the present master thesis work was the experimental demonstration of multimode emission with high efficiency, highly collimated beam profiles and on a wide gain bandwidth from quasi-periodic and random photonic resonators exploiting a THz QCL active core.
Design, fabrication and study of the transport and optical behavior of a complete set of THz QCLs, having quasi-periodic and random resonator geometries with different filling factors, have been investigated. All lasers were characterized electrically and optically to study how the different physical and geometrical parameters affect the lasing threshold, the slope efficiency, the emitted power and the far-field intensity profile. The emission spectra were probed via Fourier Transform Infrared Spectroscopy (FT-IR), demonstrating the predicted multimode emission in all devices, with a maximum of ten spectral lines.

Random lasing was demonstrated for the first time in the THz regime, and the study of the dynamics of the unveiled optical modes, clearly identifies the resonant feedback random lasing regime.
The measured far-field intensity profiles shows a remarkable beam quality, with angular divergences as small as $\approx 20^{\circ}$ in the best performing highly symmetric quasi-crystal and random resonators.

The collected peak optical power reaches $\approx 40\ mW$ in the highly symmetric quasi-crystal THz QCLs, $\approx 35\ mW$ in the low symmetry quasi-crystal lasers and $\approx 20\ mW$ in the random THz lasers. All devices shows good electrical performances, with threshold current densities in the range $400 \div 500\ A/cm^2$ and slope efficiencies up to $\approx 40\ mW/A$. The maximum operating temperature is $110\ K$ (corresponding to a lattice temperature $116\ K$), providing a very good thermal behavior.

The demonstrated high-efficiency multimode emission opens interesting perspectives to explore the possibility to experimentally assess the predicted mode-locking transition of a random or quasi-random laser, after properly combining the developed resonators with ultrafast passive component, like graphene, in external or internal-embedded configurations. In this perspective, the saturable absorption of graphene was measured in the THz spectral region, revealing an relevant bleaching of the transmission for high incident light intensity.

Furthermore, the demonstrated low-divergence, combined with the reasonably low-threshold current densities in the double-metal waveguide configuration, and the tens-mW power level make the devised surface-emitting multimode lasers, interesting sources for multi-wavelength spectroscopic sensing across the far-infrared.

RINGRAZIAMENTI

Questa tesi è il frutto di un intenso e appassionante lavoro che non sarebbe stato possibile senza il supporto e i consigli delle persone che mi sono state vicine in questi mesi.

In primo luogo ringrazio i miei genitori, mia sorella e mia nonna per essermi sempre stati accanto in questo lungo cammino, insegnandomi a combattere per i miei sogni e i miei obiettivi, condividendo i momenti di gioia e serenità, e incoraggiandomi in quelli di dubbio e preoccupazione. Nonostante la distanza geografica, la loro presenza costante è stata ed è un punto di riferimento prezioso e insostituibile, di cui sarò per sempre riconoscente.

Sono grato alla dott.ssa Miriam Serena Vitiello, relatore di questa tesi, per la sua attenta supervisione nel corso di questo lavoro e per le sue spiegazioni rigorose e dettagliate. Gli innumerevoli consigli da lei forniti sono stati fondamentali in tutti questi mesi. Voglio esprimere la mia gratitudine a tutti i membri del *Terahertz Group* del NEST, che mi hanno introdotto alle tecniche di sviluppo e caratterizzazione dei dispositivi QCL, mostrando grandi disponibilità e qualità umane.

Un pensiero va anche a tutti gli insegnanti che ho avuto in questi anni: alcuni di loro hanno lasciato una traccia profonda nella mia formazione come persona e studente ed è stato un onore essere loro allievo.

Desidero ricordare i colleghi e gli amici con cui ho condiviso ore di studio e confronto, vita di laboratorio e momenti spensierati in questi anni di università. A loro va un grande ringraziamento, nella speranza che i nostri cammini possano continuare ad incrociarsi in futuro.

Infine, rivolgo un ringraziamento speciale a Cristina per essere stata al mio fianco, sostenendomi e rendendosi partecipe al percorso di questi mesi.

Grazie di cuore a tutti coloro che hanno creduto in me.

BIBLIOGRAPHY

[1] J. Faist. *Quantum Cascade Lasers*. Oxford University Press, Oxford, UK, 2013.

[2] Z.V. Vardeny A. Nahata and A. Agrawal. Optics of photonic quasicrystal. *Nature Photonics*, 7(177), 2013.

[3] J. M. Luttinger and W. Kohn. Motion of electrons and holes in perturbed periodic fields. *Physical Review*, 97(4), 1955.

[4] G. Grosso and G. Pastori Parravicini. *Solid State Physics*. Academic Press, London, UK, 2003.

[5] M. Levinstein et al. *Handbook Series on Semiconductor Parameters*. World Scientific, London, UK, 1999.

[6] K. Konishi and G. Paffuti. *Quantum Mechanics*. Oxford University Press, Oxford, UK, 2009.

[7] L. Esaki and R. Tsu. Superlattice and negative differential resistance in semiconductors. *IBM Journal of Research and Development*, 14(1), 1970.

[8] H. C. Liu and F. Capasso. *Intersubband transitions in Quantum Wells: Physics and Device Application I*. Academic Press, San Diego, USA, 2000.

[9] B. S. Williams. Terahertz quantum-cascade lasers. *Nature Photonics*, 1(517), 2007.

[10] R.F. Kazarinov and R.A. Suris. Possibility of the amplification of electromagnetic waves in a semiconductor with a superlattice. *Soviet Physics-Semiconductors*, 5(4), 1971.

[11] J. Faist. Wallplug efficiency of quantum cascade lasers: Critical parameters and fundamental limits. *Applied Physics Letters*, 90(253512), 2007.

[12] R. Koehler et al. Terahertz semiconductor-heterostructure laser. *Nature*, 417(156), 2002.

[13] C. Deutsch et al. Dopant migration effects in terahertz quantum cascade lasers. *Applied Physics Letters*, 102(201102), 2013.

[14] L. Mahler and A. Tredicucci. Photonic engineering of surface-emitting terahertz quantum cascade lasers. *Laser & Photonics Review*, 5(5), 2011.

[15] J. D. Joannopoulos et al. *Photonic Crystals: Molding the Flow of Light*. Princeton University Press, Princeton, USA, 2003.

[16] V. Passaro et al. *Advances in photonic crystals*. InTech Europe, Rijeka, Croatia, 2013.

[17] K. Srinivasan and O. Painter. Momentum space design of high-Q photonic crystal optical cavities. *Optics Express*, 10(15), 2002.

[18] D. Shechtman et al. Metallic phase with long-range orientational order and no translational symmetry. *Physical Review Letters*, 53, 1984.

[19] D. Levine and P.J. Steinhardt. Quasicrystals. I. Definition and structure. *Physical Review B*, 34(2), 1986.

[20] J.E.S. Socolar and P.J. Steinhardt. Quasicrystals. II. Unit-cell configurations. *Physical Review B*, 34(2), 1986.

[21] C. Janot. *Quasicrystals. A primer*. Oxford University Press, Oxford, UK, 1994.

[22] L. Mahler et al. Quasi-periodic distributed feedback laser. *Nature Photonics*, 4(125022), 2010.

[23] M. S. Vitiello et al. Photonic quasi-crystal terahertz lasers. *Nature Communications*, 5(5884), 2014.

[24] M. Notomi et al. Lasing action due to the two-dimensional quasiperiodicity of photonic quasicrystals with a Penrose lattice. *Physical Review Letters*, 92(12), 2004.

[25] D.S. Wiersma. Disordered photonics. *Nature Photonics*, 7(188), 2013.

[26] Hui Cao. Review on the latest developments in random lasers with coherent feedback. *Journal of Physics A: mathematical and general*, 38, 2005.

[27] M. Leonetti et al. The mode locking transition in random lasers. *Nature photonics*, 5, 2011.

[28] H. K. Liang et al. Electrically pumped mid-infrared random lasers. *Advanced Materials*, 25, 2013.

[29] J. E. S. Socolar et al. Quasicrystals with arbitrary orientational symmetry. *Physical Review B*, 32(8), 1985.

[30] M. Qiu. Effective index method for heterostructure-slab-waveguide-based two-dimensional photonic crystals. *Applied Physics Letters*, 81(7), 2002.

[31] M. Hammer and O.V. Ivanova. Effective index approximation of photonic crystal slabs: a 2D-to-1D assessment. *Optical and quantum electronics*, 41(4), 2009.

[32] M. Amanti et al. Bound-to-continuum terahertz quantum cascade laser with a single-quantum-well phonon extraction/injection stage. *New Journal of Physics*, 11(125022), 2009.

[33] K. Takahata et al. *Advances in micro/nano electromechanical systems and fabrication technology*. InTech Europe, Rijeka, Croatia, 2013.

[34] J. A. Stratton and L. J. Chu. Diffraction theory of electromagnetic waves. *Physical Review*, 59(99), 1939.

[35] M. S. Vitiello et al. Thermal properties of THz quantum cascade lasers based on different optical waveguide configurations. *Applied Physics Letters*, 89(021111), 2006.

[36] G. Xing et al. The physics of ultrafast saturable absorption in graphene. *Nature Photonics*, 18(5), 2010.

[37] F. Bianco et al. THz saturable absorption in turbostratic multilayer graphene on silicon carbide. *Optics Express*, 23(9), 2015.